Whistler Wave Propagation in Inhomogeneous Plasmas

Inauguraldissertation

zur

Erlangung des akademischen Grades eines

Doktors der Naturwissenschaften

der

Mathematisch-Naturwissenschaftlichen Fakultät

der

Ernst-Moritz-Arndt-Universität Greifswald

vorgelegt von

Jörg P. Pfannmöller

geboren am 08.11.1978

in Darmstadt

Greifswald, im März 2011

Dekan:	Prof. Dr. K. Fesser
1. Gutachter:	Prof. Dr. O. Grulke
2. Gutachter:	Prof. Dr. R. Sydora
Tag der Promotion:	17.06.2011

Abstract

In this thesis wave propagation in the whistler wave frequency range $\omega_{ci} \leq \omega \leq \omega_{ce}$ in the linear magnetized plasma experiment VINETA is investigated. The plasma is generated by a helicon antenna and has a diameter of about 10 cm. Whistler waves are launched by a loop antenna with a diameter of 4.5 cm and the fluctuating magnetic field is mapped by $\dot{B}$-probes. Experiments are carried out for plasma parameters $\gamma \leq 1/\sqrt{2}$ under which the only transversal polarized wave according to plane wave dispersion theory is the whistler wave. Due to the small collision frequencies $\nu \ll 1$ cyclotron damping of whistler waves in this parameter regime is dominant and depends only on the electron plasma-β.
The influence of the inhomogeneous plasma profile and excitation by a loop antenna is investigated by measurements of the fluctuating magnetic field perpendicular to the ambient magnetic field in azimuthal and radial axial planes. A mode characterized by the number of wave lengths m in the azimuthal direction is found. The mode structure is modified by the specific shape of the plasma density profile. Profiles with a homogeneous density inside the plasma radius are found to posses a comparably simple mode structure. An agreement in the mode structure of full-wave simulations in three dimensions, including a Gaussian density profile and excitation of the wave by a loop antenna, with the experimental results is found. Conclusions on the spatial structure of the excited mode are drawn using the simulations which predict excitation of an $m = 2$ mode. The wave is found to be ducted within the plasma radius over a wide parameter range. A Helmholtz decomposition of the simulations electric field exhibits the fluctuating space charge as the dominant source for the electric field, while the contribution due to induction is negligible. The magnetic field is given partially by the electron and displacement current. Both contributions to the magnetic field are of the same order of magnitude.
The frequency dependency of the excited modes spatial damping increment is investigated using measurements of the magnetic fluctuations along the symmetry axis of the plasma. In order to illustrate the parameter dependency, the electron plasma-β is varied over two orders in magnitude in the range $\beta = 4{\cdot}10^{-4} - 2.4{\cdot}10^{-2}$. The experimental result for the spatial damping increment of the mode yields a strong damping for wave frequencies $\omega/\omega_{ce} > 0.5$ at maximum plasma-β, which shifts to higher frequencies with decreasing β. The parameter dependency of the damping for a fixed frequency is studied in an axial ambient magnetic field gradient. In both cases an excellent agreement between the experimental result and predictions for cyclotron damping from plane wave dispersion theory is found.

Kurzfassung

In dieser Dissertation wird die Ausbreitung von Wellen im Whistlerwellen Frequenzbereich $\omega_{ci} \leq \omega \leq \omega_{ce}$ im linear magnetisierten Plasmaexperiment VINETA untersucht. Das Plasma wird von einer Helikonantenne erzeugt und hat einen Durchmesser von 10 cm. Whistlerwellen werden von einer Schleifenantenne mit einem Durchmesser von 4.5 cm angeregt und deren Magnetfeld wird mit $\dot{B}$-Sonden detektiert. Die Experimente werden in einem Parameterbereich $\gamma \leq 1/\sqrt{2}$ durchgeführt für den die Dispersionstheorie für ebene Wellen als einzige transversal polarisierte Welle die Whistlerwelle vorhersagt. Aufgrund der vernachlässigbar kleinen Stoßfrequenz $\nu \ll 1$ ist die Dämpfung der Whistlerwelle in diesem Parameterbereich durch Zyklotrondämpfung bestimmt welche nur vom Elektronen Plasma-β abhängt.
Der Einfluss der Plasmainhomogenität und der Anregung per Schleifenantenne wird durch Messungen des fluktuierenden Magnetfeldes senkrecht zum Hintergrundmagnetfeld in azimutalen und radial axialen Ebenen im Plasma untersucht. Diese zeigen eine Modenstruktur die durch die Anzahl der Wellenlängen m in der azimutalen Feldkomponente bestimmt ist. Die Modenstruktur wird durch das Dichteprofil des Plasmas modifiziert und besitzt in Plasmen mit homogener Plasmadichte innerhalb des Plasmaradius eine vergleichsweise einfache Struktur. Dreidimensionale full-wave Simulationen, unter Annahme eines Gauß'schen Plasmadichteprofiles und Anregung der Welle durch eine Schleifenantenne, zeigen in ihrer Modenstruktur eine gute Übereinstimmung mit den experimentellen Ergebnissen. Dies erlaubt einen Rückschluss auf die räumliche Struktur der angeregten Mode welche eine $m = 2$ Modenstruktur aufweist. Die Ausbreitung der Welle ist über einen weiten Parameterbereich auf einen räumlichen Bereich innerhalb des Plasmaradius begrenzt. Mittels einer Helmholtzzerlegung des elektrischen Feldes der Simulationen wird die fluktuierende elektrische Raumladung als dominante Quelle des elektrischen Feldes identifiziert, Beiträge durch Induktion sind vernachlässigbar. Das magnetische Feld ist durch den Elektronenstrom und den Verschiebungsstrom gegeben. Die Simulationen zeigen einen Beitrag beider Ströme zum Magnetfeld, der in der gleichen Größenordung liegt.
Die Frequenzabhängigkeit des räumlichen Dämpfungsinkrementes der angeregten Mode wird mittels Messung der magnetischen Fluktuationen entlang der Symmetrieachse des Plasmas charakterisiert. Zur Darstellung der Parameterabhängigkeit wird das Elektronen Plasma-β um zwei Größenordungen im Parameterbereich $\beta = 4 \cdot 10^{-4} - 2.4 \cdot 10^{-2}$ variiert. Das experimentelle Ergebnis für das räumliche Dämpfungsinkrement der Mode weist bei großem Plasma-β starke Dämpfung für Frequenzen $\omega/\omega_{ce} > 0.5$ auf, diese verschiebt sich zu höheren Frequenzen bei

kleinerem β. Die Parameterabhängigkeit der Dämpfung bei einer festen Anregungsfrequenz wird in einem axialen Gradienten des Hintergrundmagnetfeldes untersucht. In beiden Fällen gibt es eine exzellente Übereinstimmung zwischen dem experimentellen Ergebnis und Vorhersagen der Dispersionstheorie für ebene Wellen.

Contents

1 Introduction

Whistler waves have been discovered more than a century ago as interferences in telephone communication [1]. In world war one they appeared again as interferences during interception of enemy communication, which triggered scientific interest [2]. Whistlers found in nature are comprised of a band of frequency components. As a consequence of the whistler wave dispersion high frequencies in a whistler wave package are faster than low frequencies. Since whistlers occurring in nature posses frequencies in the audio range the dispersion leads to a whistling tone if the received signal is made audible. The origin and nature of whistler waves was clarified in connection with the discovery of the ionosphere by Appleton *et al.* [3]. In order to interpret the experimental results Appleton *et al.* developed a formalism called magneto-ionic theory [4, 5, 6] which is today known as dispersion theory and describes wave propagation in a magnetized plasma. This formalism was adapted in order to interpret investigations on whistler waves [7, 8]. Well founded predictions on whistler wave propagation and excitation have been established about half a century ago [9]. Those investigations clarified that whistlers are right-hand circular polarized electro magnetic waves, excited by lightnings, which propagate in the plasma surrounding the earth. Whistler waves are used for the exploration of the earth's space plasma especially for density measurements [10], but also in order to identify the structure of the space plasma around the earth which lead to the discovery of the plasma sphere [11].
In addition to whistler wave propagation also whistler wave damping is important. Especially the collisionless damping of whistler waves features interesting properties. Whistler waves in a plasma with finite temperature are due to kinetic effects like cyclotron [12] and Landau [13] damping. After inter hemispheric transport whistler waves in nature posses frequencies mainly in the very low frequency range, high frequencies are almost absent [10]. A possible explanation for this frequency cut-off is given by a combination of effects due to plasma inhomogeneities and cyclotron damping [14]. Based on this observation the determination of the particle distribution functions in astrophysical plasmas is possible [15].
Knowledge about the near-earth orbit is essential for todays world-wide communication via ground-based radio stations and satellites. Todays communication would not be possible without a clear cut knowledge of the plasma density profile in the earths outer atmosphere. Not to mention all the scientific and military space missions.
Experiments on whistler waves in astrophysical plasmas are performed using ground based radio stations [16], probes on board of sounding rockets [17], space ships [18], satellites in the earth's orbit [19] and even on satellites in the orbit of other plan-

ets in the solar system [20]. Those experiments have two major problems. First, the conditions under which the experiments are performed are not reproducible. Second, the experiments lack on spatial resolution. Many of those experiments measure the whistler wave field on a single point in space. In order to overcome those problems and to test the validity of available predictions on whistler wave propagation, laboratory experiments are performed [21].
Whistler wave physics is not only important in the exploration of nature, there are also important technical applications. Probably the most important technical application connected to whistler waves are helicon discharges. The counter part of whistler waves in a bounded plasma is called a helicon wave. Helicon waves are known to be highly effective in plasma generation [22] and have been discovered in connection with whistler wave investigations in laboratory devices. Though, widely used in laboratory and industrial applications the physical mechanism behind the helicon discharge is not yet known [23].
Besides the puzzle about the helicon sustained discharge another open field concerning whistler waves are their non-linear properties [24]. A huge number of theoretical investigations about non-linear aspects of whistler wave propagation are performed [25, 26, 27]. Experimentally it is challenging to establish the conditions needed in order to test those predictions. Just a few laboratory investigations on this topic have been performed [28, 29].
A pioneering laboratory experiment was performed in 1960 [30] in a toroidal device. Subsequent theoretical [31, 32] and experimental [33] investigations found a crucial influence of the plasma boundary and homogeneity on wave propagation. In a device with a homogeneous plasma free of boundary effects [34] the influence of the particular excitation method on whistler wave propagation was investigated systematically [35, 36, 37, 38, 39, 40]. An important influence of the excitation method on wave propagation was found [41].
The influence of the boundaries or plasma inhomogeneities on wave propagation causes a guiding of whistler wave energy called ducting. Ducting of whistler waves by plasma inhomogeneities plays an important role in the propagation of whistler waves in nature [42]. From the difference between ducted and free propagation details about the structure of the plasma profile in planetary space plasmas are deduced [43, 44]. Therefore, this became a topic on its own [45]. It is investigated in detail for cases in which geometrical optics is valid [34, 46, 47]. Today investigations of the general case are in the focus of interest [48, 49].
Due to the improvement of computing capabilities numerical full-wave simulations of whistler wave propagation are possible which allow to compute the field of the wave including properties of its specific excitation method and the underlying plasma profile [50]. Such simulations are especially useful for computation of ducted whistler wave propagation [51, 52] and are used to deduce predictions on whistler wave propagation, e.g. the mode structure of the excited wave. However, a benchmark test on the agreement of the predictions with experiments in a laboratory device is yet not available.
In cylindrical plasmas the geometrical damping of loop antenna excited whistler waves is found to depend on the radius of the plasma [48]. In plasmas with a

large radius, free of ducting effects due to the inhomogeneity geometric damping dominates over other damping mechanisms [34]. Thus, experiments on cyclotron damping are performed in cylindrical plasmas with a smaller radius in which wave energy is ducted and geometric damping is thereby suppressed [53, 54, 55]. Although investigations on whistler waves are performed in plasmas in which the influence of the plasma inhomogeneity is important the mode of whistler wave propagation in such systems is not yet identified [56, 34, 57, 58]. A major problem is the lack of adequate methods for the prediction of the excited mode.
The present work focuses on laboratory investigations of loop antenna excited whistler waves propagating in a cylindrical plasma in which the plasma inhomogeneity is important. Emphasis is placed on the characterization of the excited mode and kinetic effects in its damping. Full-wave simulations of the wave field are pointed out as a method for an accurate description of the observations. This aims on closing a gap in the research on whistler waves in laboratory plasmas, since predictions on wave propagation have before been achieved only in certain approximations. A combined analysis of simulations and experiments on whistler wave propagation is used to identify the excited mode. The cyclotron damping of the mode is investigated in order to allow for an interpretation of results previously reported on cyclotron damping of loop antenna excited whistler waves.
The thesis is structured as follows: In chapter 2 the cold plasma dispersion relation is used to define the properties of whistler waves and to identify a parameter window in which whistler waves are the only transversal propagating waves. Important properties of whistler wave damping due to collisions and propagation due to the anisotropy of the plasma are addressed. The hot plasma dispersion relation is used to perform predictions on and clarify the nature of cyclotron damping. In chapter 3 the methods used for data evaluation are elucidated. The influence of inhomogeneities on wave propagation in a cylindrical plasma is outlined in chapter 4. First, the effect of inhomogeneities is illustrated in the limit of geometric optics. Second, 3D full-wave simulations including the plasma profile and wave source of subsequent presented experiments are analyzed and predictions on wave propagation are performed. Both predictions are carried out for a cold and collisionless plasma.
In chapter 5 the experimental device including plasma and wave field diagnostic as well as the wave exciter is introduced. The experimental results are presented in chapter 6. Basic properties of loop antenna excited whistler waves are discussed using measurements of the magnetic fluctuations along the central axis of the plasma. The influence of plasma density inhomogeneities is characterized by 2D measurements in azimuthal and radial-axial planes. A plasma profile in which the parallel phase velocity in the plasma center equals the phase velocity of parallel propagating plane waves in a homogeneous plasma is identified. The measurements of whistler wave propagation in this profile are compared to simulations over a wide parameter range. The mode of the wave excited in the experiments is characterized from a comparison with simulations. This is followed by an investigation of the modes parallel dispersion and spatial damping along the symmetry axis of the plasma. The frequency and parameter dependency is compared to

kinetic dispersion calculations exhibiting an excellent agreement with the predictions. Finally a summary and a conclusion is given in chapter 7 followed by an outlook in chapter 8.

2 Whistler Wave Propagation in Homogeneous Plasmas

In this chapter the basic properties of whistler waves in a homogeneous plasma are outlined assuming propagation of plane waves. In this formalism the wave under discussion extends throughout the entire plasma. The frequency and plasma parameter regime of whistler wave propagation is identified in the framework of cold plasma dispersion theory. Wave dispersion and damping by collisions in this regime is discussed for parallel and oblique propagation. Index surfaces are pointed out as a simple graphical method to achieve an overview about the influence of the plasma anisotropy on wave propagation. Cyclotron damping of whistler waves is discussed using the hot plasma dispersion relation for parallel propagating waves. The considerations carried out in this chapter serve as a first order approximation for wave propagation in systems which have a higher degree of complexity.

2.1 Linear Dispersion Theory

Plasma dispersion theory describes propagation of plane waves in an infinitely homogeneous plasma. The fluctuating wave magnetic field $\widetilde{\mathbf{B}}$ is assumed small compared to the ambient magnetic field $\mathbf{B}_0$. Therefore, perturbation theory can be used to simplify the calculations. The temporal and spatial evolution of the wave is described by the Maxwell equations

$$\nabla \times \mathbf{B} = \mu_0 \left(\mathbf{J} + \epsilon_0 \frac{\partial \mathbf{E}}{\partial t} \right) , \qquad (2.1a) \qquad \nabla \times \mathbf{E} = -\frac{\partial \mathbf{B}}{\partial t} , \qquad (2.1b)$$

$$\nabla \cdot \mathbf{B} = 0 , \qquad (2.1c) \qquad \nabla \cdot \mathbf{D} = \rho_{sc} . \qquad (2.1d)$$

If propagation of plane waves is assumed (2.1a) and (2.1b) are given by

$$\mathbf{k} \times \mathbf{B} = -\omega \epsilon_0 \mu_0 \underline{K} \cdot \mathbf{E} , \qquad (2.2a) \qquad \mathbf{k} \times \mathbf{E} = \omega \mathbf{B} , \qquad (2.2b)$$

which are combined to a single wave equation

$$\mathbf{N} \times (\mathbf{N} \times \mathbf{E}) + \underline{K} \cdot \mathbf{E} = 0 , \qquad (2.3a) \qquad \mathbf{N} = \mathbf{k} c/\omega , \qquad (2.3b)$$

where $\underline{K}$ is the dielectric tensor and $\mathbf{N}$ is the index of refraction vector. In magnetized plasmas the electric displacement is related to the electric field by a tensor relation $\mathbf{D} = \underline{K}\mathbf{E}$, while the magnetic induction is related to the magnetic field by

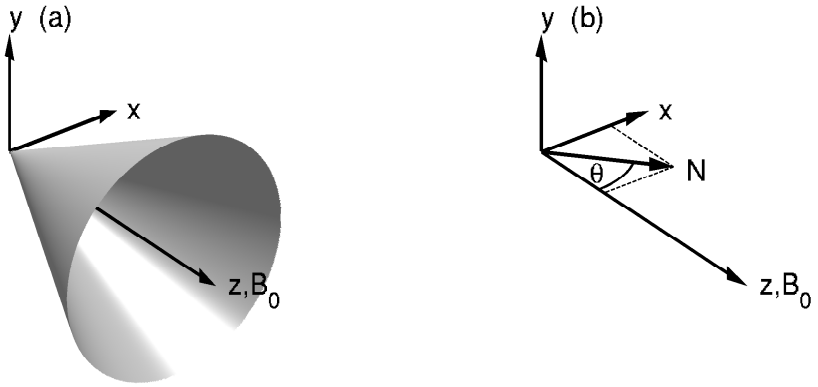

Figure 2.1: (a) Conical surface along which the index of refraction is constant. (b) Convention for the coordinate system used to describe wave propagation.

the permeability of vacuum $\mathbf{B} = \mu_0 \mathbf{H}$ to a good approximation [59]. One of the eigenvalues of (2.3a) is the desired dispersion relation. In oder to keep the result for the dispersion relation simple the symmetries of the problem are exploited. As depicted in figure 2.1, the ambient magnetic field $\mathbf{B}_0$ is chosen to point in the z-direction and $\mathbf{N}$ is embedded in the xz-plane. The angle between $\mathbf{N}$ and $\mathbf{B}_0$ is called θ. Due to rotational symmetry with respect to the $\mathbf{B}_0$-axis the problem is a plane problem, no azimuthal dependencies will occur. Thus, the index of refraction vector is given by

$$\mathbf{N} = \begin{pmatrix} N_x \\ 0 \\ N_z \end{pmatrix} = |\mathbf{N}| \begin{pmatrix} \sin\theta \\ 0 \\ \cos\theta \end{pmatrix} . \tag{2.4}$$

As a consequence of the azimuthal symmetry the index of refraction is constant along cones around the z-axis. The dielectric tensors used in the following are found to posses a similar structure

$$\underline{K} = \begin{pmatrix} K_1 & K_2 & 0 \\ -K_2 & K_1 & 0 \\ 0 & 0 & K_3 \end{pmatrix} = \begin{pmatrix} S & -iD & 0 \\ iD & S & 0 \\ 0 & 0 & P \end{pmatrix} \tag{2.5}$$

from which two important combinations of the tensor elements are deducted

$$R = S + D \,, \tag{2.6a}$$

$$L = S - D \,. \tag{2.6b}$$

The parameters S,P,D,R and L are also called the Stix parameters [60]. Equation (2.3a) in this coordinate system is given by

$$\begin{pmatrix} S - \mathbf{N}^2 \cos^2\theta & -iD & \mathbf{N}^2 \cos\theta \sin\theta \\ iD & S - \mathbf{N}^2 & 0 \\ \mathbf{N}^2 \cos\theta \sin\theta & 0 & P - \mathbf{N}^2 \sin^2\theta \end{pmatrix} \begin{pmatrix} E_x \\ E_y \\ E_z \end{pmatrix} = 0 \,. \tag{2.7}$$

If equation (2.7) has non-trivial solutions its determinant of coefficients needs to vanish. The solution of the determinant in terms of the index of diffraction **N** or alternatively the propagation angle θ is given by

$$A = S\sin^2\theta + P\cos^2\theta\ , \quad (2.8a) \qquad B = RL\sin^2\theta + PS(1+\cos^2\theta)\ , \quad (2.8b)$$

$$C = PRL\ , \quad (2.8c) \qquad F^2 = B^2 - 4AC\ , \quad (2.8d)$$

$$\mathbf{N}^2 = \frac{B \pm F}{2A}\ , \quad (2.8e) \qquad \tan^2\theta = -\frac{P\left(\mathbf{N}^2 - R\right)\left(\mathbf{N}^2 - L\right)}{\left(S\mathbf{N}^2 - RL\right)\left(\mathbf{N}^2 - P\right)}\ . \quad (2.8f)$$

The phase velocity inside the plasma is calculated from

$$v_{ph} = \frac{c}{|\mathbf{N}|} = \frac{\omega}{|\mathbf{k}|}\ , \tag{2.9}$$

where v_{ph} is directed parallel to **N**. The resonances and cut-offs are calculated from

$$N \to \infty \Leftrightarrow \tan^2\theta_{res} = -\frac{P}{S}\ , \quad (2.10a) \qquad N \to 0 \Leftrightarrow \tan^2\theta_{cut} = C\ , \quad (2.10b)$$

where the wave is absorbed at resonances and reflected at cut-offs. As the results show for each frequency there is an angle of propagation for which the corresponding wave has a cut-off or resonance. Waves are classified by their frequency, wavelength and polarization. In the case of propagation parallel to the ambient magnetic field the dispersion relation of three waves with different polarizations can directly be determined from (2.8f)

$$P = 0\ , \quad (2.11a) \qquad N_R^2 = R\ , \quad (2.11b) \qquad N_L^2 = L\ , \quad (2.11c)$$

where the polarization is defined by

$$\mathcal{P} = \frac{iE_x}{E_y} = \frac{N^2 - S}{D} = \frac{2N^2 - (R+L)}{R-L} = \begin{cases} +1\ (N^2 = R) \\ -1\ (N^2 = L) \end{cases}\ . \tag{2.12}$$

The equations (2.11) describe plasma oscillations (a), waves with right-handed circular polarization (b), from here on called R-waves, and waves with left-handed circular polarization (c), from here on called L-waves. Since the dielectric tensor is related to the conductivity tensor $\underline{\sigma}$

$$\underline{K} = \left(\mathbb{1} - \frac{\underline{\sigma}}{i\omega\epsilon_0}\right)\ , \tag{2.13}$$

which is in turn given by by the current

$$\mathbf{J} = \underline{\sigma}\cdot\mathbf{E} = \sum_s n_s q_s \mathbf{v}_s\ , \tag{2.14}$$

the plasma properties enter the theory through the currents in the plasma. The index s denotes the particle species in equation (2.14), n denotes the density, q

the charge and v the velocity of the corresponding species. Hence, if the general form of the current in a plasma is known the dispersion relation of the plasma can be calculated. Different models of the plasma may be chosen to compute the current, e.g. hot or cold plasma. The current is computed from the corresponding plasma particles equation of motion. In order to increase the insight into the parameter dependency of the dispersion relation it is expressed in the following set of dimensionless parameters

$$\psi = k\delta \,, \tag{2.15a}$$

$$\delta = \frac{c}{\omega_{pe}} \,, \tag{2.15b}$$

$$\chi = \frac{\omega}{\omega_{ce}} \,, \tag{2.15c}$$

$$\gamma = \frac{\omega_{ce}}{\omega_{pe}} \,, \tag{2.15d}$$

$$\iota = \frac{\theta}{\theta_{res}} \,, \tag{2.15e}$$

$$\nu = \frac{\nu_{eff}}{\omega_{ce}} \,, \tag{2.15f}$$

$$\theta_{res} = \arccos(x) \,, \tag{2.15g}$$

$$\beta = \frac{nk_BT_e}{B_0^2/2\mu_0} \,, \tag{2.15h}$$

where k is the wave vector and ω the waves angular frequency. Moreover, δ is the collisionless skin depth, c is the velocity of light and ω_{pe} is the plasma frequency. The electron cyclotron frequency is termed ω_{ce} and $\nu_{eff} = \nu_{en} + \nu_{ei}$ is an effective collision frequency including electron-neutral (ν_{en}) and electron-ion (ν_{ei}) collisions. An important quantity for the description of kinetic effects on wave propagation is the plasma-β, which is given by the ratio of plasma pressure $p_{plasma} = nk_BT_e$ to magnetic pressure $p_{mag} = B_0^2/2\mu_0$.
An advantage of the formulation in dimensionless parameters is a simple classification of plasmas concerning plane wave propagation. All plasmas with the same parameters γ, ν and β have similar properties concerning R- and L-wave propagation. This can be used to draw conclusions on wave propagation in space plasmas from wave propagation in a laboratory device.

2.2 Cold Plasma Dispersion Theory

The equation of motion in the single particle picture including collisions is given by

$$m_s \frac{d\mathbf{v}_s}{dt} = q_s \left(\mathbf{E} + \mathbf{v}_s \times \mathbf{B}\right) - m_s \mathbf{v}_s \nu_{s,eff} \ . \tag{2.16}$$

Collisions are modeled by the term containing the collision frequency $\nu_{s,eff}$. This treatment of collisions was developed by Krook *et al.* [61, 62] and represents a simplification of the exact collision operator, e.g. the energy is not conserved in the model. Effectively, the term describes the momentum exchange of the concerned particle species with one or several other species in the plasma, e.g. electrons with neutrals and ions. The velocities defined by (2.16) are used to calculate the corresponding current as defined in (2.14) which leads to the following dielectric tensor if plane wave propagation is assumed

$$K_1 = 1 - \sum_s \frac{\omega_{ps}^2 \left(\omega + i\nu_s\right)}{\omega \left[\left(\omega + i\nu_s\right)^2 - \omega_{cs}^2\right]} \ , \tag{2.17a}$$

$$iK_2 = \sum_s \frac{\epsilon_s \omega_{cs} \omega_{ps}^2}{\omega \left[\left(\omega + i\nu_s\right)^2 - \omega_{cs}^2\right]} \ , \tag{2.17b}$$

$$K_3 = 1 - \sum_s \frac{\omega_{ps}^2}{\omega \left(\omega + i\nu_s\right)} \ , \tag{2.17c}$$

where ϵ_s is the sign of particle species s electric charge. The dispersion relation for propagation at arbitrary angles can be calculated using equation (2.8e). In the following a single ion-species argon plasma is assumed in the calculations consisting of ions and electrons, which posses a mass ratio of

$$\frac{m_e}{m_i} \approx \frac{1}{73000} \ . \tag{2.18}$$

Since the expression for the general dispersion relation is rather complex and contains contributions from waves with several polarizations it is desirable to derivate less complex expressions which describe waves with a single polarization. In the quasi-parallel approximation [63, 60]

$$\frac{\omega^2 \omega_{ce}^2 \sin^4(\theta)}{4(\omega^2 - \omega_{pe}^2)^2 \cos^2(\theta)} \ll 1 \ , \tag{2.19a}$$

$$\frac{\omega_{ce}^2 \sin^2(\theta)}{\mid 2(\omega^2 - \omega_{pe}^2) \mid} \ll 1 \ , \tag{2.19b}$$

expressions for the dispersion relation of R- and L-waves are derived which are considerably less complex than the full dispersion relation and describe wave propagation at arbitrary angles to the ambient magnetic field. In this approximation the dispersion relations for R- and L-waves are given by

$$\mathbf{N}_R^2 = 1 - \frac{\omega_{pe}^2}{\omega(\omega - \omega_{ce}\cos\theta)} \ , \tag{2.20a}$$

$$\mathbf{N}_L^2 = 1 - \frac{\omega_{pe}^2}{\omega(\omega + \omega_{ce}\cos\theta)} \ . \tag{2.20b}$$

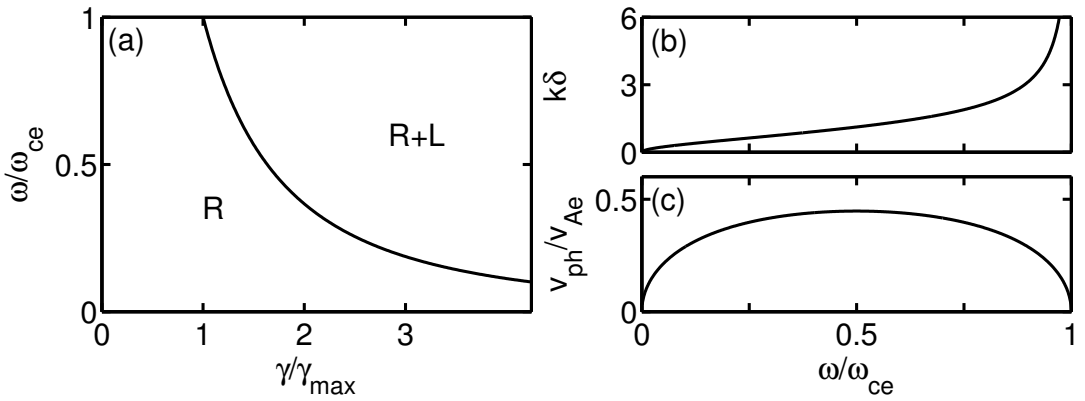

Figure 2.2: (a) Possible polarizations over plasma parameter γ and normalized frequency. (b) Normalized dispersion relation of R-waves for $\gamma = \gamma_{max}$. (c) Phase velocity normalized to the electron Alfvén velocity $v_{Ae} = c\omega_{ce}/\omega_{pe}$.

Collisions can be included in the dispersion relation (2.20) by a replacement of the electron mass by

$$m_e \to m_e \left(1 + i\frac{\nu_{eff}}{\omega}\right). \tag{2.21}$$

Resonance ω_{res} and cut-off ω_L^R frequencies in this approximation are given by

$$N_R \to \infty \Leftrightarrow \omega_{res} = \omega_{ce}\cos\theta\,, \tag{2.22a}$$

$$N \;\to\; 0 \Leftrightarrow \omega_L^R \;= \pm\frac{\omega_{ce}\cos\theta}{2} + \sqrt{\left(\frac{\omega_{ce}\cos\theta}{2}\right)^2 + \omega_{pe}^2}\,. \tag{2.22b}$$

There is an additional resonance for the L-wave not included in the quasi parallel approximation. However, in an argon plasma the L-wave resonance frequency is very small compared to the cut-off frequency of the R-wave resonance frequency given in equation (2.22) and can therefore be neglected. The dispersion relation (2.20a) reformulated in the dimensionless parameters defined in equations (2.15) is given by

$$\psi^2 = \chi^2\gamma^2 - \frac{\chi}{\chi + i\nu - \cos(\iota\theta_{res})}\,. \tag{2.23}$$

If wave propagation is parallel ($\iota = 0$) and the plasma is assumed collisionless ($\nu = 0$) propagation depends on a single parameter termed γ. Hence, also the L- and R-wave cut-off frequency depend only on γ. Both transversal polarized waves can propagate for frequencies smaller than their resonance and larger than their cut-off frequencies. There exists a γ range in which the L-wave cut-off is larger than the electron cyclotron frequency. For

$$\gamma \le \gamma_{max} = \frac{1}{\sqrt{2}}\,. \tag{2.24}$$

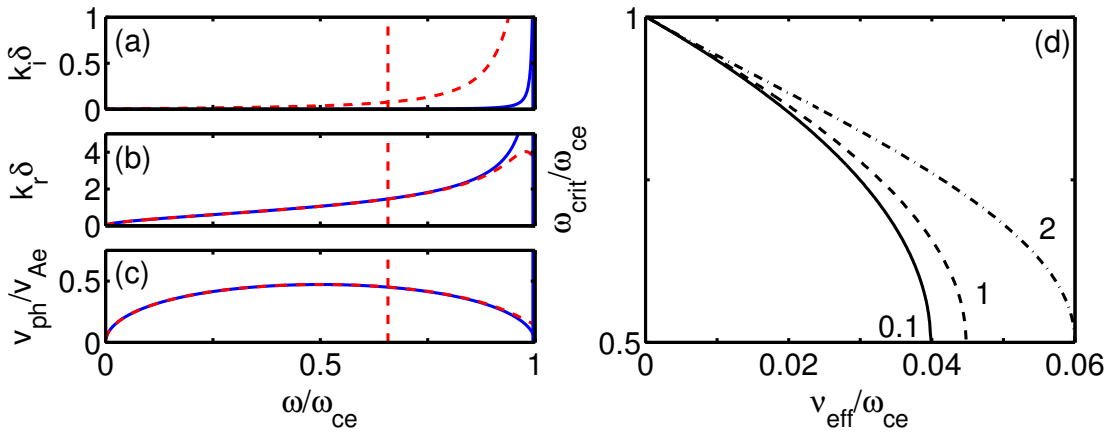

Figure 2.3: Cold plasma dispersion relation for $\nu = 0.001$ (full lines) and $\nu = 0.04$ (dashed lines), where $\gamma = \gamma_{max}$. (a) Spatial damping increment and (b) the wave vector, both normalized to the skin-depth δ. (c) Phase velocity normalized to the electron Alfvén velocity over frequency. The critical frequencies for both cases are marked by vertical lines. The critical frequency over the collision frequency for three different ratios of γ/γ_{max} is shown in (d).

the R-wave is the only transversal wave for frequencies between the L-wave and R-wave resonance. As depicted in figure 2.2 (a) for $\gamma > \gamma_{max}$ R- and L-waves can occur simultaneously even for frequencies smaller than the electron cyclotron frequency. A typical result for the parallel dispersion relation is depicted in figure 2.2 (b) for $\gamma = \gamma_{max}$. The phase velocity normalized to the electron Alfvén velocity is depicted in figure 2.2 (c). The dependency of the parallel dispersion relation on γ is weak for $\gamma \leq \gamma_{max}$. If $\gamma \leq 0.1\gamma_{max}$ the dispersion relation becomes completely independent of γ. Typical findings are the increase of the normalized wave vector with increasing frequency. Furthermore, the phase velocity has a peak value of about half the electron Alfvén velocity at $\omega = 0.5\omega_{ce}$ and minima at $\omega = 0$ and $\omega = \omega_{ce}$. The R-wave in this frequency range is called whistler wave within the context of this thesis. Since wave propagation is not restricted to parallel propagation and collisions are important in many practical situations it is necessary to investigate the influence of those modifications on the whistler wave parameter window.

2.2.1 Effects of Collisions

If the collision frequency is non-zero the result for the dispersion relation is complex valued, where the imaginary part of k is the spatial damping increment k_i due to collisions defining a spatial damping length $\tau = 1/k_i$ and the real part k_r is related to the wave length $\lambda = 2\pi/k_r$. The spatial damping is considered strong if the

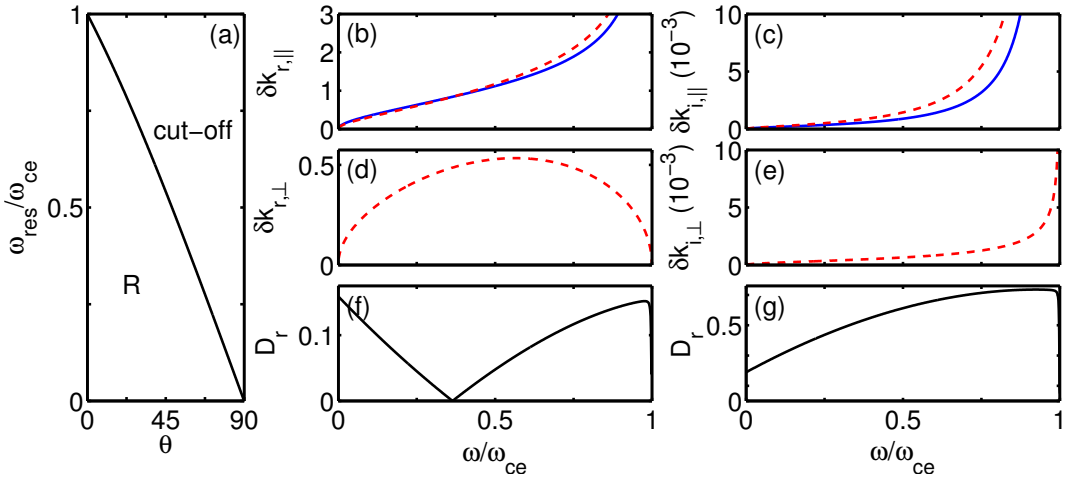

Figure 2.4: (a) Resonance frequency over propagation angle. (b-g) Comparison of quantities for parallel propagation (full line) with quantities for propagation at half the resonance cone angle (dashed lines).

damping length is equal or smaller than the wave length

$$\frac{\tau}{\lambda} \leq 1 \, . \tag{2.25}$$

The frequency at which $\tau/\lambda = 1$ is called critical frequency ω_{crit}. In figure 2.3 (a) the frequency dependency of k_i is depicted. If the frequency is small the damping is weak and vice versa, where a continuous increase is found between small and large frequencies. Thus, for frequencies smaller than the critical frequency the damping is weak and above it is strong. In the case of small ν the spatial damping decrement k_i is small up to $\omega \lesssim \omega_{ce}$, above a certain onset frequency it increases strongly and approaches its maximum value $\omega = \omega_{ce}$. Thus, the resonance vanishes and instead a strong damping of the wave is found. If ν increases collisions are more frequent in the plasma and the spatial damping increment increases, as a comparison between the two cases in figure 2.3 (a) shows. A difference in the wave vector between the case with weak and strong damping depicted in 2.3 (b) is negligible below the critical frequency for the case with strong damping. Consequently, the same holds for the phase velocity depicted in figure 2.3 (c). Hence, the major difference between the cases depicted occurs in the spatial damping increment. The critical frequencies for both cases are depicted as vertical lines illustrating the dependency of the damping on the normalized collision frequency ν. In figure 2.3 (d) the normalized critical frequency is shown over the normalized collision frequency for several values of γ. A weak dependency of the critical frequency is found for $\gamma \leq \gamma_{max}$ and the dependency is negligible for $\gamma \leq 0.1\gamma_{max}$ if the collision frequency is not too large. Hence, for small $\nu \lesssim 0.001$ the damping at frequencies $\omega \leq 0.9\omega_{ce}$ and its γ dependency for $\gamma \leq \gamma_{max}$ can be neglected. The wave length of the R-wave and the L-wave cut-off are almost the same as in the collisionless case and the whistler wave parameter window stays unchanged for $\nu \lesssim 0.001$.

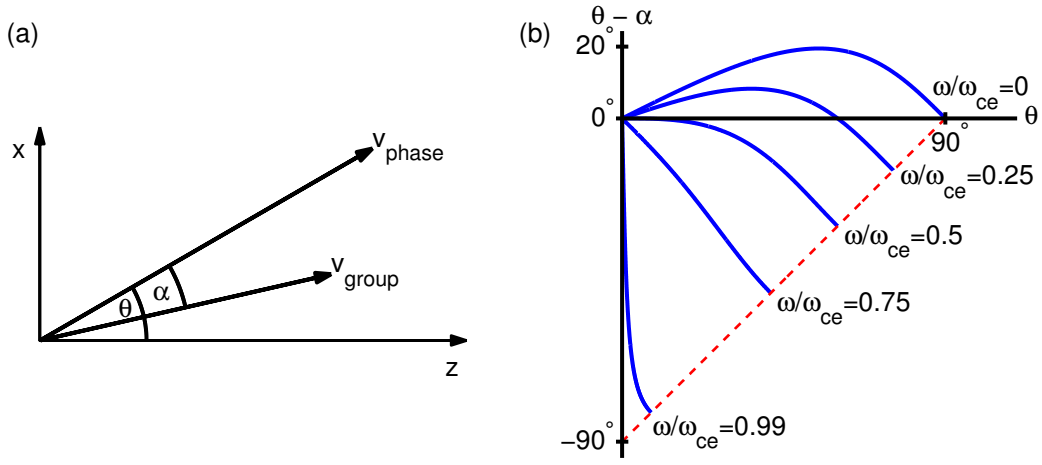

Figure 2.5: (a) Definition of the group velocity angle $\theta - \alpha$, where θ is the phase velocity angle relative to $\mathbf{B}_0$ and α is the angle between phase and group velocity. (b) Group velocity angle over phase velocity angle, the dashed line shows the resonance cone angle. Shown are curves for five different values of ω/ω_{ce}.

2.2.2 Effect of Oblique Propagation

If oblique propagation is included in addition to collisions and $\gamma \leq \gamma_{max}$ the limit for the whistler wave propagation window is given by the resonance cone angle, as depicted in figure 2.4 (a). Figure 2.4 (b) shows the dependency of the parallel wave length on the frequency for a normalized collision frequency of $\nu = 0.001$ and two propagation angles. Depicted are the curves for parallel propagation and propagation at half the resonance cone angle. The relative difference $D_r = |\delta k_{r,||}(\theta = 0) - \delta k_{r,||}(\theta = 0.5\theta_{res})|/\delta k_{r,||}(\theta = 0)$ between the parallel wave lengths is depicted in figure 2.4 (f) and is found to be small. Although the perpendicular wave length shown in figure 2.4 (d) is not negligible. The dependency of the spatial damping increment on the propagation angle is depicted in figures 2.4 (c), (e) and (g) in the same manner. The parallel spatial damping increment shows a considerably larger difference between parallel and oblique propagation than the wave length. However, the critical frequencies at the depicted propagation angles are larger than $\omega/\omega_{ce} = 0.99$ and decrease only slightly with increasing propagation angle if the angles are not to close to the resonance cone angle. Thus, for wave propagation angles smaller than or equal half the resonance angle the whistler wave parameter window does not change.

Anisotropic Propagation Features

The group velocity describes the energy flow of the wave. Due to the anisotropy induced by the ambient magnetic field the whistler wave group velocity does not point in the same direction as the phase velocity if the wave propagates oblique.

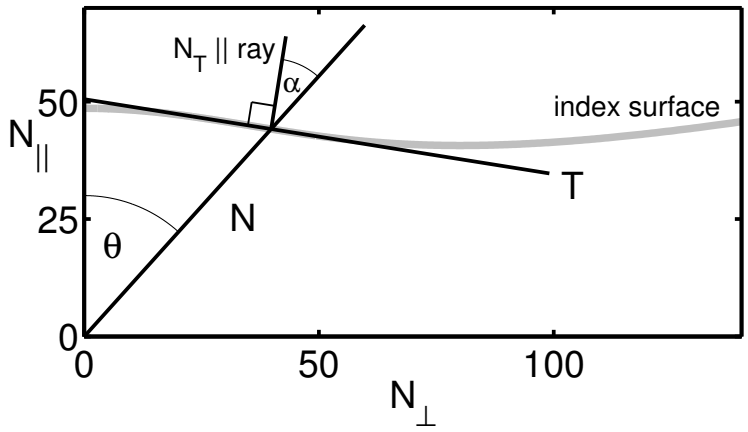

Figure 2.6: Construction of the group velocity direction from the refractive-index surface. Thick Line: Index surface of dispersion relation (2.23) for $\gamma = 0.05$ and $\omega/\omega_{ce} = 0.23$.

The magnitude of group and phase velocity generally differ from each other. If the frequency is held fixed both velocities have their largest values for parallel propagation. If the propagation angle is increased the magnitude of phase and group velocity decreases monotonically. The group velocity is defined by

$$\mathbf{v}_g = \frac{\partial \omega}{\partial \mathbf{k}} = \frac{\partial \omega}{\partial k}\mathbf{e}_\mathbf{k} + \frac{1}{k}\frac{\partial \omega}{\partial \theta}\mathbf{e}_\theta \ , \tag{2.26}$$

where $\mathbf{e}_\mathbf{k}$ is the unit vector parallel to the wave vector $\mathbf{k}$ and $\mathbf{e}_\theta$ is the unit vector perpendicular to $\mathbf{e}_\mathbf{k}$. If the dispersion relation for whistler waves (2.23) is used the result for the angle between the group velocity and the ambient magnetic field is found to be

$$(\theta - \alpha) = \arctan\left(\frac{\sin(\theta)\,(\cos(\theta) - 2\omega/\omega_{ce})}{1 + \cos(\theta)\,(\cos(\theta) - 2\omega/\omega_{ce})}\right) \ . \tag{2.27}$$

The θ dependency of the group velocity angle $(\theta + \alpha)$ is relatively complex, but the dependency on the ratio ω/ω_{ce} can be described in simple terms. Figure 2.5 shows the group velocity angle $\theta - \alpha$ for five characteristic values of ω/ω_{ce}. If $\omega/\omega_{ce} < 0.5$ the group velocity angle is positive until a certain θ_{lim} is reached, above this θ_{lim} the angle becomes negative. The group velocity angle is always negative for $\omega/\omega_{ce} \geq 0.5$. An important property of the group velocity angle in figure 2.5 is its small value up to frequencies of $\omega/\omega_{ce} = 0.4$ of less than 20°. This behavior is called focusing [9]. In this frequency range the whistler wave energy flow is mainly along the ambient magnetic field. This effect becomes weaker and gets lost completely at high frequencies. Hence, the guiding of the energy flow by the ambient magnetic field is strong for low frequencies and weak for high frequencies.

A very useful way to illustrate the group velocity direction is achieved by the use of the refractive index surface, as depicted in figure 2.6. This surface is given

by the dispersion relation and shows the dependency of the index of refraction on the propagation angle θ. The trajectory of the refractive index vector is displayed in the refractive index space. In the examples shown here this space is two dimensional, the ordinate represents the component of the refractive index vector parallel to $\mathbf{B}_0$ and the abscissa perpendicular to $\mathbf{B}_0$. The surface is constructed from this representation by revolution about the ordinate. All parameters in the dispersion relation except of the propagation angle θ are held constant. Each point on this surface represents a specific angle of propagation θ_i, the corresponding angle of the group velocity is given by the normal N_T to the tangent T at $\mathbf{N} = \mathbf{N}(\theta)$ [64, 10]. The group velocity direction is alternatively termed ray direction.

2.3 Hot Plasma Dispersion Relation

The previous results for the cold plasma dispersion relation considered only collisional damping. In a finite temperature plasma also non-collisional damping of waves is possible. Since even a low-temperature plasma is subject to both collisional and non-collisional damping a dispersion relation including this effect is needed in order to achieve an accurate description of wave propagation. Therefore, the hot plasma dispersion relation including all kinetic effects is utilized in the approximation of parallel propagating waves for frequencies $\omega \gg \omega_{ci}$. In order to include a finite temperature in the dispersion relation it is convenient to describe the plasma by particle distribution functions f_s describing the velocity distribution of each species in the plasma. The time evolution of those particle distribution functions is described by the Boltzmann equation

$$\frac{\partial f_s}{\partial t} + \mathbf{v} \cdot \nabla f_s + \frac{q_s}{m_s} (\mathbf{E} + \mathbf{v} \times \mathbf{B}) \cdot \nabla_v f_s = \left(\frac{\delta f_s}{\delta t} \right)_{coll} . \tag{2.28}$$

Instead of the exact Boltzmann collision operator collisions are modeled by the Krook model [61, 62]

$$\left(\frac{\delta f_s}{\delta t} \right)_{coll} = -\nu_{eff} (f_s - f_{0,s}) . \tag{2.29}$$

If an isotropic Maxwellian velocity distribution of the plasma particles is chosen

$$f_{0,s} \left(v^2 \right) = \frac{1}{(\sqrt{\pi} v_{th,s})^3} e^{-v^2 / v_{th,s}^2} , \tag{2.30}$$

where $v_{th,s} = \sqrt{2 k_B T_s / m_s}$, and only parallel propagation is taken into account the dielectric tensor is given by

$$K_1 = 1 + \frac{1}{2} \sum_{s,m=\pm 1} \frac{\omega_{ps}^2}{\omega k v_s} Z_{ms} , \tag{2.31a}$$

$$K_2 = -\frac{i}{2} \sum_{s,m=\pm 1} m \frac{\varepsilon_s \omega_{ps}^2}{\omega k v_s} Z_{ms} , \tag{2.31b}$$

$$K_3 = 1 - \sum_s \frac{\omega_{ps}^2}{\omega k v_s} \zeta_{0s} Z'_{0s} . \tag{2.31c}$$

In the expression for the dielectric tensor the plasma dispersion function Z_{ms} [65] occurs which is a transcendental function defined by

$$Z_{ms} = \frac{1}{\sqrt{\pi}} \int_{-\infty}^{\infty} \frac{e^{-\xi^2}}{\xi - \zeta_{ms}} d\xi , \qquad Im \left(\zeta_{ms} \right) > 0 , \qquad \zeta_{ms} = \frac{\omega + m \omega_{cs} + i \nu_{eff}}{k v_{th}} . \tag{2.32}$$

In order to achieve this result a first order linearization in the fields and the particle distribution function is performed [66, 67, 59], which is valid only if the field

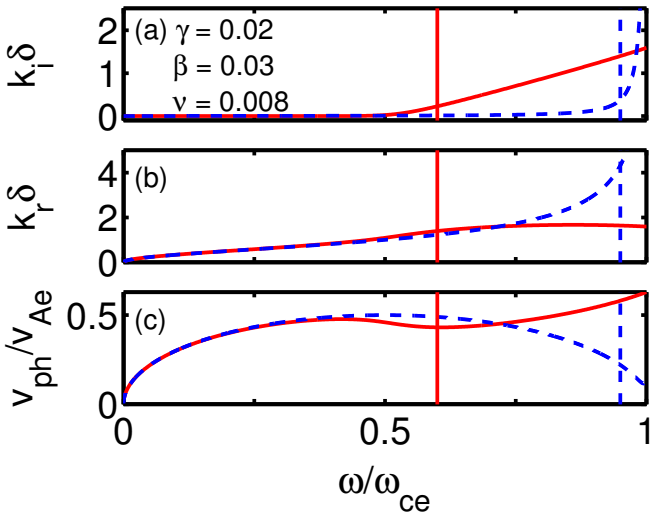

Figure 2.7: Comparison between the dispersion relation in a hot plasma (full line) and a cold plasma (dashed line). Corresponding critical frequencies are indicated by vertical lines.

amplitudes are small against the ambient magnetic field. The R-wave dispersion relation in this plasma model is of special interest in the limit in which the ion terms can be neglected. In this limit it is given by [68]

$$\mathbf{N}_R^2 = 1 + \frac{\omega_{pe}^2}{\omega k v_{th}} Z\left(\zeta_{-1e}\right) \ . \tag{2.33}$$

Since the plasma is described by particle distribution functions all kinetic effects are included in the description of parallel propagating R-waves. In dimensionless variables the dispersion relation is given by

$$\psi^2 = \gamma^2\chi^2 + \frac{\chi}{\psi\sqrt{\beta}} \cdot Z\left(\frac{\chi + i\nu - 1}{\psi\sqrt{\beta}}\right) \ . \tag{2.34}$$

Since (2.34) is an implicit equation which can not be solved analytically for ψ Newtons method [69] is applied for a fixed frequency. As the initial value for the routine the ψ calculated from the cold plasma dispersion relation of (2.23) may be used. A very crucial point for the numerical accuracy of the computation is the determination of the plasma dispersion function. Several routines for the calculation of the plasma dispersion function are known [70, 71, 72], which calculate the dispersion function accurate to a certain numbers of decimals. A method with a high accuracy of at least ten decimals is used for the computation of the dispersion relation [72]. The code for the computation was implement by Sauer *et al.* [73]. Figure 2.7 shows a comparison between typical results for the dispersion relation of a cold plasma and a hot plasma for the case of small γ, relatively high electron plasma-β and small collisionality $\nu \ll 1$, as the parameters in figure 2.7 (a) show. In the cold plasma the wave is damped exclusively by collisions, while in

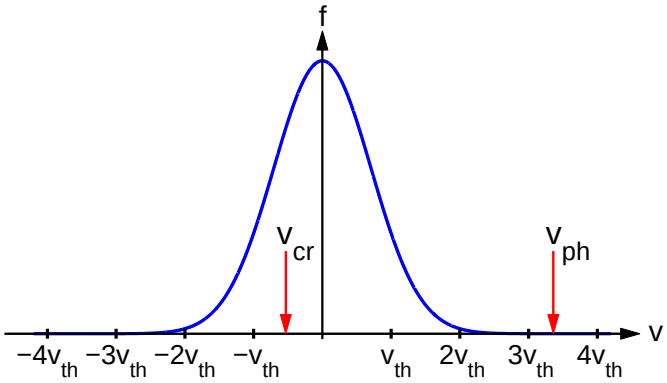

Figure 2.8: Maxwellian velocity distribution function describing the particle velocities along $\mathbf{B}_0$. Plotted is the velocity in units of the thermal velocity along the abscissa and the probability density along the ordinate. Red arrows show the phase velocity and the cyclotron resonance velocity respectively for the plasma parameters indicated in figure 2.7 and $\omega/\omega_{ce} = 0.86$.

the hot plasma damping by collisions and kinetic effects is included. The critical frequencies for both cases are indicated by vertical lines exhibiting a considerable difference. In the cold plasma $\omega_{crit}/\omega_{ce} = 0.95$ while $\omega_{crit}/\omega_{ce} = 0.6$ in the hot plasma. As depicted in figures 2.7 (b-c), for frequencies larger than the critical frequency of the hot plasma also the wave vector and phase velocity of both cases differ from each other. Hence, an increased damping at high frequencies is predicted by the hot plasma dispersion relation which is due to a kinetic effect. This damping is called cyclotron damping and is due to the velocity distribution of the electrons, which causes a distribution in the relative velocity between the electrons and the whistler wave. Cyclotron damping is caused by the interaction of the whistler wave with a group of electrons called resonant electrons [74]. Electrons are resonant if the Doppler shifted frequency of the whistler wave in the frame moving with the electrons is equal to the electron cyclotron frequency. Hence, the parallel velocity of the electrons together with the parallel velocity of the wave v_{ph} determines the frequency shift as illustrated in figure 2.8. The velocity of the resonant electrons for a certain whistler wave frequency is called cyclotron resonance velocity v_{cr}. A large quantity of resonant particles at this velocity means strong damping and vice versa. The resonance velocity is m times the thermal velocity if

$$\chi_m = 1 - m\sqrt{\beta}\psi_m \ , \tag{2.35}$$

which is a consequence of the Doppler shift in the frequency experienced by the electrons. Figure 2.9 shows the frequency at which condition (2.35) is fulfilled for $m = 1 - 3$ over β in the parameter range $\gamma, \nu \ll 1$. Furthermore, the critical frequency is depicted as a dashed curve. Since the number of resonant particles increases with decreasing m wave damping is stronger for frequencies larger than the critical frequency. Hence, the velocity of resonant particles decreases with increasing frequency and the onset of strong damping shifts to smaller frequencies

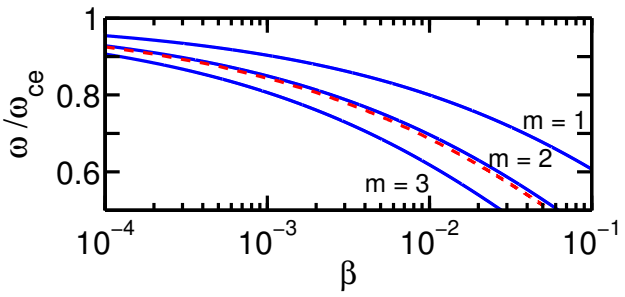

Figure 2.9: Frequency at which the resonant particles have m times thermal velocity (full lines) over β, where $m = 1 - 3$ and increases from top to bottom curve. The critical frequency at which damping length equals wave length is depicted for the case of small γ and ν (dashed line).

if β is increased. Cyclotron damping becomes strong if the wave has a frequency at which it couples to electrons having a speed of approximately two times the thermal velocity.

3 Data Processing

3.1 Cross-Power Spectrum

A cross-power spectral density of two signals $f_1(t)$ and $f_2(t)$

$$\mathcal{P}_\times\{f_1, f_2\}(\omega) = \mathcal{F}\{f_1(t)\}^* \cdot \mathcal{F}\{f_2(t)\} \tag{3.1}$$

is given by the product of the complex conjugate Fourier transform of signal f_1 with the Fourier transform of signal f_2. The time averaged phase difference between the signals $\Delta\phi$ at a frequency ω is given by

$$\Delta\phi(\omega) = \tan\left(\frac{Im\mathcal{P}_\times(\omega)}{Re\mathcal{P}_\times(\omega)}\right) , \tag{3.2}$$

where frequency and phase shift between the signals are assumed constant during the sampling time. Due to averaging, noise in the signals is strongly reduced [75]. If time dependent measurements of a wave field are performed along a certain axis z the wave length of the wave is calculated using (3.2). The phase shift between the wave excitation signal

$$f_r(t) = A_r \exp\left[i(-\omega t + \phi_r)\right] \tag{3.3}$$

and measured wave signal

$$f_w(t) = A_w \exp\left[i(k_z z - \omega t + \phi_w)\right] \tag{3.4}$$

is given by

$$\Delta\phi = k_z z + \phi_w - \phi_r \ . \tag{3.5}$$

Hence, the wave vector component along this axis is given by

$$\frac{\partial\Delta\phi}{\partial z} = k_z \tag{3.6}$$

from which the wave length is calculated. This method is used to extract the phase and the wave vector from time series measured in experiments.

3.2 Hilbert Transform

The Hilbert transform $\mathcal{H}$ of a real valued signal $f(x)$ is given by

$$g(x) = \mathcal{H}\{f(x)\} = \frac{1}{\pi} \int_{-\infty}^{+\infty} \frac{f(y)}{x-y} dy \; . \tag{3.7}$$

$g(x)$ represents the signal phase shifted by 90°. This property is exploited in order to calculate instantaneous properties of the signal. Therefore, the analytical signal is computed

$$f_a(x) = f(x) + ig(x) \; . \tag{3.8}$$

Thus, the instantaneous amplitude A_{in} and phase ϕ_{in} of the signal are given by

$$A_{in} = \sqrt{f_a(x) \cdot f_a^*(x)} \; , \tag{3.9a}$$

$$\phi_{in} = \tan\left(\frac{g(x)}{f(x)}\right) \; . \tag{3.9b}$$

In order to calculate $f_a(x)$ in practice its properties in Fourier space are used [75], which allows an efficient computation of $f_a(x)$. The procedure is used to compute instantaneous properties from simulations.

3.3 Helmholtz Decomposition

According to the fundamental theorem of vector calculus any vector field in three dimensions can be resolved into the sum of a curl-free vector field and a divergence-free vector field. This is known as the Helmholtz decomposition [76]. If a Helmholtz decomposition is applied to the electric field of a wave the source of the curl-free field is the fluctuating space charge and the curl of the divergence-free field is induction, or in other words the rotation of the electric field. Therefore, the divergence-free field is called inductive electric field $\mathbf{E}_{ind}$ and the curl-free field electrostatic field $\mathbf{E}_{es}$, also termed space charge electric field. The sum of both fields gives the total electric field

$$\mathbf{E} = \mathbf{E}_{es} + \mathbf{E}_{ind} \; . \tag{3.10}$$

Besides their causation the electrostatic and the inductive field differ also in their direction relative to the wave vector $\mathbf{k}$ in Fourier space. The inductive electric field is perpendicular, while the electrostatic field is always parallel to the wave vector

$$\nabla \cdot \mathbf{E}_{ind} = 0 \Rightarrow \mathbf{k} \cdot \mathcal{F}\{\mathbf{E}_{ind}\} = 0 \; , \tag{3.11a}$$

$$\nabla \times \mathbf{E}_{es} = 0 \Rightarrow \mathbf{k} \times \mathcal{F}\{\mathbf{E}_{es}\} = 0 \; . \tag{3.11b}$$

In the application of the Helmholtz decomposition to simulation data the properties in Fourier space are exploited to compute the inductive electric field from the total electric field

$$\mathcal{F}\{\mathbf{E}_{ind}\} = -\frac{\mathbf{k} \times \mathbf{k} \times \mathcal{F}\{\mathbf{E}\}}{k^2} \,. \tag{3.12}$$

Since the total electric field is known the electrostatic field is computed by solving (3.10).

4 Propagation in a Cylindrical Plasma

Plasma inhomogeneities modify wave propagation. Under certain conditions the waves energy flow is guided by density enhancements, called density crests. A simple model assuming the validity of geometric optics and whistler waves launched from a point source is used to illustrate the effect of a density crest on wave propagation. Full-wave simulations of loop antenna excited whistler waves in a cylindrical plasma, are carried out in order to gather predictions on wave propagation in the experiments presented subsequently.

4.1 Whistler Wave Ducting

The anisotropy of a magnetized plasma causes a focusing effect which guides whistler waves along the magnetic field lines for low frequencies. Another important guiding is given by inhomogeneities in the plasma. Inhomogeneities form channels in which whistler waves are guided effectively [77] also at higher frequencies. The channels are called ducts and the guiding therefore ducting. In the following wave propagation in density crests with their symmetry axis aligned to the ambient magnetic field are investigated [10]. The concepts introduced in chapter 2.2 are used to perform predictions about the ducting of whistler waves in the approximation of geometric optics. If the variation of the plasma density is small above the wave length of the wave propagating in the plasma a simple graphical method exists which allows to calculate the direction of the ray trajectory $\mathbf{R}$. Since reflections are unimportant in this case only refraction effects have to be considered. Refraction at a boundary between two homogeneous media with refractive indices differing from each other is particular simple example for refraction. The direction of the waves ray trajectory in medium I $\mathbf{R}_1$ is given as an initial condition. The law of refraction states that the projection of the refraction index onto the z-axis seen by the wave in medium I must be equal to the one in medium II. Thus, the direction of the ray in medium II $\mathbf{R}_2$ is determined from the index of refraction surfaces of both media. This is accomplished in figure 4.1 (a). The initial conditions for P_1 determine $N_{||}$, which in turn determines P_2. Hence, the ray direction in medium II $\mathbf{R}_2$ is determined. This is used to depict the wave energy flow trajectories in space as depicted in figure 4.1 (b). The direction of the ray in medium I is constant while the wave propagates from P_1 to P_2. At P_2 the plasma density jumps from a low to a high value. Correspondingly the ray direction changes, which changes the direction of the waves energy flow. This result is

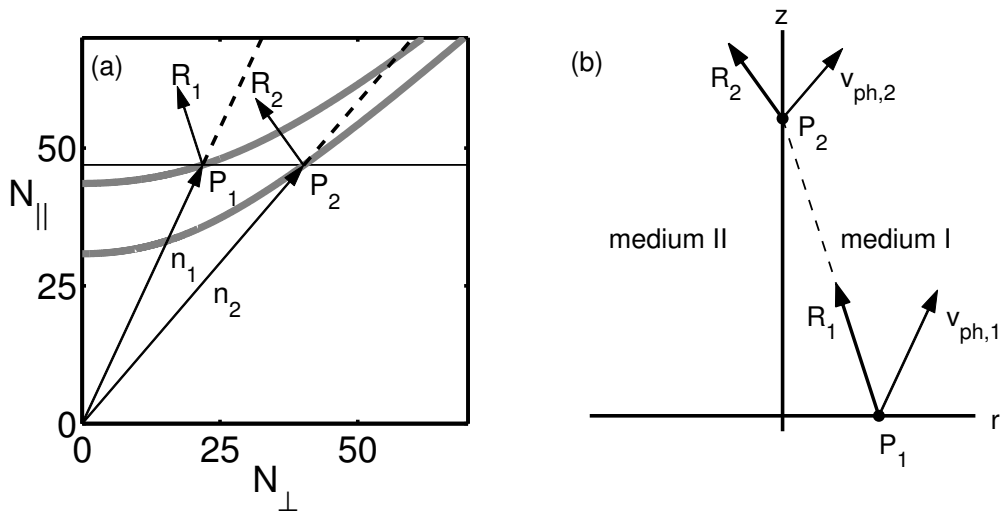

Figure 4.1: Graphical determination of the change in propagation direction at the boundary between two homogeneous media using the Snell's law and the index of refraction surface.

used to determine the energy flow trajectory in a density crest. Since a density crest exhibits a continuous instead of a step wise change in plasma density it is discretized into a large quantity of density slabs in the direction perpendicular to the ambient magnetic field. Wave propagation is initialized in the center of the crest. The construction just outlined is repeated at every density step in the discretized density crest. As depicted in figure 4.2 the whistler wave dispersion relation has the property to decrease the initial group velocity angle under certain conditions, while the wave propagates away from the central axis of the crest. This is the case if $\omega/\omega_{ce} < 0.5$ and the initial group velocity angle fulfills

$$\theta_1 \leq \arccos\left(2\frac{\omega}{\omega_{ce}}\right) \ . \tag{4.1}$$

Under those conditions the trajectory possesses a turning point at which the energy flow is parallel to the ambient magnetic field. The radial position of the turning point is given by

$$\frac{n(P)}{n(0)} = \frac{1-\omega/\omega_{ce}}{\cos\theta_1 - \omega/\omega_{ce}}\cos^2\theta_1 \ . \tag{4.2}$$

After the turning point has been passed the ray, and therefore the group velocity, is directed towards the plasma center until the energy flow trajectory crosses the plasma center. The pattern just described is repeated periodically leading to a wave energy flow which oscillates around the plasma center. Thus, the wave energy performs lateral excursions from the plasma center if the initial group velocity angle fulfills the condition (4.1). The group velocity of the wave changes continuously from low values in the plasma center to higher values at lower density

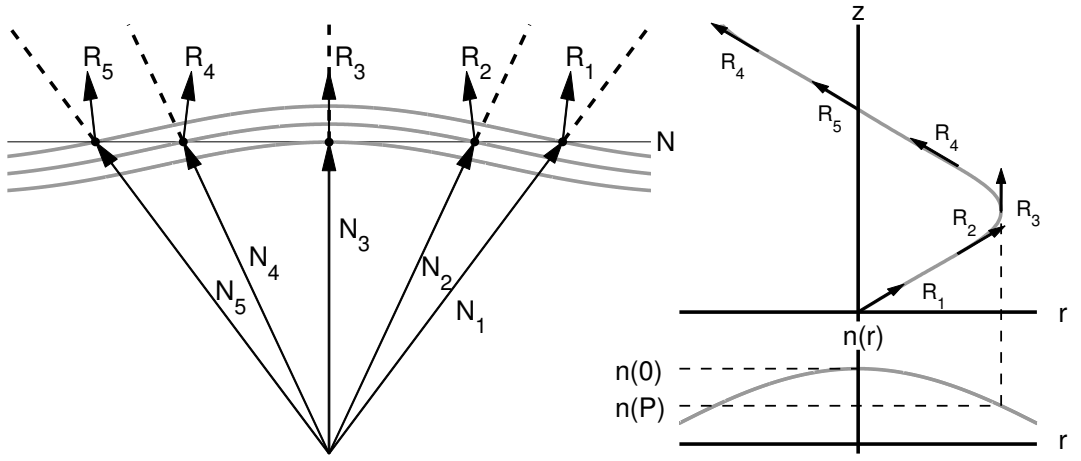

Figure 4.2: Graphical determination of the ray trajectory in a density crest. Depicted is a case in which the wave is launched in the center of the plasma with an angle θ_1 under which the wave is trapped in the density crest.

off the central axis. Simultaneously the wave travels a longer distance than in the case of propagation parallel to the ambient magnetic field. In many applications of practical importance the surplus in the distances cancels the surplus in the group velocity, which leads to a parallel group velocity equal to the one predicted for parallel propagation in the plasma center [43]. If wave damping is neglected the amplitude along the plasma center is not constant as in the case of parallel propagation but shows oscillations. At axial positions of maximum lateral excursion, the wave amplitude exhibits a minimum, while it shows a maximum at points at which the energy flow trajectory crosses the plasma center [78]. Those effects can become noticeable for density crests which have a density maximum exceeding the background plasma density about 10% depending on the plasma parameters [79].

4.2 Full-Wave Simulation

In order to perform predictions on whistler wave propagation in the general case, more sophisticated methods than just discussed are necessary, termed full-wave computations. Those are ab intio computations of the wave field based on the Maxwell equations. In the following a wave source extended in space is employed for wave excitation. The plasma is assumed cold and collisionless, which means kinetic effects are neglected. The ions are static and serve as a neutralizing background, only electron currents are accounted for. Since energy transfer from the wave or the wave source to the plasma is not included in the computations effects due to the heating of the plasma occurring in real physical systems are neglected. Perturbations on the plasma density due to the wave source or a detector system

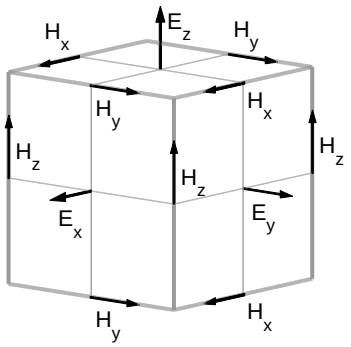

Figure 4.3: Illustration of the Yee cell in the Yee space lattice. The position of the fields computed in the cell are illustrated.

mapping the wave field are not present. Subsequently full-wave Finite-Difference Time-Domain (FDTD) computations of wave-fields using the IPF-FD3D [50] code are presented [80]. IPF-FD3D is an implementation of the Yee algorithm [81] which computes wave propagation in the most general case including all effects possible in the propagation of electromagnetic waves. The basic idea behind the algorithm is to use the Maxwell curl (2.1a)-(2.1b) and an appropriate grid to compute the time dependency of the electromagnetic fields on the grid points. In addition to the curl equations an equation describing the current in the plasma is needed. Hence, the following set of equations is solved numerically

$$\frac{\partial \mathbf{E}}{\partial t} = \frac{1}{\epsilon_0}\nabla \times \mathbf{H} - \frac{1}{\epsilon_0}\mathbf{J} \,, \tag{4.3}$$

$$\frac{\partial \mathbf{H}}{\partial t} = -\frac{1}{\mu_0}\nabla \times \mathbf{E} \,, \tag{4.4}$$

$$\frac{\partial \mathbf{J}}{\partial t} = \epsilon_0 \omega_{pe}^2 \mathbf{E} - \omega_{ce}\mathbf{J} \times \mathbf{e}_z \,, \tag{4.5}$$

where the plasma properties enter the computations through the current. Equation (4.5) describes the evolution of a current in a cold and collisionless plasma as discussed in chapter 2.2. Yee proposed the algorithm to compute the electric and magnetic fields in vacuum. IPF-FD3D is an extension of this method to plasmas, which in addition computes the current density in the plasma. Therefore, the problem is gridded into voxels which center the **E** and **H** components so that every **E** component is surrounded by four cycling **H** components and vice versa. This type of a voxel is called the Yee cell and is depicted in figure 4.3. The lattice is equally spaced $\Delta x = \Delta y = \Delta z = \Delta$, but the current density and the fields are computed on different positions in the Yee cell. Thus, after the computation of the fields an interpolation is performed in order to compute the current and the fields in the center of the Yee cells. The location of a certain grid cell center is

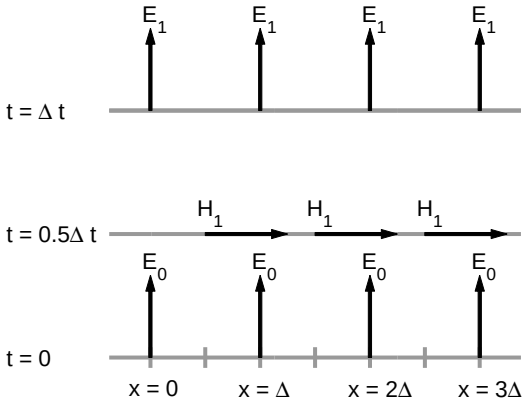

Figure 4.4: The leapfrog scheme for the computation of the fields in the FDTD method.

specified by

$$(i, j, k) = (i, j, k)\Delta \ , \tag{4.6}$$

where i, j and k are integers. The derivatives are approximated by central-differences

$$\frac{\partial u}{\partial x}(i, j, k, n\Delta t) = \frac{u^n_{i+1/2,j,k} - u^n_{i-1/2,j,k}}{\Delta} \ , \tag{4.7}$$

which is accurate up to second order in the Taylor expansion of $\partial u/\partial x$. The location of the **E**- and **H**-fields in the Yee cell together with the central difference operations on these components implicitly enforce the validity of the Maxwell divergence equations (2.1c) and (2.1d).

In the computation of the fields, **E** and **H** components are not only computed at different positions in space, but also in time. The algorithm starts from certain initial conditions for the current $\mathbf{J}_0$ for $t = 0$ from which the initial electric field $\mathbf{E}_0$ is computed employing (4.3). From the initial conditions for the electric field the **H**-fields called $\mathbf{H}_1$ are calculated at time $t = \Delta t/2$ using (4.4). Those results are used to calculate the fields $\mathbf{J}_1$ from (4.5) and $\mathbf{E}_2$ from (4.3) at time $t = \Delta t$. Thus, the first time step includes the calculation of the electric and magnetic fields separate from each other and central in time, as illustrated in figure 4.4. This is repeated until the desired final time point is reached. Due to the double calculation in one time step this scheme is called leapfrog time-stepping.

So far the computation of the fields and currents in a lattice have been discussed. Since such lattices are always of limited size in space, boundary conditions have to be imposed on the lattice borders. Electromagnetic fields propagating inside the computational domain impinge on the boundary at arbitrary angles θ. In most problems it is desirable to have boundary conditions which absorb the incident waves regardless of their incidence angle θ. A convenient method to achieve this is the use of a so called uniaxial perfectly matched layer absorbing boundary conditions (UPML-ABC) [82]. The finite lattice is surrounded by a thin boundary lattice, the material properties of this boundary are fine tuned to achieve adequate

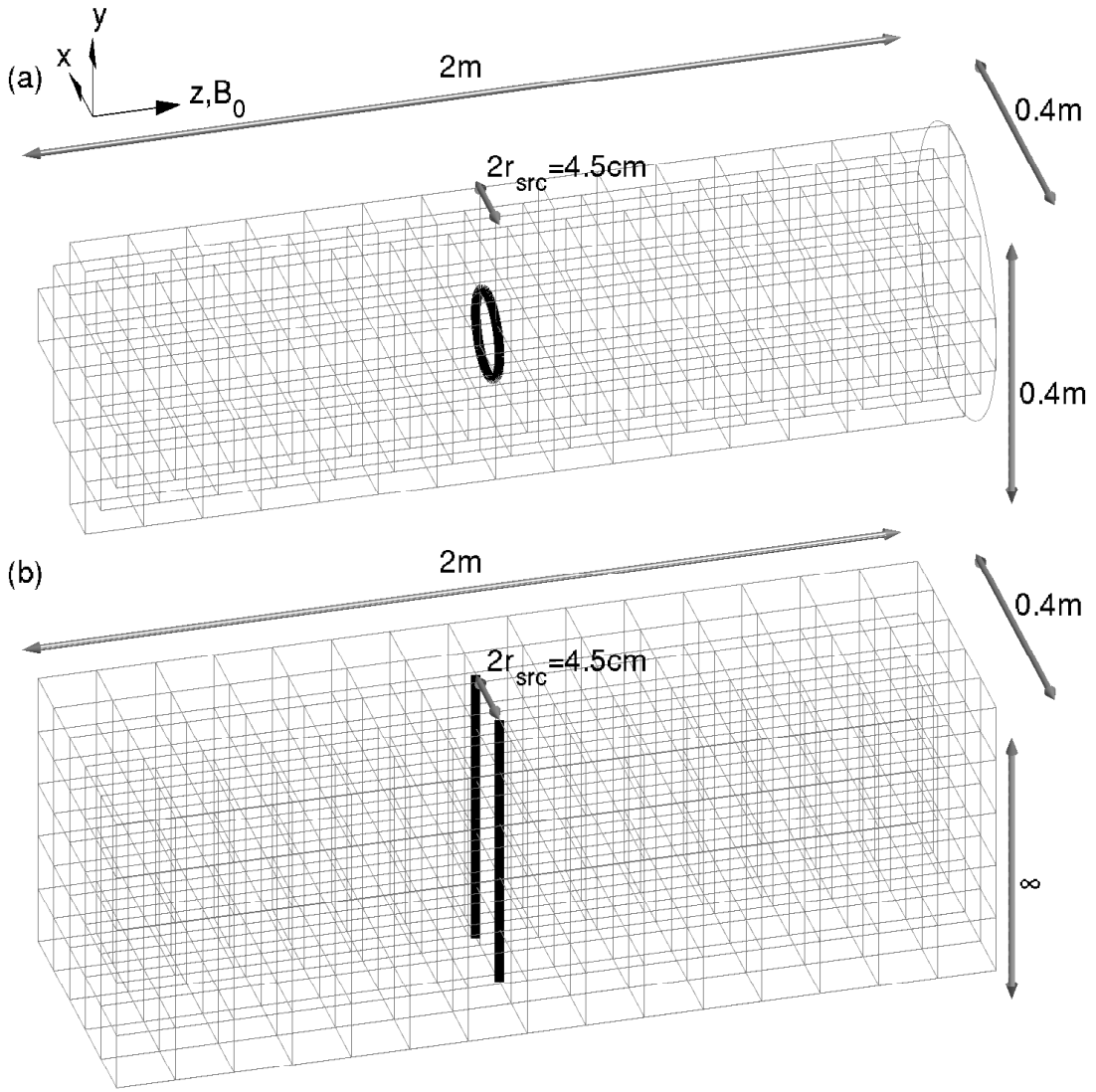

Figure 4.5: Geometry of the simulation grid and the wave exciters. The ambient magnetic field parallels the axial direction. The size of the grid cells is disproportionated in comparison with the size of the grid cells used in computations. Thick black lines illustrate the wave exciters.

absorption and negligible reflection of the incident waves independent of the angle under which the wave impinges onto the boundary layer. Uniaxial materials provide this property at a lower computational effort than alternative methods [83]. The simulations presented in the following have been performed in 2D and 3D. Figure 4.5 (a) illustrates the 3D simulation grid and the wave source. The axial length of the grid is 2 m and parallels the direction of the ambient magnetic field. In the perpendicular direction the simulation volume has a diameter of 0.4 m. The wave source is a current ring with $r_{src} = 0.0225$ m, it has a Gaussian current density distribution with a full width at half mean of $\sigma = 0.007$ m. As shown in figure 4.5 (a) it is located in a plane perpendicular to the ambient magnetic

field centered in the axial direction and the ring is coaxial to the simulation grid. The grid cells depicted are much larger than the ones used in the simulations. Therefore, the boundary in the radial direction has been illustrated as a circle at the right end of the simulation volume. The plasma density profile is of Gaussian shape

$$n = n_0 \exp\left(-\left[\frac{r}{\sigma}\right]^2\right) \tag{4.8}$$

and close to the boundary of the simulation volume the plasma density is ramped down to zero within a distance of about a few grid cells before the UPML follows up. Thus, the plasma possesses two gradients. One due to the plasma profile and a second one which is introduced to model the plasma decrease in the plasma sheath. In IPF-FD3D the source of the fields is given by a current density which generates the fields in the surrounding plasma by inductive coupling. Those fields are the initial fields in the leapfrog scheme. Therefore, the current density given as the external generator of the initial fields is the source of the wave. In order to achieve continuous wave propagation the source current flow is initialized at $t = 0$ at a frequency kept constant throughout the entire simulation.
A weakness of the Yee algorithm is its large computational effort, especially in 3D simulations. If the simulation is restricted to a radial axial plane aligned with one of the perpendicular directions through the simulation volume the computational effort is much smaller. However, since the Yee-algorithm is formulated on a Cartesian grid a simulation performed in this way corresponds to a 3D geometry as depicted in figure 4.5 (b). The simulation grid has a slab geometry which is infinitely extended in one of the perpendicular directions. In this direction the plasma density is constant, while it has Gaussian shape in the perpendicular direction. Instead of a current ring two infinitely extended parallel currents are simulated. Since the plasma geometry and the source current geometry changes a benchmark test needs to be performed whether 2D simulations can be used instead of 3D ones.
The simulations of wave propagation are performed for the parameters found in

	f (MHz)	ω/ω_{ce}	γ	$n_0(10^{18}\mathrm{m}^{-3})$	B_0(mT)	σ(cm)
I	200	0.45	0.037	1.732	15.8	7.24
II	200	0.2	0.111	1	35.5	7.77
III	100	0.11	0.054	3.366	31.6	6.67

Table 4.1: Parameter sets for which simulations are performed.

table 4.1. 3D simulations are performed for each parameter set with a spatial resolution $\Delta = 1.8$ mm and a temporal resolution of $\Delta t = 2.965$ ps. A 2D simulation is performed for the parameter set I with a spatial resolution $\Delta = 1$ mm and the same temporal resolution as in the 3D simulations. Since the memory required to store the computed fields at all time instances is rather large only a subset of the computed data at equally spaced time instances is stored for subsequent

processing. In graphical representations the simulation data are interpolated.

4.2.1 Ducting and Leakage of Loop Antenna Excited Waves

The preferred propagation direction is illustrated by depicting the time evolution of energy density isosurfaces for $U = 5$ nJ/m^3 and the energy transport by Poynting vector field lines. A 3D simulation with the plasma parameters described in table 4.1 II is chosen. Wave excitation is performed at $z = 0$ and the ambient magnetic field is parallel to the z-direction. The radial limit of the simulation volume is indicated by a gray circle at $z = 0$. Figure 4.6(a)-4.6(d) shows four different time instances. In figure 4.6 (a) the simulation has progressed about five periods, the energy density is smaller than 5 nJ/m^3 over the entire simulation volume. Therefore, no isosurface is depicted. The Poynting field lines are relatively diffuse and have not reached the boundaries of the simulation volume at the depicted time instance. Figure 4.6 (b) shows a time instance of the simulation in which the energy density has increased above the threshold value close to the antenna. The Poynting field lines have reached the radial and axial limits of the simulation volume. However, most of the lines are confined within the plasma radius defined by $r = \sigma$. In figure 4.6 (c) the region in which the energy density is above threshold extends further away from the antenna, but is limited by the plasma radius in its lateral extend. The same holds for the Poynting field lines only a small number of lines is penetrating the region outside the plasma radius. Those lines continue until they reach the limits of the simulation volume, where the energy is absorbed, reflected or trapped. At the axial limit most of the energy becomes trapped close to the limit of the simulation volume. At the time instance in figure 4.6 (d) this trend is sustained. The energy density isosurface extends along the entire axial length within the plasma radius, but is small outside except at the radial limits, at which energy has accumulated. An asymmetry with respect to the plasma center is found in this region which is due to the time dependency of the field. The Poynting field lines are almost completely confined inside the plasma radius. At larger times, which are not depicted, the portion of the wave reflected at the outer limits contributes dominantly to the energy inside the plasma radius. Thus, at those times the influence of the boundaries becomes important and the simulation can no longer be used. The analysis of the energy flow time dependency reveals a ducting of the wave inside the plasma radius. Most of the wave energy is found in a cylindrical region around the plasma center. Reflections at the simulation volume limits are negligible up to a certain time instance. From a direct comparison of the fields in this time window a spatiotemporal window is found in which the wave field is in continuous wave mode. Points in the simulation volume which have experienced ten periods of the wave are found to be in continuous wave mode. This spatiotemporal window is used to perform predictions on whistler wave propagation.

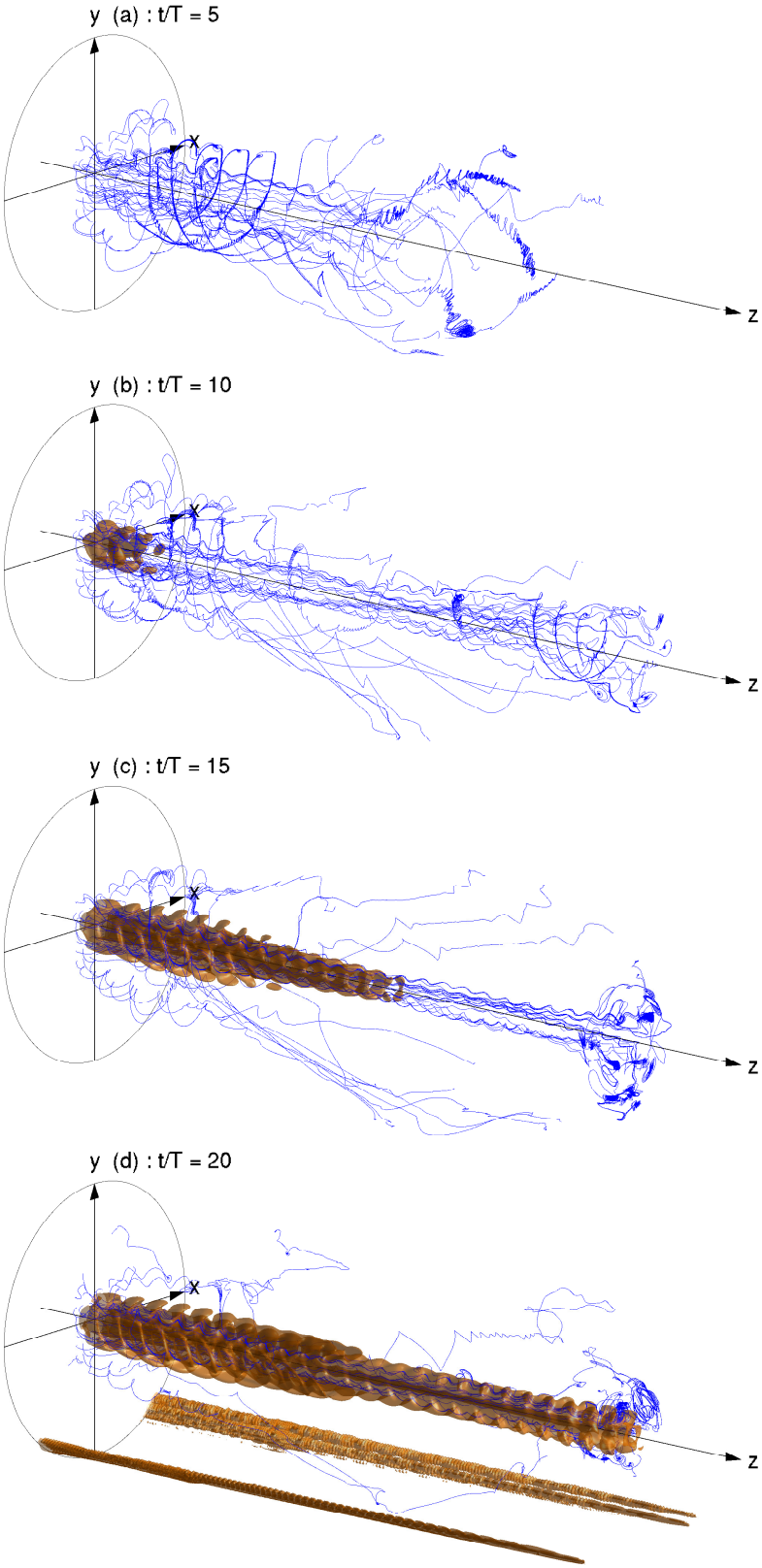

Figure 4.6: Spatial evolution of the energy density and the energy transport at four time instances for parameters from set II.

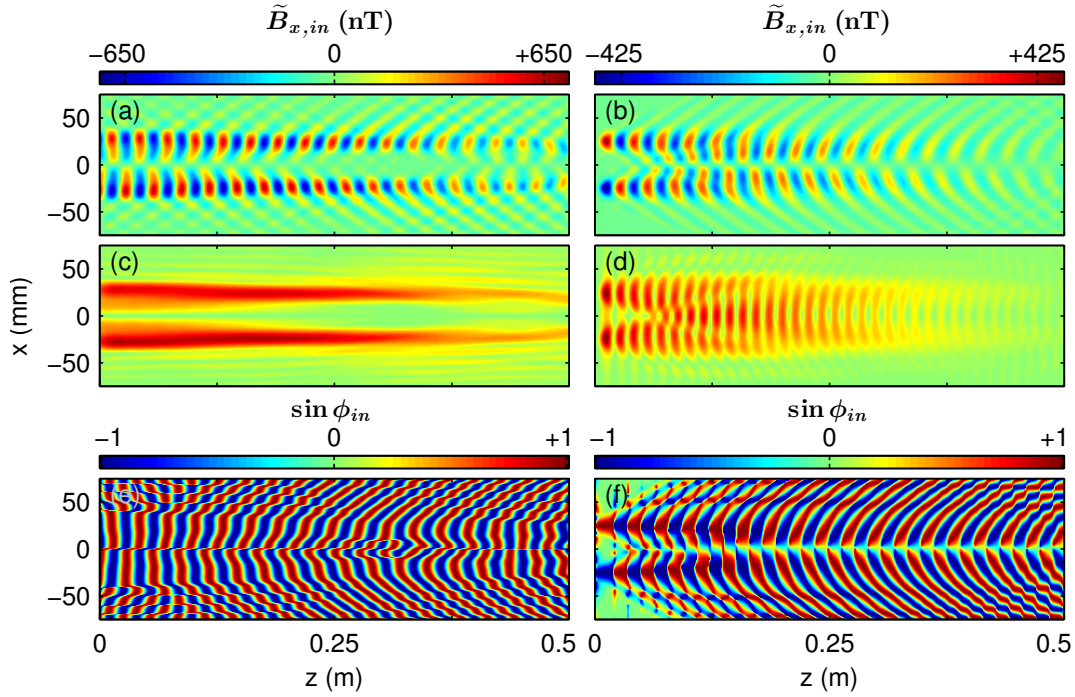

Figure 4.7: IPF-FD3D simulation of wave propagation for the plasma parameter set I at t/T=25. The field is simulated in a 2D (left column) and a 3D (right column) plasma geometry. The magnetic field component $\widetilde{B}_{x,in}$ is depicted in xz-planes.

4.2.2 Comparison of 2D and 3D Simulations

As stated above, simulations in two and three dimensions have been performed for the parameter set I. Figure 4.7 shows a comparison of those simulations for a time instance at which the wave field is in continuous wave mode and reflections are unimportant. Figure 4.7 is subdivided in two columns the left column shows the result of the 2D simulation and the right of the 3D simulation. The component of the wave magnetic field in the x-direction $\widetilde{B}_{x,in} = B_{x,in} \sin \phi_{in}$ in a xz-plane is depicted in figure 4.7 (a) and 4.7 (b). At least a qualitative agreement of both fields close to the wave exciter is found, while the fields differ in their axial evolution. The instantaneous amplitude $B_{x,in}$ is depicted in figure 4.7 (c) and 4.7 (d). In both cases the amplitude pattern close to the source is given by two maxima which occur along the radius of the wave exciter. The maxima extend from the wave exciter into the plasma almost parallel to the ambient magnetic field. In both cases the coils tend to focus to the center of the plasma. In comparison the focusing in the 3D case is stronger than in the 2D one. Wave energy is focused to the plasma center in the 3D simulation at distances of about $z = 0.1$ m and is redistributed at larger distances leading to a decrease of wave amplitude in the plasma center for $z > 0.1$ m. The coils in the 2D simulation extend further into the plasma a focusing to the plasma center is not observed. Furthermore, the

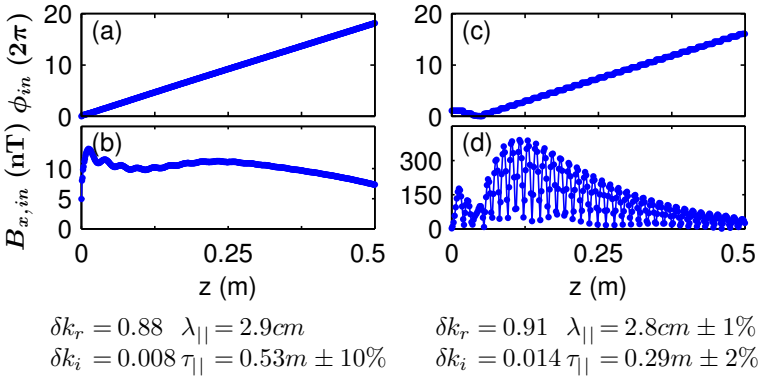

Figure 4.8: Phase (first row) and amplitude (second row) evolution along the plasma center for a 2D (left column) and a 3D (right column) simulation taken from the data presented in figure 4.7. Wave and damping lengths extracted from the axial evolution are indicated below the corresponding figures.

amplitude pattern in the 3D simulation shows vertical streaks which occur periodically in which the magnetic field amplitude is zero, those are not found in the 2D simulation.
The fields instantaneous phase factor $\sin \phi_{in}$ is shown in figure 4.7 (e) and 4.7 (f), both wave fields show a radial anti-symmetry. At radial positions off the symmetry axis, but within the bulk plasma the wave propagation angles are small compared to the ones in the region of the radial density gradient. The 2D simulation shows a region of parallel wave propagation close to the wave exciter which is not present in the 3D simulation.
The phase evolution along the symmetry axis of the plasma for the 2D simulation is depicted in figure 4.8 (a) and the amplitude evolution in 4.8 (b). Figure 4.8 (c) and 4.8 (d) show the same quantities for the three dimensional simulation. A monotonous increase in the phase is found in the 2D simulation, while the 3D simulation shows a small region close to the antenna in which the phase is decreasing instead, for $z > 0.05$ m an increase in the phase is found. The parallel wave length along the symmetry axis is extracted from the region in which the phase increases. An almost equal result is found for both cases indicated below the corresponding figures, which is in excellent agreement with the prediction of the plane wave dispersion relation ($\delta k_r = 0.92,\ \lambda_{||} = 2.8$ cm). A result also found in experiments using a loop antenna and a plasma with similar parameters [84, 85]. The amplitude evolution along the symmetry axis does not show a similar behavior for both simulations. An obvious difference are the short scale fluctuations in the 3D case which are the 1D equivalent to the line like pattern found in the spatial amplitude evolution depicted in figure 4.7 (d). If the envelope of figure 4.8 (d) is compared to figure 4.8 (b) still both cases exhibit a long scale oscillation in the amplitude superimposed on a decay. Since the plasma in the simulation is collisionless the decay is due to geometric damping. The geometric damping is given by the redistribution of wave energy in and the leakage of wave energy

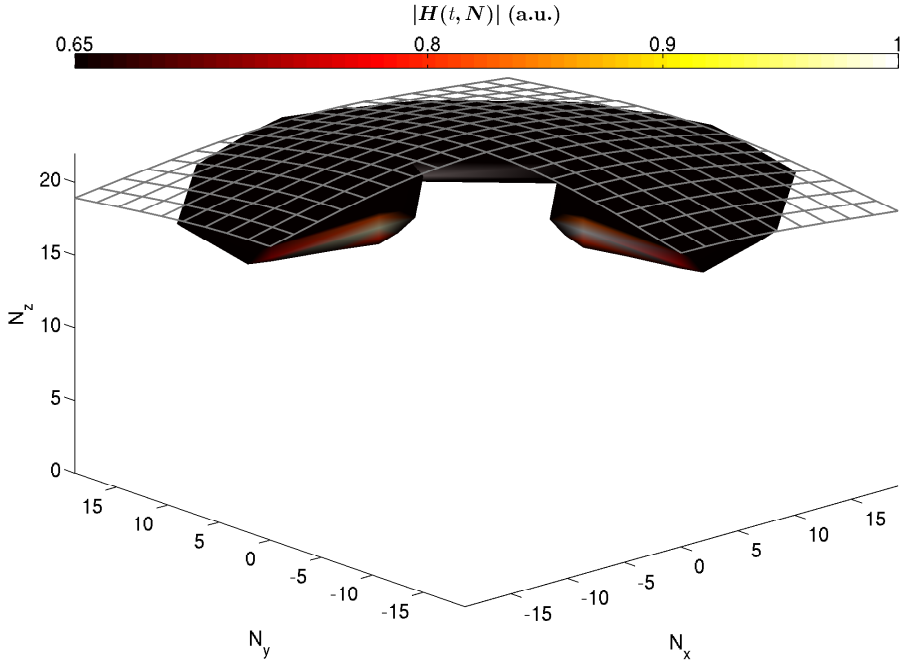

Figure 4.9: Isosurface in the Fourier transform of a simulation with parameters of set II at t/T = 15 and the corresponding plane wave index of refraction surface depicted as a grid in the index of refraction space. A quadrant has been removed in order to show the amplitude distribution inside the isosurface.

from the plasma. The damping length along the plasma center in the 2D case is approximately twice the damping length in the 3D simulation, as indicated below the corresponding figures, where the damping length is approximated by fitting an exponential decay on the data. The difference is mainly due to the effective focusing of wave energy in the plasma center observed in the 3D simulation at $z = 0.1$ m, which causes a strong increase of the wave amplitude at distances $z < 0.1$ m and a strong decrease at larger distances $z > 0.1$ m. Correspondingly the absolute value of the amplitude along the plasma center in the 3D case is much larger than in the 2D case.
Comparable 2D simulations have been performed by Streltsov *et al.* [51] using a wave source extended over the width of the density crest. A phase pattern comparable to the one presented in figure 4.7 (e) is found, but the amplitude pattern differs. Hence, the particular source plays an important role for the wave propagation pattern which needs to be included in the simulation.
In conclusion the influence of the inhomogeneity and the specific wave excitation causes a modification of the waves amplitude pattern and the parallel damping length. The parallel wave length shows a negligible dependency on the radial position in the region depicted in figure 4.7. The differences between both simulations are not negligible, especially the short scale fluctuations in the amplitude, the focusing and geometric damping differ essentially. Therefore, 3D simulations will be used in the following for detailed comparisons with experimental results.

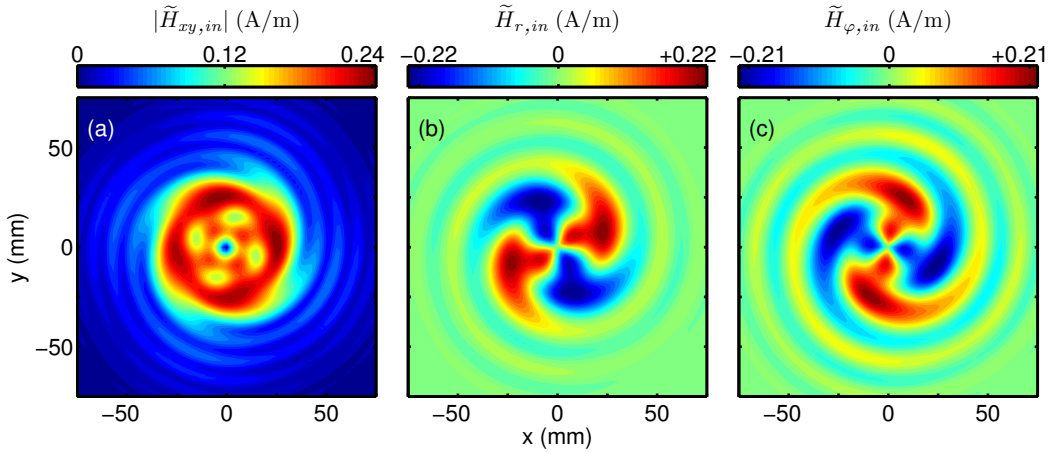

Figure 4.10: Magnetic field in an azimuthal plane at distance $\Delta z = 0.11$ m from the exciter for parameters from set I at t/T = 25. Depicted is the absolute value of the perpendicular field (a), the field in radial (b) and azimuthal direction (c).

4.2.3 Mode of Propagation

In order to compare the agreement of the entire wave field inside the plasma radius with the plane wave dispersion relation, the magnetic field is transformed to Fourier space and an isosurface of constant absolute value of the magnetic field is depicted $|\mathbf{H}(t, \mathbf{N})| = const.$. The agreement of the spectrum with the dispersion relation is tested by depicting an index of refraction surface for the corresponding plasma parameters as a grid, shown in figure 4.9. A quadrant of the Fourier space has been removed in order to visualize the amplitude distribution inside the isosurface and the relative position of the amplitude maximum and the index of refraction surface. A systematic off-set between the maximum of the Fourier transform and the dispersion surface is found. The index of refraction predicted by the simulation has a smaller value than the one predicted by the plane wave dispersion relation, where the offset is attributed to an influence of the plasma inhomogeneity [31, 33]. The toroidal structure of the isosurface, indicating only a small parallel propagating portion of the wave, has also been reported in experiments having a homogeneous plasma and a loop antenna [40]. This is a property of the excitation by loop antenna, which mainly launch oblique propagating waves. The volume of the torus indicates the excitation of a broad band of whistlers. Hence, instead of launching a plane wave a complex wave packet like structure is excited. This effect is not only due to the inhomogeneity of the plasma, but also to the source of the wave [40, 86]. Thus, the simulations with IPF-FD3D reproduces features expected from cold plasma dispersion theory, supplemental experiments in homogeneous plasmas and alternative theoretical approaches. An open issue is the cause of the short scale fluctuations found in the amplitude of the 3D simulations. Those will be addressed in the following. Figure 4.10 depicts the magnetic field in an azimuthal plane. In figure 4.10 (a) the absolute value of the

magnetic field in an azimuthal plane close to the wave source is shown. A pattern indicating large amplitudes inside the plasma radius and small amplitudes outside is found. The radial component of the magnetic field is shown in figure 4.10 (b), while figure 4.10 (c) shows the magnetic field in azimuthal direction. Plane wave dispersion theory predicts an azimuthal invariance of the wave field, as discussed in chapter 2.1. Thus, the azimuthal field shows a clear evidence for a wave mode differing from plane waves. Modes in a cylindrical plasma can be characterized by the number of extrema found in the azimuthal direction. The field of such a mode is proportional to $e^{-im\varphi}$ in the azimuthal direction, where φ is the azimuthal angle and m the number of wave lengths in the azimuthal direction called mode number. As figure 4.10 (b) shows four extrema are found and therefore the mode observed in the simulation is an $m = 2$ mode. Similar whistler modes are investigated in connection with helicon discharges [22, 87]. Although, those investigations are performed at smaller frequencies and correspondingly larger parallel wave lengths.
An open question is the selection rule after which the particular mode number is chosen. Investigations of loop antenna excited whistler waves in a laboratory plasma in which the boundaries are unimportant reveal excitation of an $m = 0$ mode [40]. A simple model based on the dominance of Hall currents over polarization currents explains the excited mode structure at least qualitatively as a consequence of the excitation by a loop antenna [36]. The occurrence of higher azimuthal modes observed in the simulation is due to the boundary conditions given by the inhomogeneity of the plasma. In a cylindrical plasma an infinite number of eigenmodes is possible [31]. Under the plasma parameters chosen in the simulations the $m = 2$ mode with one maximum in the radial direction fits best to the current pattern induced by the loop antenna. Thus, the mode structure is a consequence of the plasma parameters, the excitation by a loop antenna and the ratio of the plasma and antenna diameter. In order to elucidate the spatial structure of the excited mode isosurfaces of the current density, the wave fields and the fluctuating space charge are depicted in figures 4.11 (a) - 4.11 (d). The spatial structure of the simulation data is a result of the plasma inhomogeneity and the wave exciter geometry. Inside the plasma radius a mode structure is found which consists of two regions with opposite polarity having a helical shape. The helices form a double helix. In the region of the radial density gradient the wave velocity increases and the slope of the helical isosurfaces is modified. In the isosurface representation the radial density gradient causes a shape which can be decomposed into a helical and a conical pattern. This effect is especially pronounced in the electric field and the space charge, see figure 4.11 (c) - 4.11 (d). The magnitude of the fluctuating space charge is found to be at least six orders smaller than the magnitude of the plasma particle density, independent of the radial position. Thus, quasi neutrality is preserved. The short and long scale fluctuations in the amplitude and the phase jump in the center of the plasma depicted in figure 4.7 are a consequence of the waves mode structure. According to plane wave theory the electric and magnetic field perpendicular to the ambient magnetic field are also perpendicular to each other. The angle between the perpendicular electric

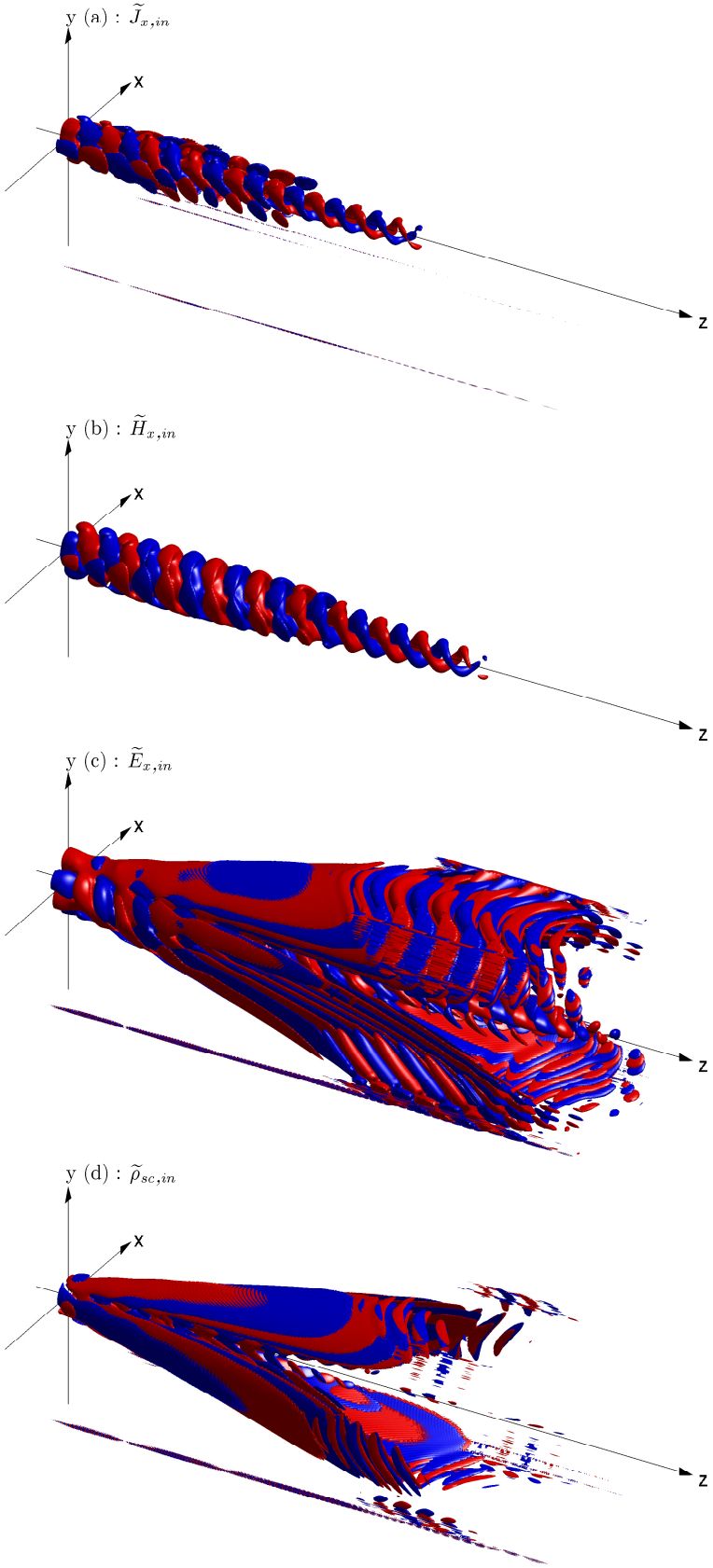

Figure 4.11: Mode structure of the x-component of (a) the current density, (b) the magnetic field, (c) the electric field and (d) the fluctuating space charge density at t/T = 15 for a simulation with parameters from set II.

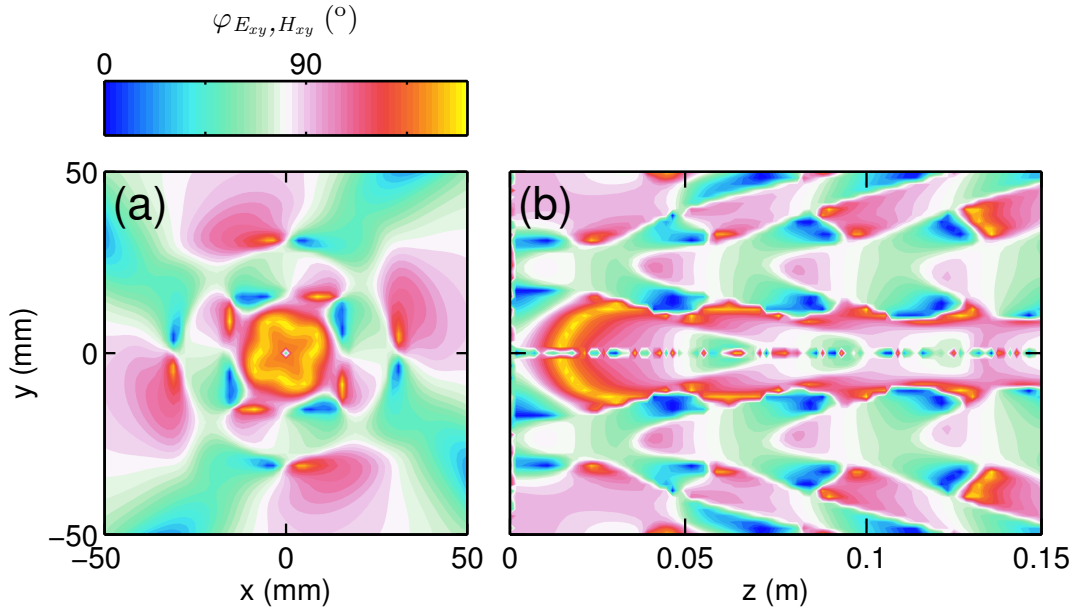

Figure 4.12: Angle between the magnetic and the electric field in an azimuthal plane (a) at a distance $\Delta z = 1.8$ cm to the exciter and in a yz-plane (b) for parameter set II at t/T=15.

and magnetic field $\varphi_{E_{xy},H_{xy}}$ is depicted in figure 4.12 (a) in an azimuthal plane at $\Delta z = 1.8$ cm distance from the wave exciter and in a yz-plane (b). A complex pattern is found instead of a constant 90° angle.

4.2.4 Wave Field Topology

In order to illustrate the vector field topology predicted by the simulation the absolute value of the wave amplitude and the vector field, where the arrows of the field are normalized to a length of unity, are depicted in an azimuthal plane. Figure 4.13 shows the topology of the current density (a), the magnetic field (b) and the electric field (c) in a distance of $\Delta z = 1.8$ cm from the exciter antenna. The field topology of the current density and the magnetic field are given by eddies, where the magnetic field topology is similar to the current density field topology at least in the regions in which the current is large. Since a loop antenna couples inductively to the plasma the eddy dominated topology is expected. However, the eddies are another feature demonstrating the necessity of simulations for the description of the wave field, since models like dispersion theory can not reproduce such effects particular to the wave exciter. In the electric field topology eddies are not dominant instead sources and sinks are clearly visible, which indicates a dominant contribution of the fluctuating space charge to the electric field.
Figure 4.14 depicts the axial evolution of the fields shown in figure 4.13, where figure 4.14 (a) depicts the current density, (b) the magnetic field and (c) the

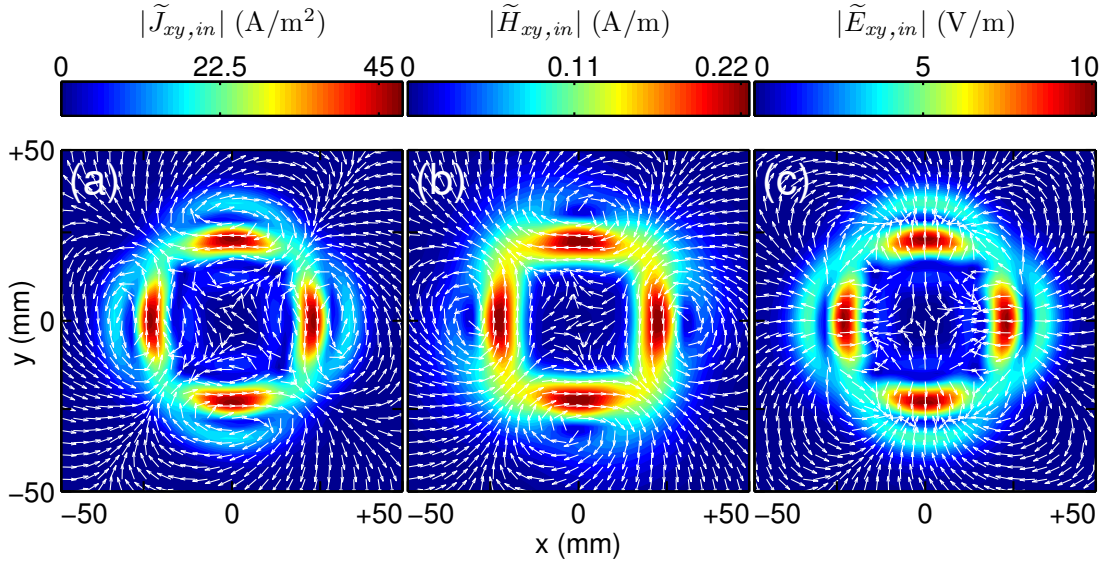

Figure 4.13: (a) Current density, (b) magnetic field and (c) electric field shown in an azimuthal plane at an axial distance of $\Delta z = 1.8$ cm to the exciter. The simulation is performed for parameter set II and is depicted for t/T = 15.

electric field. As in the azimuthal plane the current density and the magnetic field are dominated by eddies and the electric field by sources and sinks. The fields in the radial axial plane exhibit a non-trivial axial evolution. Together with the azimuthal representation the radial axial cuts show a complex three dimensional structure of the predicted fields.
Although, spectral analysis shows that most of the wave energy is close to a plane wave dispersion surface and the wave length along the symmetry axis of the plasma agrees with the prediction of plane wave theory a complex wave field topology is found. Also symmetries like the azimuthal symmetry predicted by the plane wave dispersion theory are absent, instead a $m = 2$ mode is predicted.

4.2.5 Sources of the Electric and Rotation of the Magnetic Field

In figure 4.15 (a) the fluctuating space charge $\widetilde{\rho}_{sc,in}$ in an azimuthal plane at a distance of $\Delta z = 1.8$ cm to the wave exciter is shown. Several maxima of the space charge are found in radial and azimuthal direction, which are due to the mode structure of the excited wave. Figure 4.15 (b) depicts the absolute value of the electric fields rotation $|\nabla \times \widetilde{\mathbf{E}}_{in}|$ in the same azimuthal plane as the space charge. Along the loop antenna's circumference a considerable rotation is found, while it is negligible elsewhere. The absolute value of the rotation shows azimuthal symmetry.
The radial-axial distribution of the space charge is shown in figure 4.16 (a) exhibiting a non-trivial axial evolution. High values of the space charge are found along

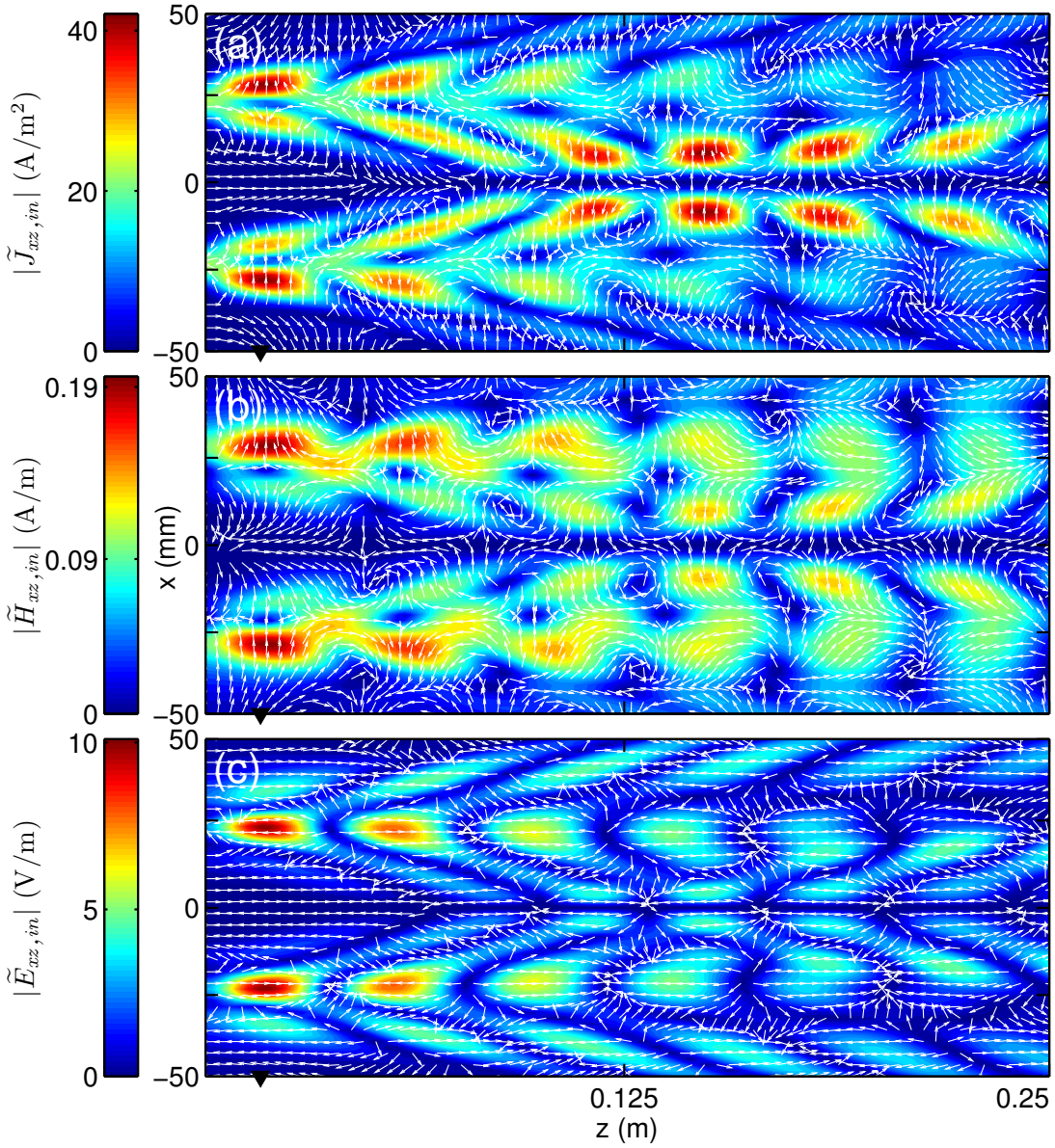

Figure 4.14: (a) Current density , (b) magnetic field and (c) electric field shown in a xz-plane. The simulation is performed for parameters of set II and is depicted for t/T = 15. The axial position of the azimuthal cuts depicted in figure 4.13 is indicated by triangles.

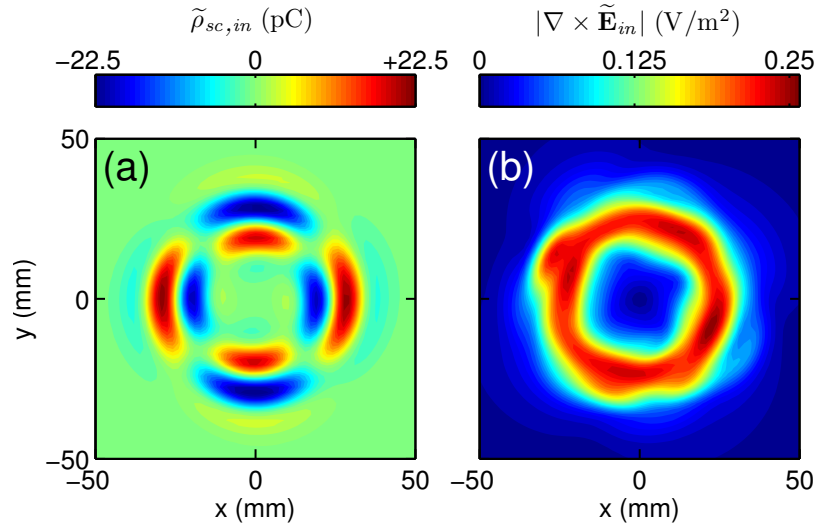

Figure 4.15: (a) Fluctuating space charge and (b) the absolute value of the electric fields rotation for a simulation with parameters from set II at $t/T = 15$ in an azimuthal plane at $z = 1.8$ cm.

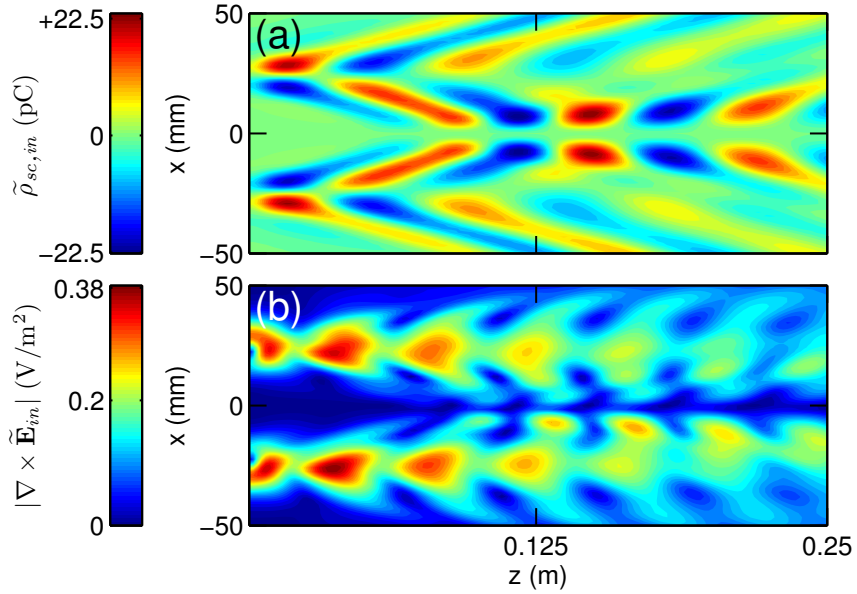

Figure 4.16: (a) Fluctuating space charge and (b) the absolute value of the electric fields rotation for a simulation with parameters from set II at $t/T = 15$ in a xz-plane.

the loop antenna circumference close to the antenna and close to the plasma center at a certain distance $z > 0.125$ m to the antenna. Figure 4.16 (b) shows the axial evolution of the rotation of the electric field. High values of the rotation are found close to the loop antenna along its circumference. The rotation becomes smaller with increasing distance from the antenna. The electric field of the wave receives contributions from both, the electrostatic field due to the fluctuating space charge

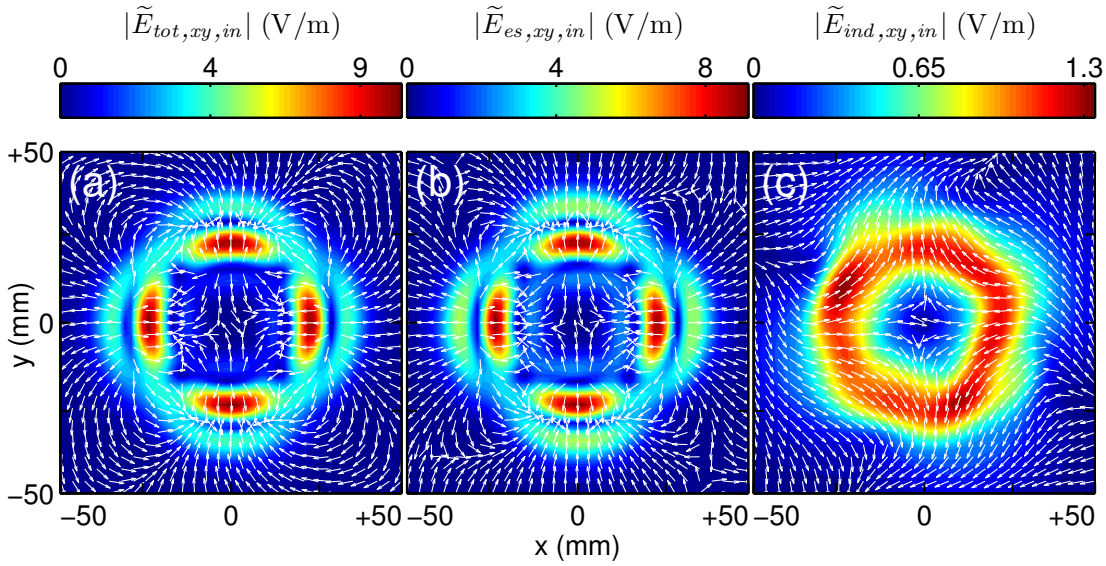

Figure 4.17: (a) total electric field (b) electrostatic electric field (c) inductive electric field for a simulation with parameters from set II at $t/T = 15$ in an azimuthal plane at $z = 1.8$ cm.

and the inductive electric field due to $|\nabla \times \widetilde{\mathbf{E}}_{in}|$. In order to clarify the relative contribution a Helmholtz decomposition of the electric field is performed. Figure 4.17 shows azimuthal cuts through (a) the total electric field, (b) the space charge field and (c) the inductive field at an axial distance of $\Delta z = 1.8$ cm to the exciter. Depicted color-coded are the absolute values of the fields and the field vectors normalized to unity. As expected, the fluctuating space charge is found to have high values in regions in which the electrostatic electric field is small. The inductive electric field has high values in regions in which the full electric field's rotation has high values. Consequently, the azimuthal symmetries are the same as for the divergence and the rotation of the total electric field. Figure 4.17 indicates a dominant contribution of the electrostatic field to the total electric field. The axial evolution of the fields depicted in figure 4.18, where (a) the total electric field, (b) the electrostatic electric field and (c) the inductive electric field is depicted in a radial-axial plane. Again the absolute value of the fields are depicted color-coded while the field vectors are normalized to unity. The dominance of the electrostatic electric field over the inductive electric field is confirmed. Hence, the source for the total electric field as predicted by the simulations is the space charge. The inductive electric field is found to have its largest values along the circumference of the antenna along its entire axial evolution, it is non-zero but small against the electro static field.

The electric field receives contributions from the space charge and induction by the magnetic field. Since no magnetic charges exist the magnetic field receives only inductive contributions, but also this field receives two different contributions. The rotation of the magnetic field includes contributions from the electron current and the displacement current, see (2.1a). Thus, the magnetic field can be

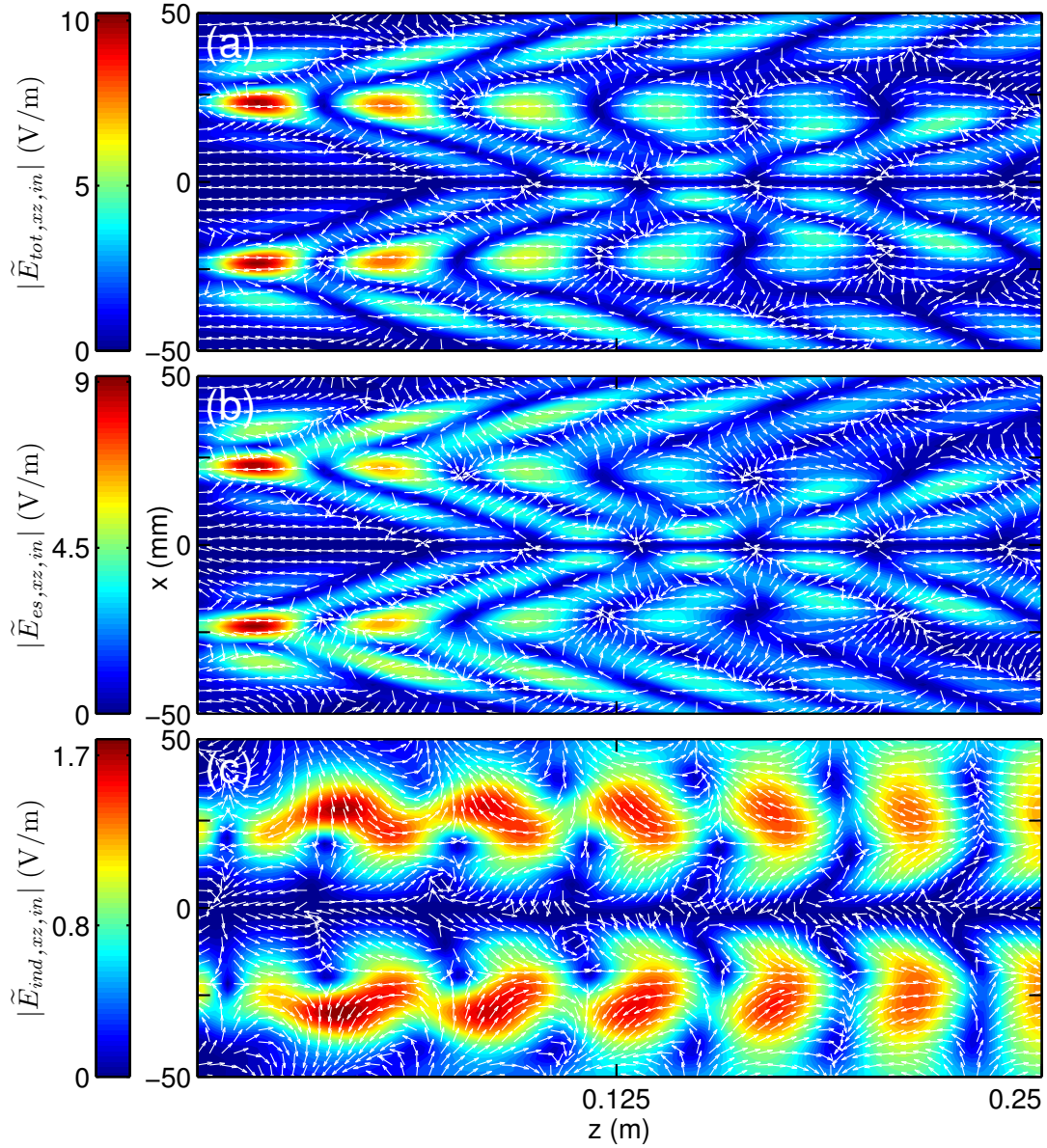

Figure 4.18: (a) Total electric field (b) electrostatic electric field (c) inductive electric field for a simulation with parameters from set II at $t/T = 15$ in a xz-plane.

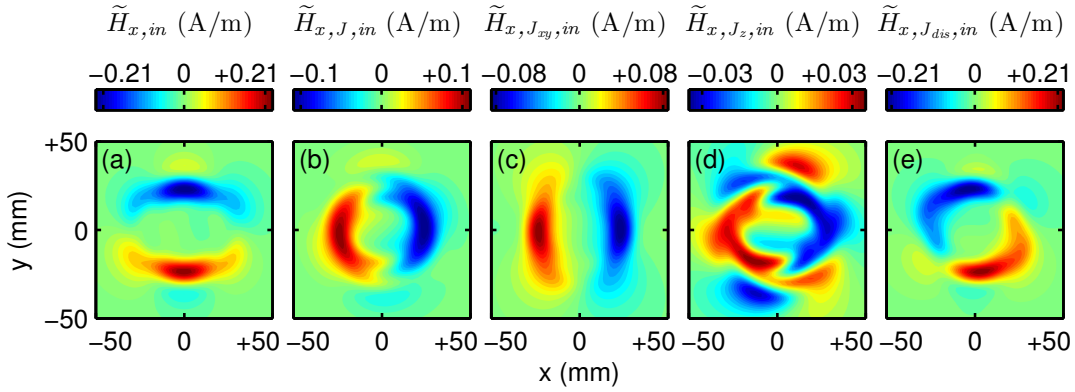

Figure 4.19: (a) Total magnetic field (b) magnetic field due to the total electron current (c) magnetic field due to the perpendicular electron current (d) magnetic field due to the parallel electron current (e) magnetic field due to the total displacement current for t/T = 15 and parameters from set II in an azimuthal plane at $z = 1.8$ cm in the x-direction.

subdivided in a field due to the electron current $\mathbf{J}$ and the displacement current $\mathbf{J}_{dis} = \epsilon_0 \partial \mathbf{E}/\partial t$. In addition the field due to the electron current is decomposed in a field given by the current perpendicular and parallel to the ambient magnetic field. In Fourier space (2.1a) is solved for the magnetic field

$$\mathcal{F}\{\mathbf{B}\} = -\frac{\omega}{k^2}\mathbf{k} \times (\mathcal{F}\{\mathbf{J}\} + \mathcal{F}\{\mathbf{J}_{dis}\})\,. \tag{4.9}$$

In order to compute the field due to a specific current, all other currents are set to zero. Results of the computation in an azimuthal plane are shown in figure 4.19. A contribution from each of the possible currents is found. Though, the contribution of the different fields to the total magnetic field differs. Figure 4.20 shows the axial evolution of the different contributions to the fluctuating magnetic field. The peak value of the magnetic field due to the perpendicular electron current is larger than the one for the parallel currents. Thus, the magnetic field due to the total current is almost identical with the one due to the perpendicular currents. The magnetic field due to the displacement current is larger than the one for the electron current. Thus, the contribution of the electron and displacement current to the total magnetic field has the same magnitude of order.

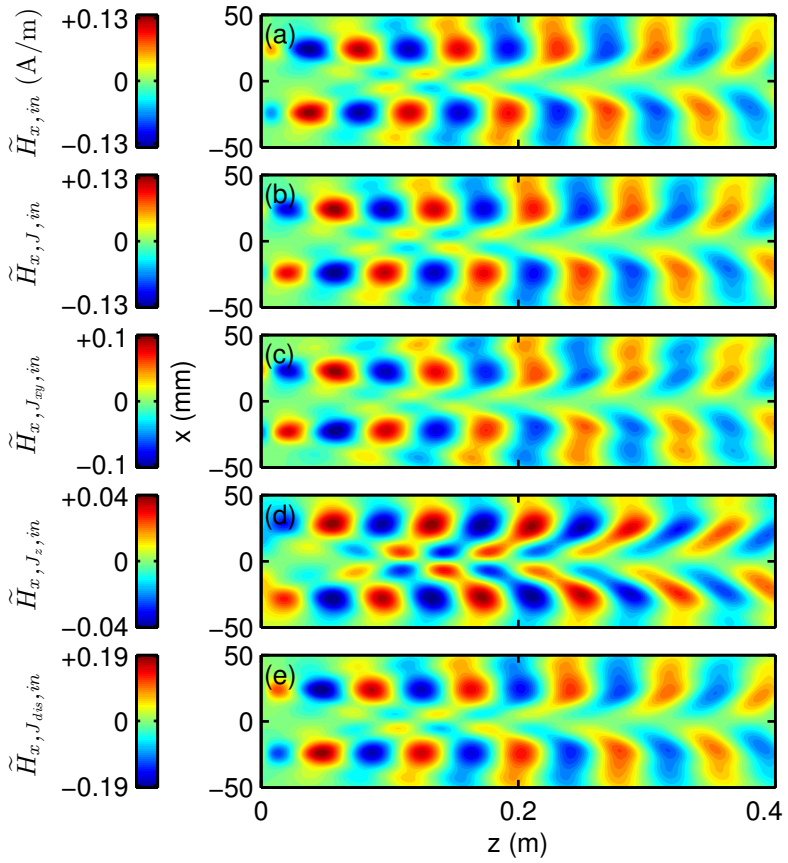

Figure 4.20: (a) Total magnetic field (b) magnetic field due to the total electron current (c) magnetic field due to the perpendicular electron current (d) magnetic field due to the parallel electron current (e) magnetic field due to the total displacement current for t/T = 15 and parameter set II in a xz-plane in the x-direction.

5 Experimental Methods

5.1 Experimental Device

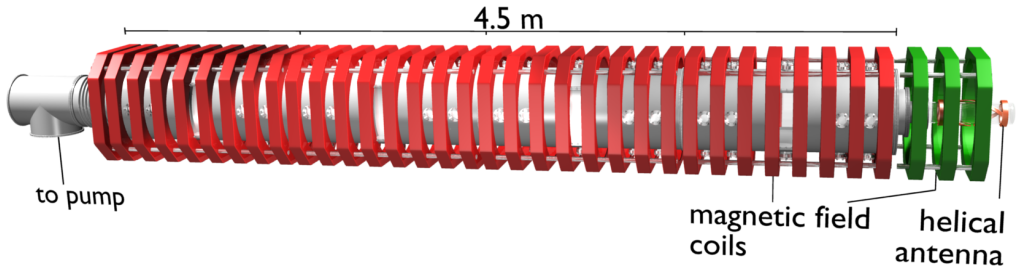

Figure 5.1: Schematic of the linear device VINETA. VINETA is an acronym for: Versatile Instrument for Studies on Nonlinearity, Electromagnetism, Turbulence and Applications.

The experiments are performed in the VINETA [88] device. This device has a cylindrical vacuum vessel consisting of four identical stainless steel modules. Each module has a length of 1.128 m and a diameter of 0.4 m, access is granted via a large number of ports.

On the left a vacuum pump is connected to the device and on the right a Pyrex cylinder with a diameter of 0.1 m is attached. Around the Pyrex cylinder a water cooled helicon antenna is mounted for plasma generation using a rf-signal with a frequency of $f = 13.56$ MHz and 5 kW maximum power. Impedance matching of the amplifier system to the antenna is achieved via a L-matching network consisting of two tunable high-voltage vacuum capacitors, see figure 5.2 (a).

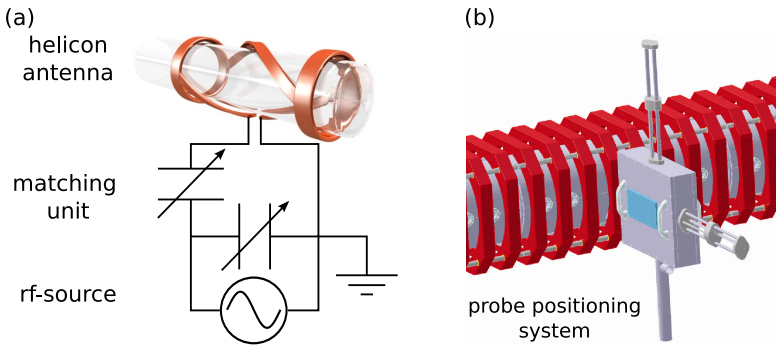

Figure 5.2: (a) Helicon antenna and L-matching network. (b) probe positioning system for probe positioning on a plane perpendicular $\mathbf{B}_0$.

The vacuum vessel is surrounded by 36 water cooled magnetic field coils which produce a uniform $\Delta B_0/B_0 < 1$ % ambient magnetic field $B_0 \leq 100$ mT. The coils of each module and the source field are powered by individually controlled 60 kW dc power supplies.
Three discharge modes are possible: capacitive, inductive and helicon mode [89]. Most experiments are performed in the inductive mode using argon as working gas with typical pressure $p_{Ar} = 0.1$ Pa. Those inductive discharges are collisionless to a good approximation with collision frequencies of $\nu/\omega_{ce} < 10^{-2}$. Typical parameters are compiled in table 5.1.

Positioning of probes is achieved by two probe positioning systems one for mea-

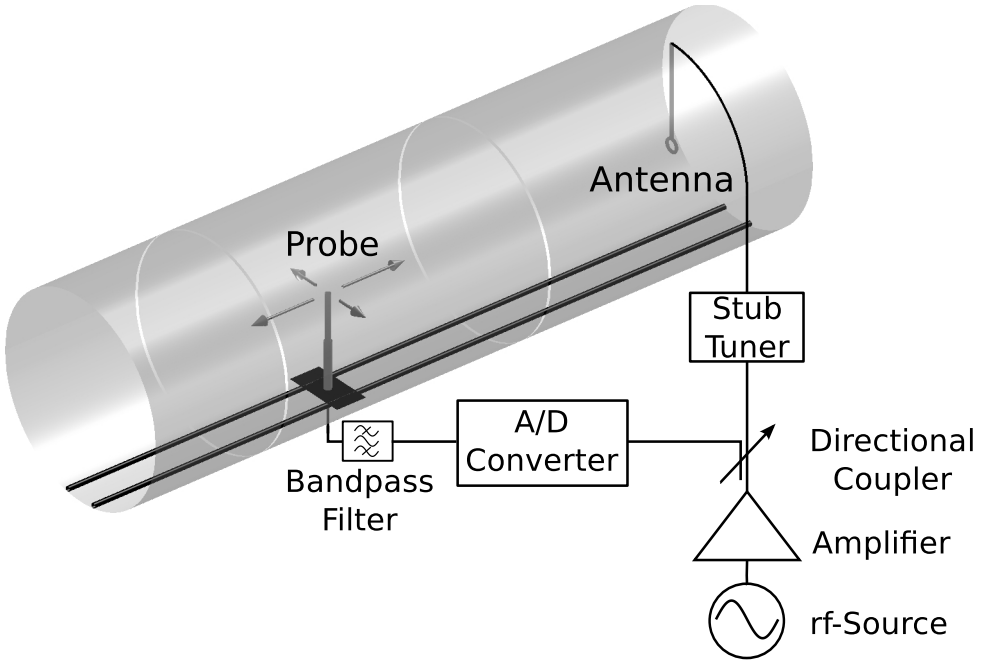

Figure 5.3: View onto the radial-axial probe positioning system mounted inside the vacuum vessel and the schematic of the wave excitation and measurement setup.

surements in an azimuthal plane depicted in figure 5.2 (b) and a second one for measurements along a radial axial plane, shown schematically in figure 5.3. The components found in figure 5.3 are connected via coaxial cables, the bandpass filter removes the rf-frequency of the helicon antenna field from the measured times series.

operation parameter	unit	typical value	range
rf-power	kW	3	$1-5$
rf-frequency	MHz	13.56	—
base pressure	Pa	10^{-4}	—
neutral gas pressure	Pa	0.1	$0.08-0.35$
ambient magnetic field	mT	20	$10-40$
peak electron density	$10^{19}\mathrm{m}^{-3}$	0.1	$0.02-0.5$
peak electron temperature	eV	2.5	$2.1-3$
peak ion temperature	eV	0.2	—
parallel length	m	4.5	—
radial density gradient length	m^{-1}	70	$50-112$
plasma radius	m	0.05	$0.04-0.07$
ionization degree	%	50	—

plasma parameter	unit	typical value	range
dimensionless parameters			
plasma γ		0.05	$0.01-0.2$
electron plasma β		10^{-3}	$10^{-4}-0.024$
collisionality ν		10^{-3}	$10^{-4}-0.01$
electron-ion mass ratio		$1.36\cdot10^{-5}$	—
magnetic perturbation B_x/B_0		10^{-3}	$5\cdot10^{-4}-2\cdot10^{-3}$
lengths			
parallel wave length $\lambda_{\|\|}$	m	0.05	$0.02-0.11$
Debye length	m	10^{-5}	$5\cdot10^{-6}-3\cdot10^{-5}$
collisionless skin depth δ	m	$5.3\cdot10^{-3}$	$2.4\cdot10^{-3}-0.012$
velocities			
electron thermal velocity $v_{th,e}$	m/s	$9.4\cdot10^{5}$	$8.6\cdot10^{5}-10^{6}$
ion thermal velocity $v_{th,i}$	m/s	979	—
frequencies			
electron cyclotron frequency ω_{ce}	rad/s	$4.42\cdot10^{9}$	$2\cdot10^{9}-7\cdot10^{9}$
ion cyclotron frequency ω_{ci}	rad/s	$6\cdot10^{4}$	$2\cdot10^{4}-10^{5}$
electron plasma frequency ω_{pe}	rad/s	$5.6\cdot10^{10}$	$2\cdot10^{10}-10^{11}$
wave frequency	MHz	200	$75-500$
gyro radii			
electron Larmor radius ρ_e	m	$3\cdot10^{-4}$	$10^{-4}-6\cdot10^{-4}$
ion Larmor radius	m	0.02	$0.01-0.04$
collision frequencies			
electron-ion ν_{ei}	MHz	8	$2-50$
electron-neutral ν_{en}	MHz	1	$0.6-4$

Table 5.1: Typical operational and plasma parameters for an argon discharge used in experiments presented subsequently. Fundamental physical constants are taken from [90] and the collision frequencies are calculated from [91].

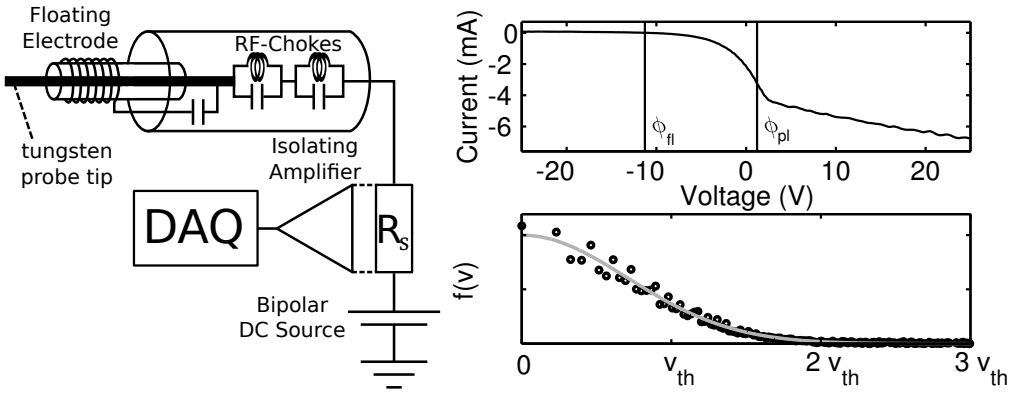

Figure 5.4: (a) Rf-compensated Langmuir probe. (b) Current voltage characteristic of a plane probe, plasma ϕ_{pl} and floating potential ϕ_{fl} are indicated. (c) Electron velocity distribution function extracted from (b).

5.2 Plasma Diagnostics

Plasma diagnostics used in the experiments are Langmuir probes [92, 93] and a 160 GHz microwave interferometer [94]. Spatially resolved time-averaged current-voltage characteristics are measured by Langmuir probes and evaluated using a kinetic model [95, 96]. The electron velocity distribution function, electron temperature and plasma density are extracted from the measurements. A microwave interferometer is used to perform radially line-integrated density measurements which are used to calibrate density profile measurements performed by Langmuir probes.

5.2.1 Langmuir Probes

The original work on Langmuir probes is formulated for unmagnetized collisionless, isotropic plasmas [96] in which the plasma parameters are constant in time. In a rf-plasma the plasma potential ϕ_{pl} is oscillating at the rf-frequency of the source. Those oscillations are compensated [97], a schematic of a rf-compensated Langmuir probe is depicted in figure 5.4 (a). The probe tip is inserted into the plasma and biased at a certain voltage, a floating electrode is coupled to the probe by a capacitor. Oscillations in ϕ_{pl} are compensated by the floating probe. Additional rf-chokes are connected in series with the probe in order to filter the rf-frequency and its first harmonic. The probe voltage is swept by a bipolar power supply and the probe current is measured via a shunt resistor R_S in series with the probe. Probes are insulated against the plasma by ceramic tubes and shielded against electro magnetic pick-up. Probe tips used have either a cylindrical or a planar shape. Figure 5.4 (b) shows the current-voltage characteristic of a plane probe. The characteristic is divided in three regions, first the electron saturation current region for voltages larger than ϕ_{pl}, second the transition region between ϕ_{pl} and

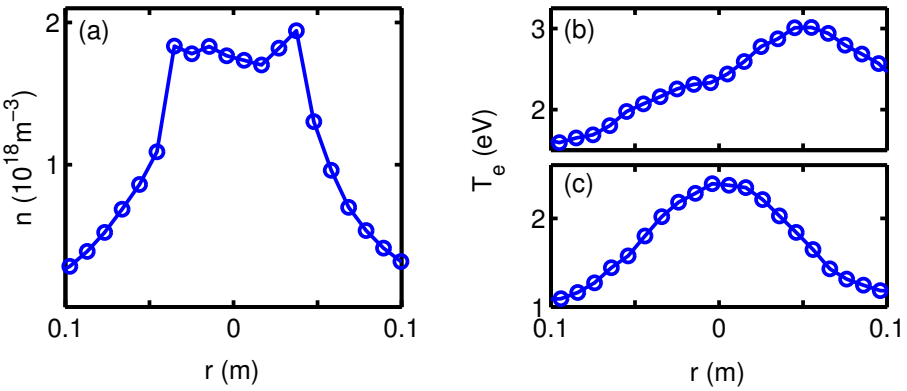

Figure 5.5: Typical radial profiles with the whistler wave exciter antenna installed in the device. (a) Ion-saturation current profile. Radial electron temperature profile along (b) and perpendicular (c) to the antenna support.

ϕ_{fl} and third the ion saturation current region for voltages below ϕ_{fl}. The plasma density is extracted from the ion saturation current, while the electron velocity distribution function is extracted from the transition region [98].
In the experimental results presented in figure 5.4 (b) the normal of the plane probe was parallel $\mathbf{B}_0$. The electron velocity distribution $f_{e,z}$ parallel $\mathbf{B}_0$ can be extracted from the transition region of the characteristic [96]

$$f_{e,z}(V) = \frac{m_e}{Ae^2}\frac{dI}{dV} \,, \tag{5.1}$$

where I is the current to the probe, $V = -m_e v_z^2/2e$ and A is the probe area. Figure 5.4 (c) shows the result together with the fit of a Maxwellian distribution function. An excellent agreement with a Maxwellian distribution is found, the temperature is $T_e = 3\text{eV} \pm 10\ \%$.
Subsequently presented Langmuir probe measurements have all been performed with cylindrical probes. The ion saturation current is given by

$$I_{i,sat} = \kappa n e A \sqrt{\frac{k_B T_e}{m_i}} \,, \tag{5.2}$$

where $\kappa = n_{probe}/n = \exp(-1/2)$ is the density drop at the sheath edge with respect to the unperturbed density and A is the effective probe surface. An estimate for the electron velocity distribution function f_e is extracted from the current voltage characteristics using a kinetic model [95]

$$f_e(V) = -\frac{4}{3\pi^2}\frac{m_e^2 \ln\left(\frac{\pi l_p}{4r_p}\right)}{e^3 \rho_e l_p V}\frac{dI}{dV} \,, \tag{5.3}$$

where r_p is the probe radius, l_p is the length of the probe tip and ρ_e is the Larmor radius of electrons. After substituting $V = -m_e v^2/2e$ a Maxwellian velocity distribution (2.30) is fitted to the data from which the temperature is extracted. Typical radial profiles are depicted in figure 5.5. As depicted in figure 5.3 an antenna is installed in the vacuum chamber which excites whistler waves. The antenna is positioned between the probe and the plasma source which leads to a perturbation of the plasma along the circumference of the antenna loop and the mounting of the loop. In figure 5.5 (a) the ion saturation current and in (b) the temperature are depicted, measured along a line including the mounting of the whistler wave exciter antenna. An asymmetry is found in the temperature profile in the direction parallel to the mounting, which is due to the perturbation by the rod supporting the antenna [99]. The ion saturation current profile shows the typical flat top shape of an inductive discharge and is not affected by the perturbations due to the exciter antenna. Figure 5.5 (c) shows a temperature profile along a direction perpendicular to the mounting. Along this direction the profile is symmetric.

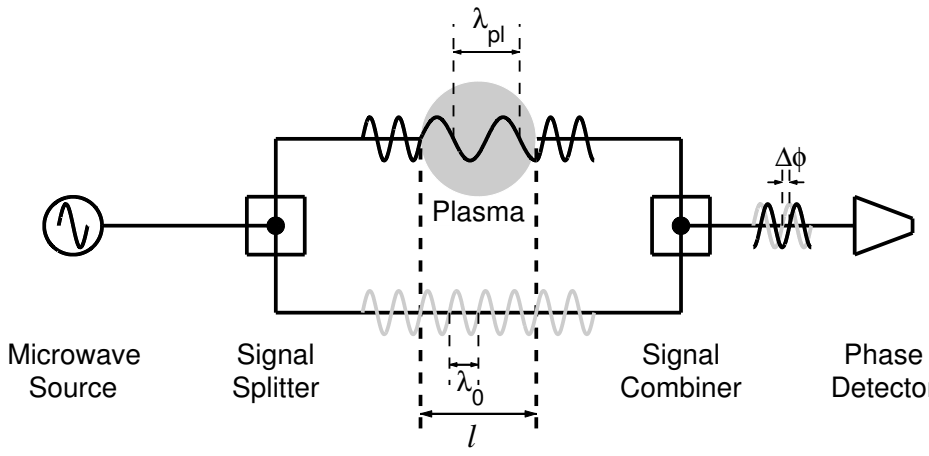

Figure 5.6: Schematic of the interferometer setup.

5.2.2 Microwave Interferometer

In comparison with probe measurements an interferometer has the advantage of being a non-intrusive diagnostic. A schematic of the interferometer principle is shown in figure 5.6. A microwave beam is radiated onto the plasma perpendicular to $\mathbf{B}_0$ in order to excite an O-mode wave. The O-mode propagates perpendicular to $\mathbf{B}_0$ with polarization $\mathbf{E}||\mathbf{B}_0$, its dispersion relation reads [59]

$$N = \frac{kc}{\omega} = \left(1 - \frac{\omega_{pe}^2}{\omega^2}\right)^{1/2} = \left(1 - \frac{n}{n_{cut}}\right)^{1/2} . \tag{5.4}$$

There is a maximum detectable density due to the O-mode cut-off $n_{cut} = \omega^2 \epsilon_0 m_e / e^2$. The phase velocity of the O-mode is larger than the velocity of light in vacuum. Hence, there will be a phase difference between a wave traveling a distance l through vacuum and an O-mode wave traveling the same distance through a plasma. If the phase difference between those waves is known conclusions about the density along the propagation path can be drawn. The phase difference is given by

$$\Delta\phi = k \int [1 - N(l)]\, dl = k \int \left[1 - \left(1 - \frac{n(l)}{n_{cut}}\right)^{1/2}\right] dl \, , \tag{5.5}$$

with $k = \omega/c$. For $n \ll n_{cut}$ (5.5) can be approximated by the first term in a Taylor expansion

$$\Delta\phi = \frac{k}{2n_{cut}} \int n(l) dl \, . \tag{5.6}$$

The phase difference $\Delta\phi$ is proportional to the line integrated density $\int n dl$. At the VINETA device a 160 GHz interferometer is used [94]. Thus, the cut-off density is $n_{cut} = 3.2 \cdot 10^{20}$ m^{-3} which is at least one order of magnitude larger than the peak density of the VINETA plasma. The typical result of an interferometer mea-

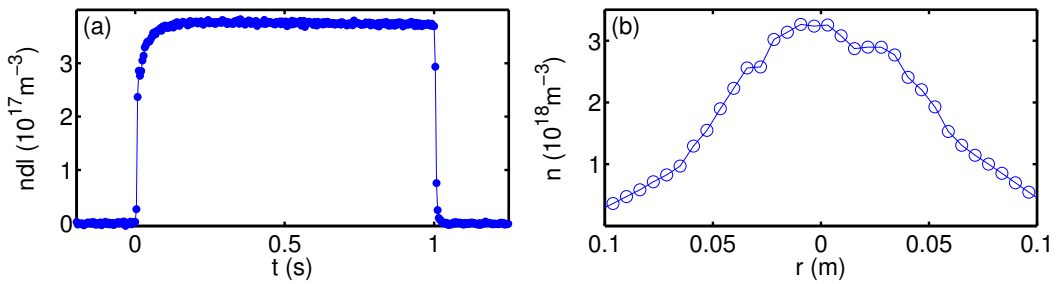

Figure 5.7: (a) Typical interferometer trace averaged over 20 plasma shots. (b) Density profile of an inductive discharge computed from an ion-saturation current profile normalized by the line integrated density measurement displayed in (a).

surement, of a 1 s plasma discharge is shown in figure 5.7 (a). After a certain rise time the plasma density reaches a steady state period. At the end of the shot the plasma source is switched off, but the plasma does not vanish instantly. From the interferometer trace an afterglow time of approximately 2 ms is found. The duration of the afterglow is determined by the Bohm sheath criteria [100, 101]. Ions in the current from the plasma to the boundary are found to have the ion sound speed c_s as their minimum velocity in the sheath, which together with the spatial dimension of the vacuum chamber determines the afterglow duration. Between the rise time and the afterglow the plasma density is constant, measurements are performed in this time window. In figure 5.7 (b) a density profile calibrated against the line-integrated density is shown.

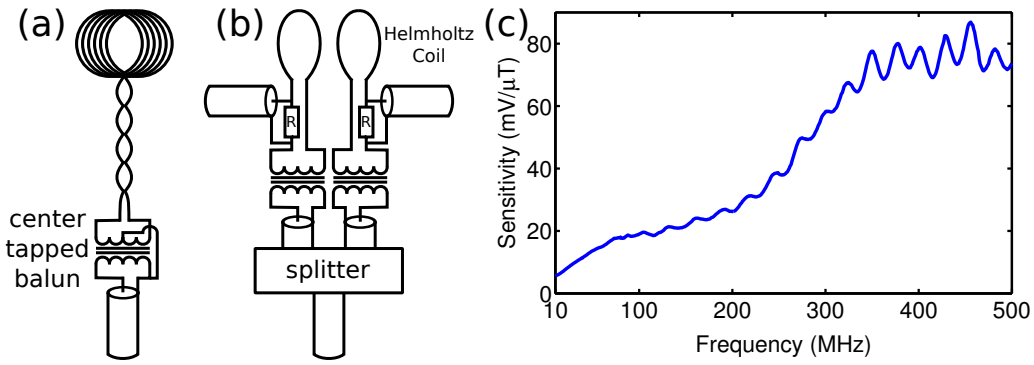

Figure 5.8: (a) Schematic of the $\dot{B}$-probe electronic circuit. (b) Setup for the calibration of $\dot{B}$-probes. (c) Typical dependency of the $\dot{B}$-probe sensitivity on frequency.

5.3 Wave Field Diagnostic and Excitation

Wave field diagnostics are magnetic fluctuation probes, called $\dot{B}$-probes [84] which allow for temporally and spatially resolved measurements of wave fields. Wave field excitation is performed by a magnetic loop antenna [36].

5.3.1 Magnetic Fluctuation Probe

A schematic of the $\dot{B}$-probe is shown in figure 5.8 (a). Due to the Faraday law a sinusoidal fluctuating magnetic field $\widetilde{B}$ induces a voltage V in a solenoidal coil

$$V = -Am\frac{d\widetilde{B}}{dt} = -Am\omega\cos(\omega t)\ , \tag{5.7}$$

where A is the coil area and m the number of windings. In the present case a coil with $m = 6$ windings of 2.5 mm in diameter is used. As shown by Franck *et al.* [84] capacitive pick-up rejection is efficiently achieved by a center tapped balun transformer. As depicted in figure 5.8 (a) the balun is connected between the coil and the signal line. The whole construction except of the coil is hermetically shielded by copper foil. In order to prevent saturation of the transformer ferrite core through the ambient magnetic field it is shielded by permalloy. All plasma facing components are electrically isolated and protected against the plasma by ceramics.

Calibration

$\dot{B}$-probes are calibrated for absolute values of the fluctuating magnetic field using the setup depicted in 5.8 (b) which essentially consists of a Helmholtz coil. Calibration is performed for frequencies between 10 MHz and 500 MHz. Helmholtz

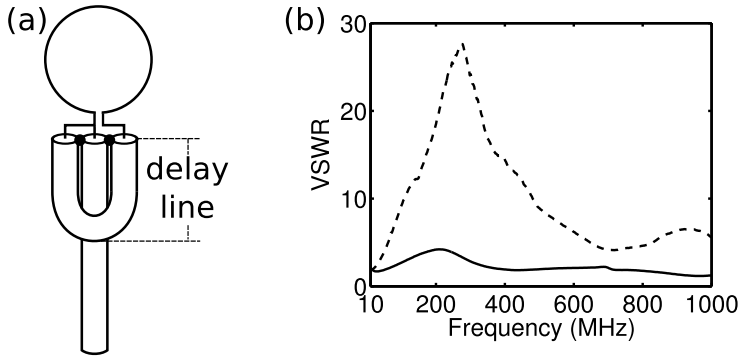

Figure 5.9: (a) whistler wave exciter antenna together with $\lambda/2$-delay line balun. (b) VSWR of the loop antenna if a 1:1 balun (dashed line) or 4:1 balun (full line) is used for symmetrization.

coils with such a large bandwidth need to be small. Therefore, a radius of $r = 1$ cm is chosen for the coils. In order to minimize run-time delays between the coils each coil is powered individually. The input signal for the coils is generated by splitting the signal supplied by a broad band function generator. Each individual signal is connected to the coil circuit after passing a balun transformer. A reference signal is decoupled from both coil circuits by monitoring the voltage drop above a $R = 50\ \Omega$ resistor with a high impedance sensor head. The Helmholtz coil was tested for homogeneity by scanning the field inside the coil volume with a $\dot{B}$-probe. A typical calibration result for the $\dot{B}$-probe is depicted in figure 5.8 (c). In the frequency range $10 \leq f \lesssim 80$ MHz the sensitivity exhibits a linear increase with frequency as expected from (5.7). At frequencies $f \gtrsim 80$ MHz the sensitivity does not grow linearly, but increases non-linearly and saturates for $f \gtrsim 400$ MHz. The length of the cable connecting the analyzer unit to the probe is $L = 3$ m which equals the wave length at $f \approx 100$ MHz. This means at frequencies close to 100 MHz the impedance matching of the probe to the cable will become important. In this frequency range the sensitivity is not only determined by (5.7), but also by the impedance matching to the signal line causing the non-linear increase. Moreover, parasitic capacities and inductances form resonant circuits which additionally modify the calibration curve.

5.3.2 Magnetic Loop Antennae

The loop antenna together with the $\lambda/2$-delay line balun and the feeding line is depicted in figure 5.9 (a), where the loop has a diameter of 4.5 cm. Rf-power is transfered to the antenna via a coaxial cable. A balun is connected between the coaxial cable and the antenna loop in order to achieve proper symmetrization of the unbalanced coaxial cable to the balanced antenna. Wave excitation is performed for frequencies 75 MHz $\leq f \leq$ 500 MHz. As depicted in figure 5.9 (b) the voltage standing wave ratio (VSWR) of the loop antenna is smaller, up to a magnitude of order, if connected to a 4:1 instead of a 1:1 balun. Since a small

VSWR means smaller losses on the coaxial cable a 4:1 balun should be used in the experiments. The balun is placed between the loop antenna and the feeding line inside the plasma. Therefore, a small installation size is needed in order to keep perturbations on the plasma small. Both criteria are matched by the $\lambda/2$-delay line balun. This segment of the antenna system is protected against the plasma by ceramics. As depicted in figure 5.3, the antenna system is matched to the amplifier system by a triple stub-tuner. The input power is monitored by a directional coupler, which simultaneously supplies the reference signal used in data processing. Since a broad band amplifier providing 50 W of rf-power is used, magnetic wave field amplitudes with peak values of $\widetilde{B}_x \leq 20$ μT are excited at a distance of 5 mm from the loop circumference. Since the wave amplitude for $z > 5$ mm is small $\widetilde{B}_x/B_0 \lesssim 0.2$ % non-linear effects due to the wave field are avoided.

6 Investigations on Wave Propagation

6.1 Axial Evolution of the Wave Field

Experimental investigations are performed in a parameter range in which the parallel wave length of whistler waves predicted by plane wave dispersion theory is equal or smaller than the diameter of the plasma column, exceptions are indicated. Figure 6.1 shows results from the measurement of a wave field along the symmetry axis of an inductive discharge for plasma parameters at which the parallel wave length predicted by dispersion theory is smaller than the plasma diameter. Magnetic fluctuations perpendicular to the ambient magnetic field are investigated. Therefore, time series are measured at equally spaced points along the symmetry axis for a fixed excitation frequency. The measurement is performed in the afterglow of the discharge in order to avoid contributions of the helicon antenna rf-field to the measurement. A typical spectrum taken from a time series measured at axial distance $z = 8$ mm from the wave exciter is depicted in figure 6.1 (a). Wave excitation is performed at a frequency of $f = 83$ MHz at which the largest peak is found. In addition to this peak higher harmonics are found which stem from the excitation. The harmonics are filtered out during data processing. The signal to

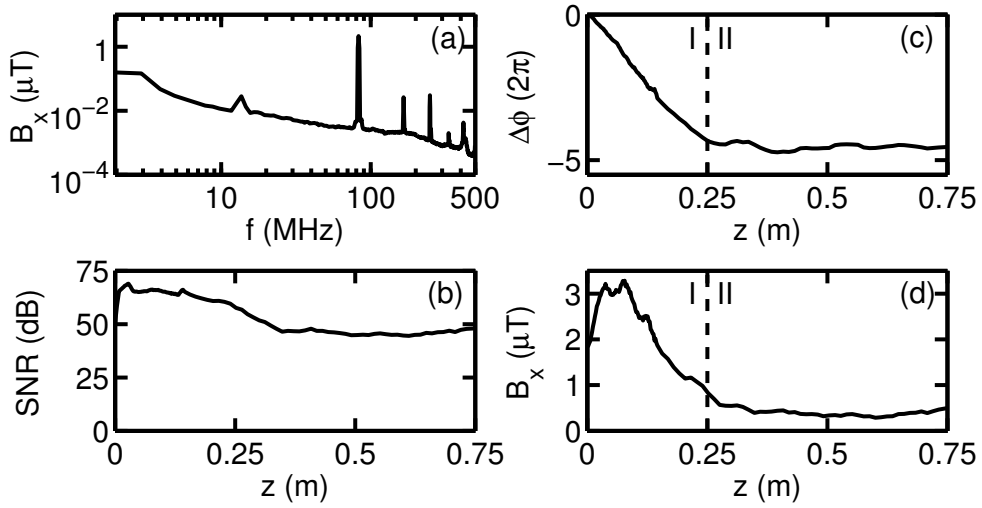

Figure 6.1: Probe spectrum (a) in an afterglow plasma both axes scaled logarithmically. Signal to noise ratio (b), phase evolution (c) and amplitude evolution (d) along the symmetry axis of the plasma.

noise ratio (SNR) at this position is found to be about 50 dB. As figure 6.1 (b) shows it stays in this range throughout its entire axial evolution and disturbances due to the noise are negligible. The axial phase evolution of the wave depicted in figure 6.1 (c) shows two regimes, where regime I is found in the axial range for $z < 0.25$ m and is characterized by a distinct slope in the phase evolution. Regime II is found at larger distances and is characterized by an almost constant value of the phase. The phase velocity in regime II is close to the velocity of light. Thus, the wave found in regime II is not expected to be a whistler wave. Figure 6.1 (d) shows the axial evolution of the amplitude, which is also divided in two regimes. In regime I the wave field amplitude is relatively large with values $|\widetilde{B}| > 1$ μT while the values found in regime II are smaller than in regime I up to an order in magnitude.
Since the vacuum wave length at 83 MHz is smaller than the vacuum chamber length cavity modes are excited. Those modes propagate at about the speed of light and are therefore much faster than the whistler waves excited in the VINETA device. Since the cavity mode has an amplitude which is much smaller than the wave amplitude in regime I it is not visible in this region. However, the almost constant phase and amplitude in regime II is due to a cavity mode.

6.1.1 Wave Dispersion and Damping

The heating of the plasma is not present in the afterglow. Therefore, the electron temperature of the plasma in the afterglow is much smaller than in the steady state plasma [102]. Consequently the damping due to collisions in the steady state plasma is much weaker than in the afterglow plasma and the wave propagates further into the plasma before it is damped away. Therefore, subsequently presented investigations are all performed in the steady state plasma. In comparison the phase evolution in both cases is qualitatively equal, but the amplitude evolution in a steady state plasma differs from the one in the afterglow. In order to explore the dispersion and the damping of the excited fluctuations, the magnetic fluctuations are measured along the symmetry axis of the plasma in the axial region in which the cavity mode is negligible. Figure 6.2 (a) shows an exemplary set of the measured time series. The time evolution of a particular point on a phase front is illustrated by a line running through all of the depicted time series. In order to illustrate the time evolution of all points the measured time series are combined to a spatiotemporal plot in figure 6.2 (b). Plotted along the abscissa is the time and along the ordinate is the axial position z. The fluctuating amplitude of the wave $\widetilde{B}_x = B_x \sin \Delta\phi$ is plotted color coded. A typical striped pattern is found, where the tilt of the stripes is equal to the one of the line found in figure 6.2 (a) and represents the phase velocity of the wave. The spatial Fourier transform of the wave field is shown in figure 6.2 (c). From a fit of a Gaussian to the spectrum the effective parallel wave vector k_r of the excited wave is determined. The value extracted from the measurement coincides with the prediction of the plane wave dispersion relation typically within an uncertainty of less than 10 % although the

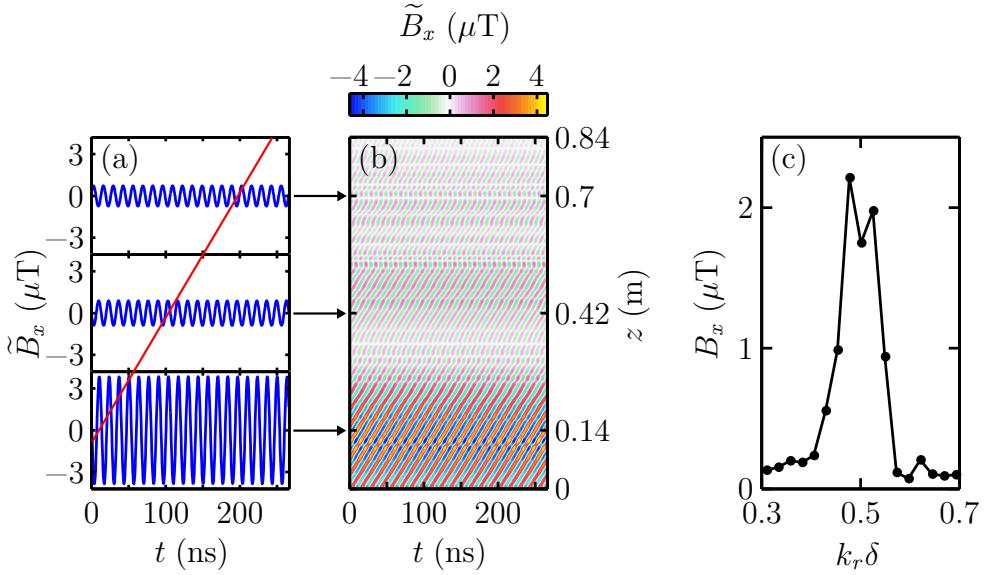

Figure 6.2: Procedure for the construction of the spatiotemporal representation of magnetic fluctuations along the plasmas symmetry axis from the measured time series (a-b) together with the spectrum of parallel wave numbers (c). Plasma parameters in the plasma center are given by $\gamma = 0.02$, $\beta = 2.4 \cdot 10^{-2}$, $\nu = 8 \cdot 10^{-3}$ and the normalized frequency by $\omega/\omega_{ce} = 0.24$.

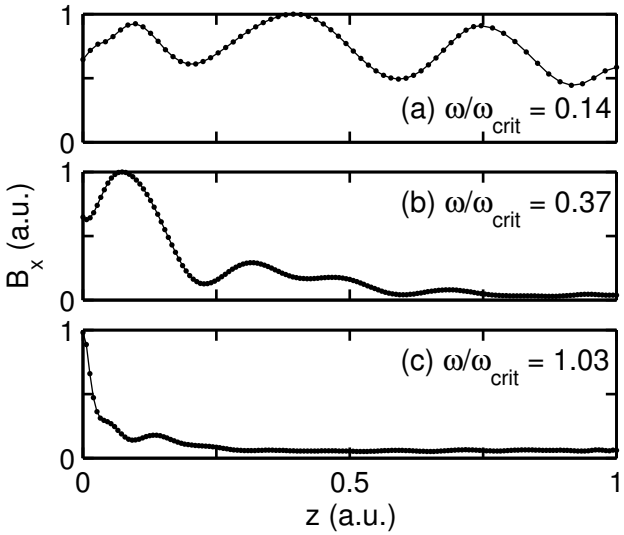

Figure 6.3: Amplitude runs along the symmetry axis of the plasma in inductive discharges for three different ratios of wave to critical frequency.

spectrum shows a broad width of wave numbers instead of a single one. Since the mean value of the spectrum is close to the parallel wave number predicted by plane wave dispersion theory, it is used to carry out first order estimates on wave propagation. The amplitude patterns in a steady state plasma are characterized by the ratio of excitation frequency to critical frequency predicted by the hot plasma

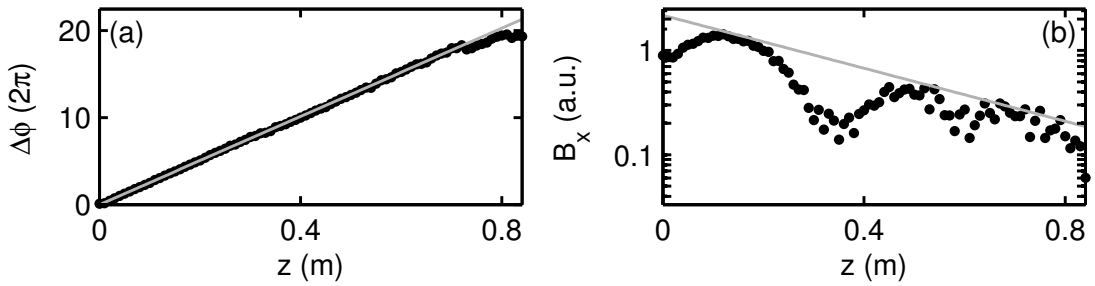

Figure 6.4: Illustration of the procedure for the extraction of the parallel wave and damping length from measurements of the wave field along the symmetry axis of the plasma. Parameters are given in figure 6.2.

dispersion theory. Figure 6.3 shows amplitude runs along the plasma center for three different ratios of wave to critical frequency. The predicted damping of the wave is negligible in the case presented in figure 6.3 (a). The case presented in figure 6.3 (b) corresponds to weak damping and an amplitude run for the case of strong damping is shown in figure 6.3 (c). Oscillations are found in each case, where the oscillation strength is large for negligible damping and decreases with increasing damping. In addition to the oscillations an exponential decay of the amplitude curves envelope is found. The damping length found experimentally decreases with an increasing ratio of critical to wave frequency. For frequencies larger than the critical frequency the distance above which wave propagation is observed becomes very small. As a first order estimate for the damping length the damping length of the amplitude curves envelope is used. Figure 6.4 (d) shows the axial evolution of the phase of the wave. In the range of constant phase velocity a linear function is fitted to the data and the wave vector k_r is extracted from the slope of the function, as discussed in chapter 3.1. The values determined from the spectrum and the phase evolution agree almost perfectly. If the damping of the wave is stronger the distance above which wave propagation is observed becomes small. The spectrum of the excited parallel wave vectors can not be determined sufficiently precise at those frequencies. Thus, the phase evolution along the symmetry axis of the plasma is employed for the determination of the wave vector. Figure 6.4 (d) shows in a similar representation the amplitude run. The spatial damping increment k_i of the wave is extracted from the envelope of the amplitude pattern over the axial distance above which the phase velocity is constant. Also k_i agrees with the prediction from the hot plasma dispersion relation typically within an accuracy of less than 10 %.

A typical result of a wave dispersion measurement along the symmetry axis of the plasma is shown in figure 6.5. The fluctuating magnetic field of the wave is measured in both directions perpendicular to the ambient magnetic field. Figure 6.5 (a) depicts the spatial damping increment over frequency for both magnetic field components. The experimental results for the transversal directions are depicted as circles and crosses. Moreover, the prediction for the spatial damping increment in a collisional cold plasma is depicted. Experiment and prediction

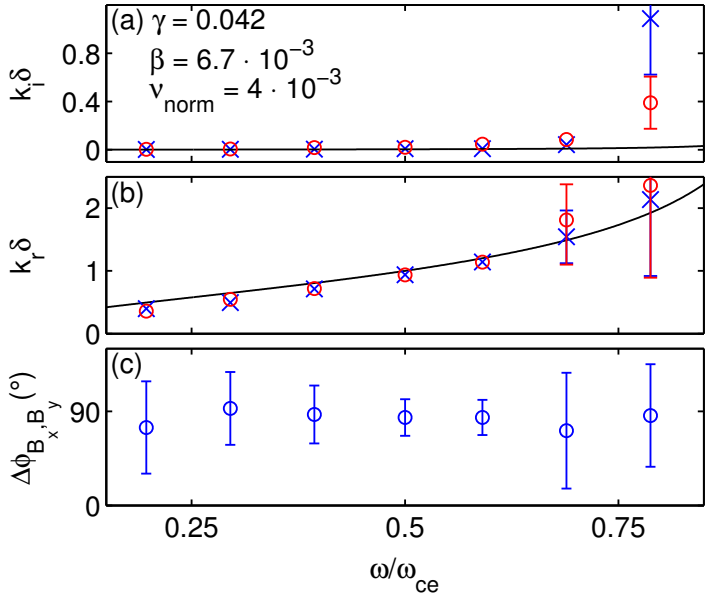

Figure 6.5: Wave dispersion relation for a cold collisionless plasma (full line). Crosses and circles denote the experimental results for the fluctuating magnetic field transversal to the ambient magnetic field along the plasmas symmetry axis in (a) and (b). The average phase shift between the transversal fields is depicted in (c). Error bars are plotted only if larger than the corresponding markers.

agree for frequencies $\omega/\omega_{ce} < 0.6$. At higher frequencies the damping increment found in the experiment is larger than the one predicted by the cold collisional dispersion relation. Since the critical frequency is $\omega_{crit}/\omega_{ce} = 0.72$ this signals the onset of kinetic effects due to the finite temperature of the plasma. A discrepancy between the cold plasma prediction and the experimental result is also found in the parallel wave vector. As depicted in figure 6.5 (b) the experimental result agrees with the prediction by the dispersion relation for frequencies $\omega/\omega_{ce} < 0.6$, where only small differences between the dispersion relation and the experiment are found for frequencies $\omega/\omega_{ce} < 0.4$. The large error bars at high frequencies are due to the strong damping which causes small amplitudes at those frequencies. However, the agreement of experiment and predictions for frequencies below this limit are surprisingly good. In a homogeneous plasma the whistler wave polarization is predicted as circular and in an inhomogeneous medium elliptic. In both cases the predicted phase shift between the transversal magnetic field components is 90°. Figure 6.5 (c) depicts the averaged phase shift of the wave along the symmetry axis of the plasma, which shows a good agreement with the shift expected for whistler waves. The amplitudes of the magnetic field B_x and B_y are not found to be identical, which indicates an elliptic polarization.

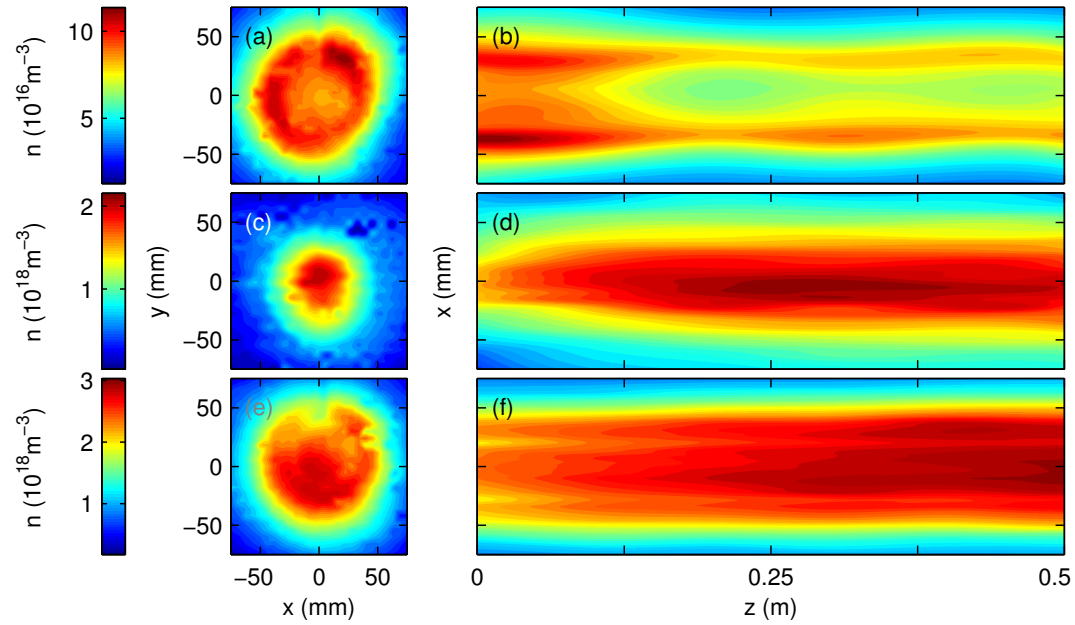

Figure 6.6: Plasma density profiles with typical inhomogeneities used for investigations about the propagation of loop antenna excited whistler waves. Density profiles in azimuthal planes are measured with a spatial resolution of $\Delta x = \Delta y = 6$ mm, while the profiles in xz-planes are measured with a resolution of $\Delta x = 6$ mm and $\Delta z = 100$ mm.

6.2 Effect of the Plasma Density Profile

Subsequently wave propagation in the whistler wave frequency range is investigated either in an azimuthal or xz-plane. At each point the temporal evolution of the fluctuating magnetic field $\widetilde{B}_x = B_x \sin \Delta\phi$ perpendicular to the ambient magnetic field is measured. The amplitude of the field is extracted from the measured time series through a Fourier analysis, while the phase of the wave field is extracted from a cross-power spectral density analysis of the magnetic field and the excitation signal. In graphical representations the data are interpolated. Whistler waves are excited at frequencies for which the influence of kinetic effects on wave propagation is negligible. Thus, the temperature profile of the discharge is unimportant and only the density profile needs to be considered.
As discussed in chapter 4.1 plasma density inhomogeneities have an important influence on whistler mode wave propagation. In order to elucidate the influence of radial plasma density inhomogeneities on the dispersion properties of the wave along the symmetry axis of the plasma, wave propagation in three different plasma density profiles is investigated.
Depicted in figure 6.6 (a) is the plasma density profile of a capacitive discharge in an azimuthal plane. In such a discharge the plasma density profile is hollow and the density decreases radially outwards. This pattern persists throughout the entire axial evolution, see figure 6.6 (b). Although, an axial gradient in the

plasma density is present. The plasma density profile of a helicon discharge in an azimuthal plane is depicted in figure 6.6 (c). Such a discharge is peaked in the plasma center and possesses large density gradients in the radial direction. The density profile in a xz-plane depicted in figure 6.6 (d) exhibits an axial evolution in the width and the maximum value of the peak in the plasma center. However, the gradient in the radial direction is always larger than the one in the axial direction. In an inductive discharge the plasma density profile is flat in a circular region around the plasma center $r < 5$ cm, as the azimuthal plasma density profile depicted in figure 6.6 (e) shows. Figure 6.6 (f) shows the plasma profile in a xz-plane which exhibits an extension of the region of homogeneity along the entire axial direction. As found in the previous cases there are perturbations on the plasma density homogeneity. Those perturbations are again small compared to the radial gradient for $r \gtrsim 5$ cm. Deviations of the plasma profiles from their ideal shapes are at least partially due to the whistler wave exciter which is installed in the device at an axial position of $z = 0$ m.
In order to investigate the mode structure of the excited wave the x-component of the fluctuating magnetic field is analyzed for each plasma profile in an azimuthal plane at an axial distance of $\Delta z = 6.5$ cm to the loop antenna. Figure 6.7 depicts the result for (a) the hollow plasma profile, (b) the peaked plasma profile and (c) the flat plasma profile. Each field is excited at a frequency of $f = 200$ MHz. Corresponding plasma parameters in the plasma center are indicated to the right of each measurement.
The x-component of the wave field is radially anti-symmetric at least in the region of high amplitudes. Plane wave dispersion theory predicts azimuthal symmetry of the waves phase which implies radial symmetry, see chapter 2. Thus, a mode substantially differing from a plane wave is excited in all of the plasma profiles. In order to elucidate the mode structure of the excited wave a mode analysis of the azimuthal mode is performed a the radial position indicated in the measurements by a white circle. The radius of the circle equals the radius of the loop antenna and shows the position at which the maximum in the magnetic field amplitude is found. A mode is characterized by the number of wave lengths in the fluctuating field found along a certain spatial direction. The fluctuating field along the circle indicated in the measurement is shown to the right of each measurement above a Fourier transform of the curve, which allows for a systematical analysis of the mode number. In the hollow profile a single maximum and a single minimum is found along the indicated circumference. As expected the spectrum shows that this corresponds to an $m = 1$ azimuthal mode. In the peaked profile the field amplitude along the circle is qualitatively equal to the one found in the hollow profile, but shows a substructure consisting of local maxima and minima. The mode analysis clarifies that again an $m = 1$ mode is found to dominate, but there are contributions from higher mode numbers. A second maximum is found corresponding to an $m = 3$ mode. In the flat profile a similar result is found. Also in this case dominance of an $m = 1$ mode is found, while an $m = 2$ mode is found as a sub dominant contribution. Hence, in this representation a $m = 1$ azimuthal mode pattern in the magnetic field component $\widetilde{B}_x$ is found. Obviously a single

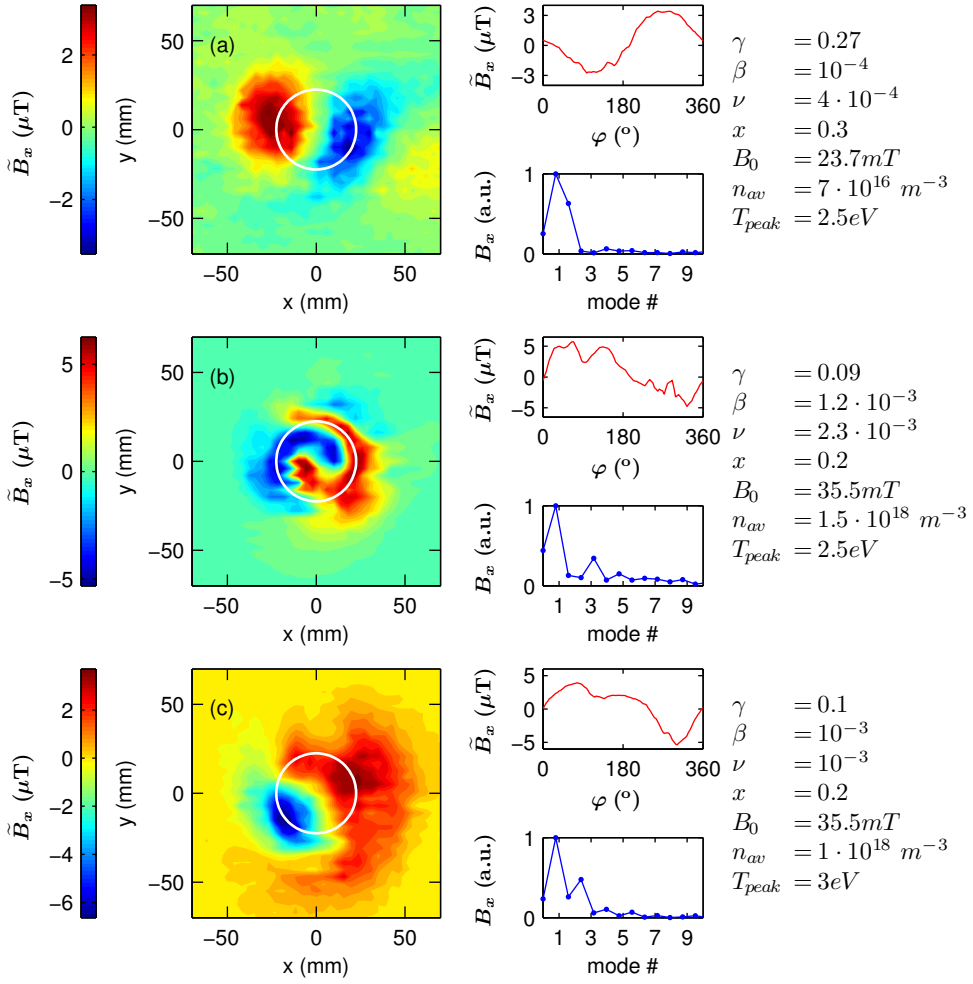

Figure 6.7: Whistler wave magnetic field in an azimuthal plane for three plasma density inhomogeneities. The spatial resolution of the measurement is $\Delta x = \Delta y =$ 4 mm. An analysis of the azimuthal mode structure and plasma parameters in the plasma center are shown to the right of each wave field.

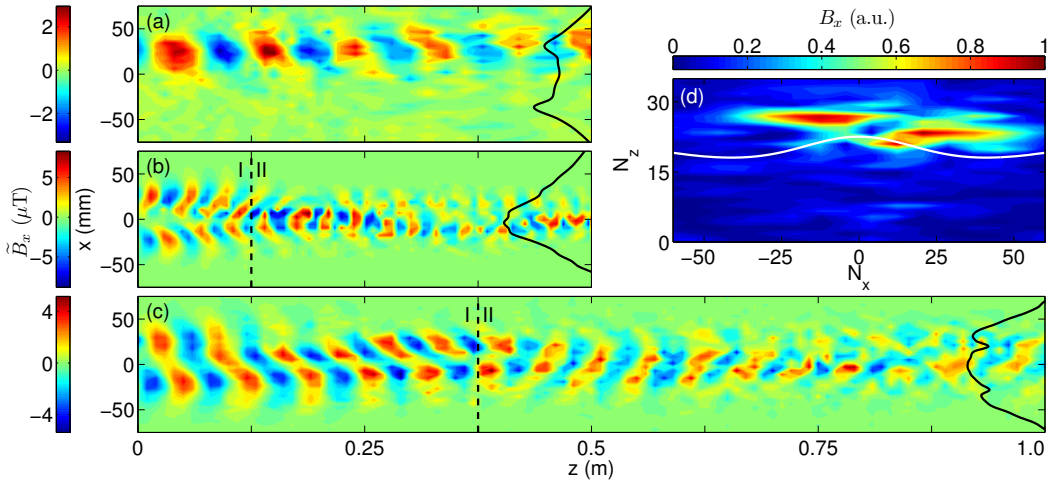

Figure 6.8: Axial evolution of the fields depicted in figure 6.7 exhibiting ducting of the wave in regions with high plasma density. A Fourier transform of the field in (c) is depicted in (d) together with an index of refraction surface.

maximum in the radial direction is found to dominate. The mode spectrum for the hollow profile is the comparatively simplest one. In space the mode structure found in the hollow profile is given by two regions of opposite polarity, separated by a region in which the amplitude is almost zero. In the peaked profile the regions of opposite polarity are in close vicinity to each other. Furthermore, they are entangled in the shape of a double spiral. The regions of opposite polarity in the flat profile are also in close vicinity, though they are not entangled or completely symmetric. In order to clarify the cause of the differences observed, the fluctuating magnetic field is investigated in an xz-plane.

Measurements of $\widetilde{B}_x$ in a xz-plane for each type of inhomogeneity are performed in order to investigate the axial evolution of the excited mode and the ducting of the wave in each plasma profile. Depicted in figure 6.8 is the wave field for the hollow profile (a), peaked profile (b) and flat profile (c). The spatial resolution of the measurements is (a) $\Delta r = 4$ mm, $\Delta z = 10$ mm, (b) $\Delta r = 4$ mm, $\Delta z = 7$ mm and (c) $\Delta r = 4$ mm, $\Delta z = 10$ mm. An exemplary radial density profile is depicted for each measurement.

In the hollow profile wave energy is ducted mainly along one of the peaks with maximum plasma density. Thus, the wave field is not ducted symmetrically with respect to the symmetry axis of the plasma. This explains the gap between the regions of opposite polarity in figure 6.7 (a). The radial variation of the density in the peaked profile causes a variation in the waves parallel and perpendicular phase velocity. This causes the entanglement of the pattern depicted in figure 6.7 (b) and an effective focusing of wave energy to the plasma center. Such a variation is not present in the case of a flat profile leading to an almost constant parallel phase velocity within the plasma radius and a wider width of the wave field during its axial evolution.

In the case of the peaked and the flat profile wave propagation can be divided

into two regions. Domain I begins at the whistler wave exciter and extends up to a certain axial position, indicated in the plots, after which domain II begins. In domain I the power radiated from the loop antenna is localized in a region along the circumference of the antenna. If the distance to the antenna increases the radius at which the amplitude maximum occurs becomes smaller until it merges to a single amplitude maximum in the plasma center. This initiates domain II characterized by a single amplitude maximum which performs lateral excursions around the plasma center during forward propagation. In this aspect, the major difference between the peaked and the flat profile is the distance over which domain I extends into the plasma, which is about 0.125 m for the peaked and 0.375 m for the flat profile. Moreover, the width of the wave field in the peaked profile is smaller due to the smaller width of the plasma density profile. A ducting of the excited wave in the region of high density is found. The lateral excursions of the amplitude maximum from the plasma center are supposedly due to axial perturbations on the plasma density.
In order to elucidate the differences between wave propagation in domain I and domain II the field depicted in figure 6.8 (c) is transformed to Fourier space. The power spectrum is depicted in figure 6.8 (d) over the index of refraction together with an index of refraction surface for plane waves. Domain I is represented by the peaks for $N_x > 0$ and domain II by the peak for $N_x < 0$. The analysis illustrates a change in the direction of wave propagation. In domain I the spectrum is given by two peaks which are neighboring each other while it is given by one peak in domain II. The peaks in both domains are wider in the perpendicular direction than in the parallel direction. A certain width of the spectrum is found in each direction indicating a broad spectrum of oblique propagating plane waves. This is expected from complementary experimental investigations [40, 103] which show that a loop antenna is found to induce a current pattern in the plasma corresponding to a multitude of oblique propagating plane waves grouped around a central wave vector in Fourier space. This is due to the radial anti-symmetric current of the loop antenna which constrains a fluctuating magnetic field parallel to the ambient magnetic field. In turn this implies excitation of oblique propagating modes since parallel propagating whistler waves posses no parallel field components.
Figure 6.9 shows the phase and amplitude evolution along the axial direction in the region of wave ducting for the hollow profile at the position of the maximum amplitude $r \approx 22$ mm (a)-(b) and in the plasma center for the peaked profile (c)-(d) and the flat profile (e)-(f). The parallel wave and damping length extracted from the experimental results together with the prediction from the dispersion relation are indicated below the corresponding measurement. The agreement between experiment and the prediction of the plane wave dispersion relation for the wave length is found to improve going from the hollow to the peaked profile. In the case of a flat profile the experiment and the prediction agree almost perfectly at least in the plasma center. This result is not self-evident since the excited wave is not a plane wave. This is reflected in the amplitude run which does not coincide with the prediction of the dispersion relation. Instead a damping length which is much smaller than the one predicted by the plane wave dispersion relation is found

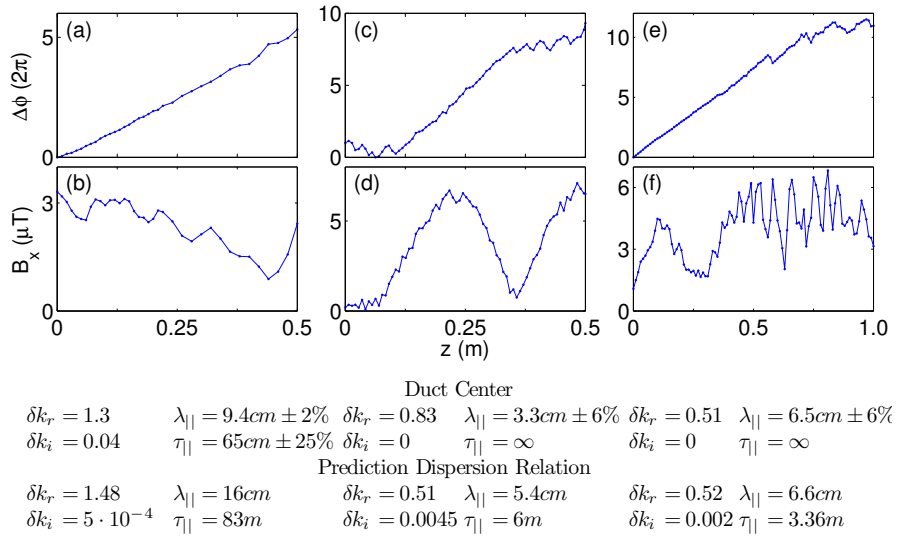

Figure 6.9: Axial evolution of the phase and amplitude along a 1D cut for the wave fields shown in figure 6.8.

for the hollow profile. The cause for this difference is given either by geometric effects like leakage of wave energy from the duct or by three dimensional effects which are not accounted for in two dimensional measurements. In contrast to this result the amplitude evolution of the wave field in the peaked and the flat profile shows no damping at all, but exhibits undamped oscillations. Hence, the plasma density profile is found to have an important influence on the propagation of the wave. In hollow profiles the wave is found to propagate off-axis, a symmetry with respect to the plasma center is not present over the entire axial evolution. In peaked and flat profiles the wave propagates mainly on-axis with small excursions from the plasma center. Since the parallel phase velocity in the case of a flat profile is approximately constant over the plasma radius and agrees with predictions from plane wave dispersion theory investigations on whistler wave propagation are performed in flat profiles.

6.3 Characterization of the Excited Mode

A comparison of wave propagation in an flat density profile with a simulation in a Gaussian profile at corresponding plasma parameters is shown in figure 6.10. The measurement presented in figures 6.7 (c) and 6.8 (c) is decomposed in its phase and amplitude in figure 6.10 (a)-(d). Depicted in figures 6.10 (e) and (f) is the simulated wave field in the same planes as for the measurements. The decomposition into instantaneous phase and amplitude is shown in figures 6.10 (g)-(j). If the wave fields in the azimuthal planes are compared at least a qualitative agreement is found. The wave field predicted by the simulation exhibits radial antisymmetry, which is also found in the experiment close to the whistler wave exciter to a good

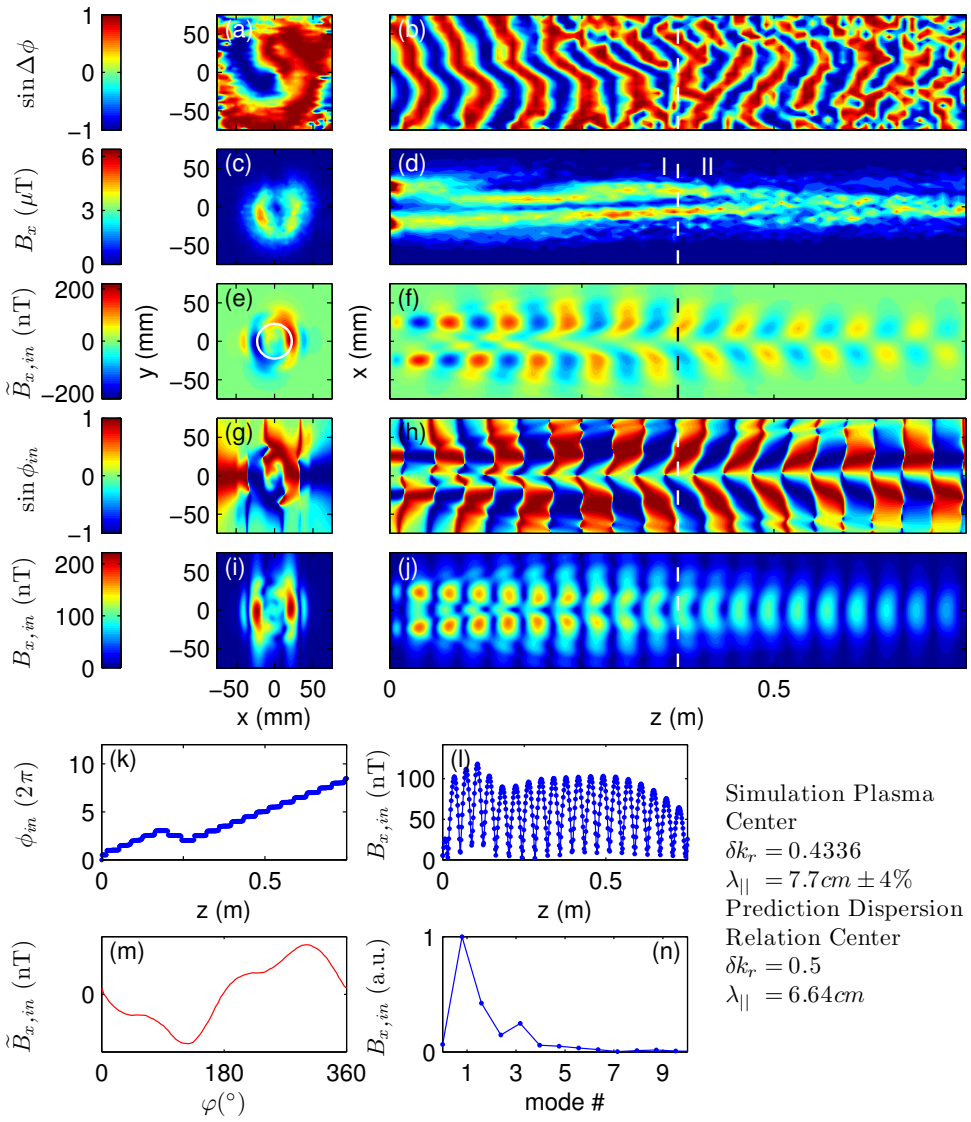

Figure 6.10: Comparison between the experiment presented in figure 6.8 (c) and a simulation with parameters of set II at t/T = 15. The azimuthal plane has a distance of $\Delta z = 0.065$ m to the exciter antenna.

approximation. Thus, the mode structure of the simulation and the experiment coincide in this region termed domain I in the preceding discussion. In domain II the amplitude pattern shows a good agreement, but the phase pattern does not. There are several possible causes for this difference. The simulation is not in continuous wave mode in this region, it does not include damping by collisions neither asymmetries or axial variations in the density.
The axial evolution of the phase in the plasma center is depicted for the simulation in figure 6.10 (k) and the evolution of the amplitude in (l). The normalized parallel wave vector and the wave length extracted from figure 6.10 (k) are indicated together with the prediction by the dispersion relation. A good agreement is found as expected from the comparison of the experiment with the prediction below figure 6.9 (e). The amplitude curve depicted in figure 6.10 (l) exhibits short scale fluctuations which are due to the mode structure. Those are not present in the curve for the corresponding experiment shown in figure 6.9 (f) since the simulation is shown for a time point while the amplitude in the measurement is a time averaged quantity. However, at least the envelope of the simulations amplitude shows a qualitative agreement with the measurement.
In the simulations a plasma density profile with a Gaussian shape is assumed, while a flat profile is generate in the experiments. Thus, the plasma density profile of the simulations has common features with a peaked profile, e.g. conical phase fronts as in the experiment depicted in figure 6.8 (b) in domain I. Since the difference in the plasma profile shapes is minimized the influence of the antenna induced current pattern dominates over the difference in the plasma density profile in domain I. Therefore, simulations and measurements are comparable in this region. The difference between simulation and experiment in domain II is at least partially due to the different plasma density profiles. Thus, from the agreement of the simulation and the experiment in domain I a conclusion on the mode excited by the loop antenna in the experiments close to the exciter is possible using the simulation. Figure 6.10 (m)-(n) shows a mode analysis in the same manner as performed for the experiments presented in figure 6.7. The amplitude evolution along the circumference indicated in figure 6.10 (e) exhibits a higher degree of radial anti-symmetry than the one found in the measurement presented in figure 6.7 (c). In the mode spectrum occurrence of an $m = 1$ and an $m = 3$ mode in the simulation is observed, while in the experiment an $m = 1$ and an $m = 2$ mode is found. However, in both analyses the $m = 1$ mode is the dominant mode in the $\widetilde{B}_x$ component. Although the mode structure of the $\widetilde{B}_x$ component found in azimuthal planes appears as an $m = 1$ mode the simulations show that an $m = 2$ mode is excited if the remaining spatial directions are included in the analysis, see chapter 4.2. Therefrom, excitation of an $m = 2$ mode in the experiments is concluded.
In order to determine wave propagation at different frequencies and plasma parameters additional experiments are performed. The experiments are compared to corresponding simulations in order to test if an agreement is found over the whole parameter range. Presented in figure 6.11 is a second comparison between an experiment in a flat density profile and a simulation assuming a Gaussian pro-

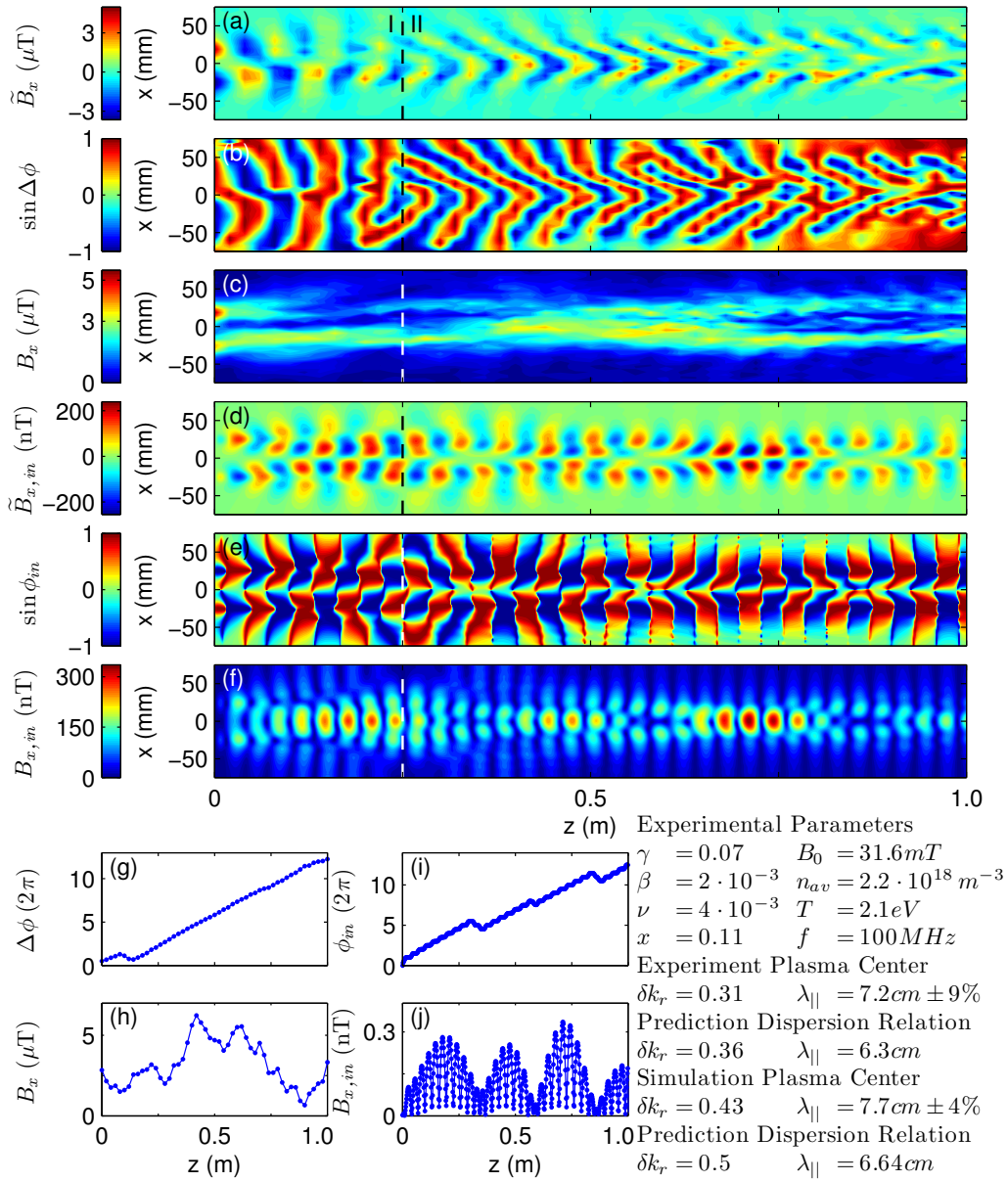

Figure 6.11: Comparison between an experiment and a simulation. Plasma parameters in the plasma center are indicated for the experiment for which data are taken with a spatial resolution of $\Delta x = 4$ mm, $\Delta z = 20$ mm. The simulation is performed for parameters from set III, it is shown at t/T = 20.

file. Figure 6.11 (a) depicts the wave field and its decomposition in (b) phase and (c) amplitude. Again the propagation pattern can be divided in two domains. In domain I ($z \lesssim 0.25$ m) an approximately antisymmetric pattern in the phase is found, while it is symmetric to a good approximation in domain II. The amplitude in the x-direction is approximately symmetric except in the axial region 0.125 m $\lesssim z \lesssim$ 0.375 m. Close to the antenna in domain I the amplitude pattern is given by maxima along the circumference of the antenna and a minimum in the center of the antenna. The maxima unify at $z \approx 0.5$ and reoccur at larger distances. Figure 6.11 (d) depicts the fluctuating magnetic field and its decomposition in (e) instantaneous phase and (f) instantaneous amplitude for the simulation. Wave field and phase show an anti symmetry in the x-direction. In contrast the amplitude is symmetric. An agreement between experiment and simulation is found in the phase pattern in domain one, while the amplitude pattern agrees only gradually along the entire axial direction. In figure 6.11 (g) the phase evolution and (h) the amplitude evolution of the wave along the symmetry axis of the plasma found in the experiment is depicted. The same is shown for the simulation in figures 6.11 (i) and (j). A comparison of the phases shows an almost equal parallel wave length as indicated in the figure. Neglecting the short scale fluctuations due to the mode structure of the wave in the simulation, the amplitude evolution of the wave field in both cases shows oscillations. Although, the specific shape of the oscillations is different from each other. This is partially due to the fact that the simulation shows an instance of time while the measurement shows time averaged quantities. Thus, the comparison shows that experiment and simulation have common features in domain I and differ at larger distances. Therefore, the mode excited in the experiment will receive at least a noticeable contribution from an $m = 2$ mode. The cause for the difference in the amplitude evolution is discussed at the end of the chapter.
Figure 6.12 depicts an experiment performed at plasma parameters for which the plane wave dispersion relation predicts the smallest parallel wave length if compared to the preceding experiments. The wave field is depicted in figure 6.12 (a) and its decomposition in (b) phase and (c) amplitude. Again two domains are found. This time distinguished by their amplitude pattern. In domain I ($z \lesssim 0.125$ m) the amplitude pattern consists of an amplitude maximum along the circumference of the antenna, while a minimum is found in the center of the antenna. In domain II a single amplitude maximum is found which is slightly off center but develops toward the center with increasing axial distance from the exciter. The phase of the wave field is neither symmetric nor distinct anti symmetric during its axial evolution. However, in the region of the amplitude maximum in domain II the phase fronts appear plain in this representation. In contrast to the preceding experiments the cable feeding the loop antenna is situated inside the plane at $x < -22.5$ mm and not perpendicular to the plane. The asymmetry in the amplitude and the difference in the phase evolution in domain one for $x > 22.5$ mm and $x < -22.5$ mm is supposedly due to this asymmetry. The phase evolution in the plasma center (blue) and along the perpendicular position of the amplitude maximum (red) is depicted in figure 6.12 (d). Both curves lead

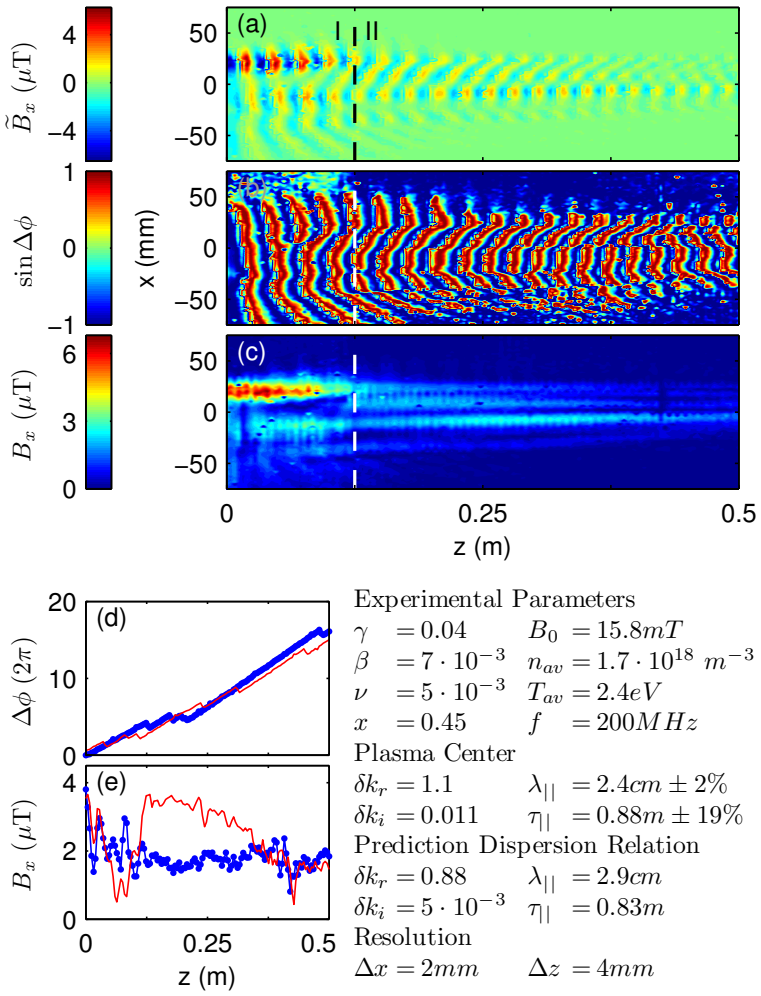

Figure 6.12: Wave propagation in a flat profile with a parallel wave length which is a quarter of the plasma diameter, plasma parameters in the plasma center are indicated.

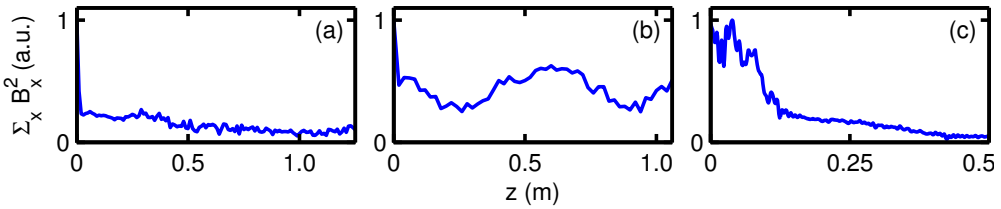

Figure 6.13: Estimation on the axial evolution of the wave energy inside the plasma radius for the measurements depicted in figures 6.10, 6.11 and 6.12.

to a similar parallel wave length indicated in the figure. Moreover, the amplitude evolution at both positions is depicted in figure 6.12 (e). In this case a difference is found. The amplitude in the plasma center is almost constant, while it exhibits oscillations at the radial position of the amplitude maximum. The maximum at $z = 0.125$ m is due to ducting effects, which are at least partially visible in the wave field. In this representation wave energy is found to be ducted from the upper to the lower half of the xz-plane depicted. A comparable simulation is depicted in chapter 4.2 in figure 4.7. In domain I a good agreement of the amplitude pattern is found, while the phase pattern coincides only gradually. Since the wave is ducted to the plasma center in the simulation, while it is ducted to a position slightly off axis in the experiment the differences are possibly due to a plasma inhomogeneity unaccounted for in the simulation. Due to the similarity of the amplitude patterns and the gradual anti-symmetry in the phase pattern of the measurement in domain I, excitation of a mode which has at least an important contribution from the $m = 2$ mode is concluded. Thus, over a wide parameter range whistler modes close to an $m = 2$ are excited by a loop antenna in the experimental setup used in the experiments. During its axial evolution the mode is modified, due to collisions and plasma inhomogeneities. This explains the oscillations found in the amplitude shown in figure 6.3 which are a consequence of the mode structure and the influence of perturbations on the ideal plasma profile shape.
In chapter 4.2.1 an analysis of simulations shows that there is a leakage of wave energy in the radial direction, though the leakage does not dominate the energy flow. The energy of the wave at a certain axial position z inside the plasma radius, for the measurements presented in figures 6.10 - 6.12, is approximated through an addition of the squared amplitude B_x^2 along the x-direction. The axial evolution of this measure for the energy inside the plasma radius gives a qualitative estimate for the leakage of energy from the duct. This is accomplished for the measurement presented in figure 6.10 in figure 6.13 (a), the measurement presented in figure 6.11 in figure 6.13 (b) and the measurement presented in figure 6.12 in figure 6.13 (c). Since the plasma in those measurements is collisionless and kinetic effects are negligible the decrease in the curves must be mainly due to a leakage of energy from the duct. In the cases depicted the leakage is largest close to the antenna. A comparatively small decrease is found at larger distances. The oscillations in figure 6.13 (b) show that energy is leaks from the plasma radius and returns back into the plasma radius. This is due to reflections at the chamber

wall in the radial direction, which explains the pronounced long scale oscillations in the experiment and the simulation in figure 6.11. Since the axial position of the wave exciter inside the vacuum chamber in the experiment and the simulation differs, also the influence of the reflections at the wall on the amplitude evolution inside the plasma radius differs. The difference in the amplitude pattern of the experiment and the simulation is attributed to this effect and not to a difference in the mode structure.
In conclusion the analysis of the wave field via 2D measurements and 3D simulations revealed the mode structure of the excited wave. In flat profiles an agreement of the parallel wave number with the one predicted by the plane wave dispersion relation is found, though an $m = 2$ mode is excited dominantly. Furthermore, the parallel phase velocity and consequently the parallel wavelength is constant over the plasma radius. Leaving the question whether the method proposed in chapter 6.1.1 for the extraction of the waves damping length describes damping due to leakage or due to an energy transfer from the wave to the plasma.
Since the amplitude of the wave along the plasma center does not show any damping and the energy possesses a decrease, the energy ducted in the plasma radius must be focused to the plasma center. Thus, if a damping due to an energy loss of the wave to the plasma is present it will be reflected by a decrease in the damping length of the amplitude curves envelope along the plasma center. This property is used in investigations on the damping of the excited mode.

6.3.1 Cyclotron Damping of Loop Antenna Excited Whistler Waves

The mode structure of the whistler waves excited in the experiments using flat density profiles is identified as having at least an important contribution of an $m = 2$ mode. A good agreement with predictions from plasma dispersion theory is found for the parallel wave and damping length extracted along the central axis of the plasma, as described in chapter 6.1.1. Even more, the phase velocity parallel to the ambient magnetic field is, to a good approximation, constant inside the plasma radius. An open issue is the frequency and parameter dependency of kinetic effects in the excited mode's damping. This is investigated in the following. Since whistler waves are circular polarized they are subject to cyclotron damping. The measurements presented in figure 6.5 indicate cyclotron damping of the excited mode for frequencies larger than $\omega_{ce}/2$. The parameter dependency of the damping is investigated in order to clarify the nature of the damping. Therefore, dispersion measurements are performed for three different combinations of the parameter γ, β and ν along the central axis of the plasma. The experimental results are presented in figure 6.14, where each column represents a specific parameter combination. For each parameter set, the spatial damping decrement k_i and the real part of the wave vector k_r is measured. The result for k_i is shown in the first row of figure 6.14. In the second row the result for k_r is depicted and in the third row the result for the phase velocity v_{ph}. All curves are plotted over frequency and all axes are normalized as pointed out in chapter 2.3. Moreover, the predictions from the hot

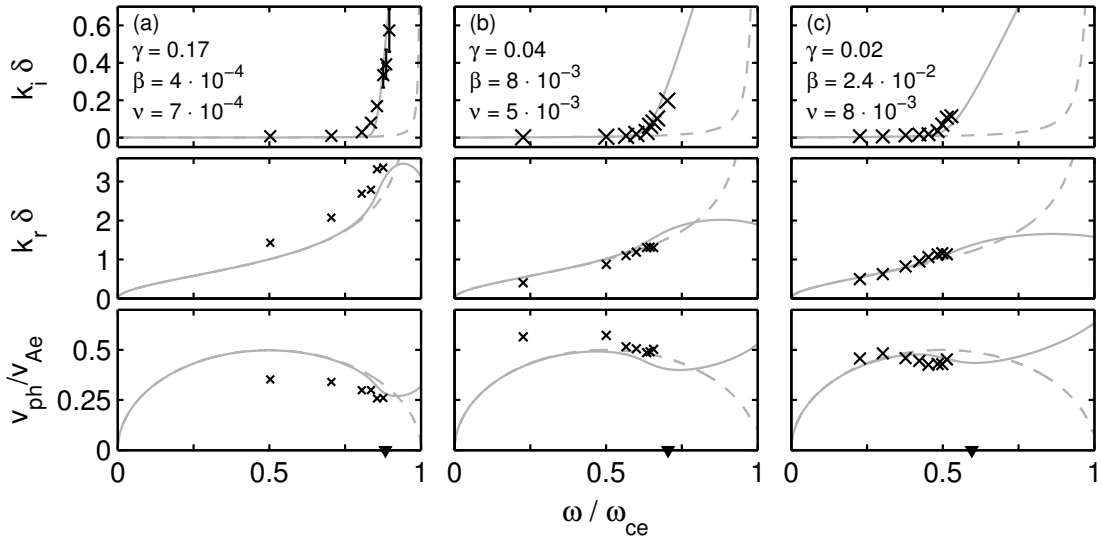

Figure 6.14: Comparison of dispersion measurements with predictions from the hot (full lines) and cold (dashed lines) plasma dispersion relation for three different parameter combinations. The critical frequency as predicted by the hot plasma dispersion relation is marked by a triangle on the frequency axis for each parameter set. Error bars are plotted only if larger than the corresponding markers.

plasma dispersion relation are plotted as full lines and the ones from the cold plasma dispersion relation as dashed lines. The onset of strong damping, depends on β and shifts to lower frequencies if the electron plasma-β is increased from $4 \cdot 10^{-4}$ to $2.4 \cdot 10^{-2}$. Although the loop antenna does not excite plane waves an excellent agreement between theory and experiment has been found for the spatial damping decrement k_i versus ω. As depicted collisional damping can not explain the onset of strong damping. At low frequencies deviations of k_r and v_{ph} from the prediction of dispersion theory is found. Those are due to the wave length of the whistler wave which is in this case larger as the plasma diameter [88]. Figure

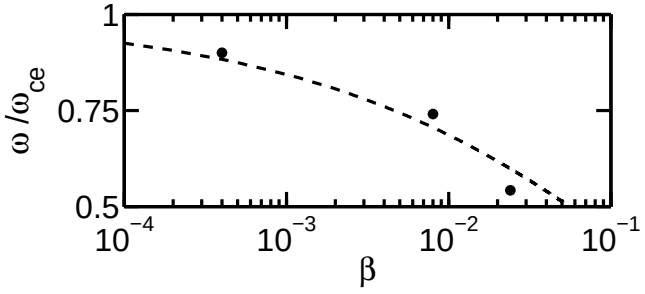

Figure 6.15: Critical frequency for the onset of strong damping (wave length equals damping length) together with the data points obtained from the measurements presented in figure 6.14 over the electron plasma-β.

6.15 depicts the critical frequency for transition from weak to strong damping

over the electron plasma-β as predicted by the hot plasma dispersion relation. Furthermore, the experimental results for the critical frequency taken from the measurements presented in figure 6.14 are shown. Since no data point is exactly at the critical frequency an interpolation of the experimental results is performed. The results show a maximum deviation of 10 % from the prediction at the largest β value. As depicted in figure 6.14 above the critical frequency detection of the wave damping is not possible. Since the loop antenna used in the experiments is an extended instead of a point source, this is supposedly due to the dominant excitation of a wave differing from the whistler mode at strong damping [68].

6.4 Axial Magnetic Field Gradient

In the experiments presented in chapter 6.3.1 dispersion measurements are presented. The whistler wave is excited at several frequencies in order to perform measurements of the frequency dependency of the spatial damping increment at constant plasma parameters. Such measurements are performed at different plasma parameters in order to identify the dominant damping mechanism of the excited mode. Alternatively a whistler wave can be excited at a single frequency and the parameters are varied while the wave propagates forward in order to measure the parameter dependency of whistler wave damping at a fixed frequency. Therefore, an ambient magnetic field configuration with a negative axial gradient is arranged. The gradient causes a plasma parameter variation in the axial direction. Depending on the specific configuration cyclotron damping predicted by the plane wave dispersion relation is negligible in the region of wave excitation, while it is strong further away from the exciter. In order to determine the effect of the negative axial ambient magnetic field gradient on whistler wave propagation, a first experiment is carried out for plasma parameters at which the damping predicted by dispersion theory is weak along the entire axial length of the configuration. A divergence of wave energy [104] along the field lines is predicted for such gradients. The ambient magnetic field is depicted in figure 6.16 (a) in which the field lines are shown together with a color coded plot of the fields absolute value. The extend of the gradient region is of comparable size to the parallel wave length predicted by the plane wave dispersion relation in the region of high magnetic field. Far away from the gradient the ambient magnetic field is homogeneous. The ambient magnetic field is decreased from a value of 31 mT to a value of 15 mT. Thus, the field is decreased by 48 %, where the center of the ambient field gradient is situated at $z = 0.629$ m. As shown in figure 6.16 (b) the plasma radius increases with increasing axial position due to the diverging field lines. A maximum in the plasma density is found in the plasma center in the center of the gradient. Figure 6.16 (c) shows the axial evolution of the wave field, where the wave is excited at $z = 0$ m. A pattern similar to the one found in the experiment presented in figure 6.10 is found. Features like a divergence of the field pattern are completely absent. Plasma parameters, spatial resolution of the measurements as

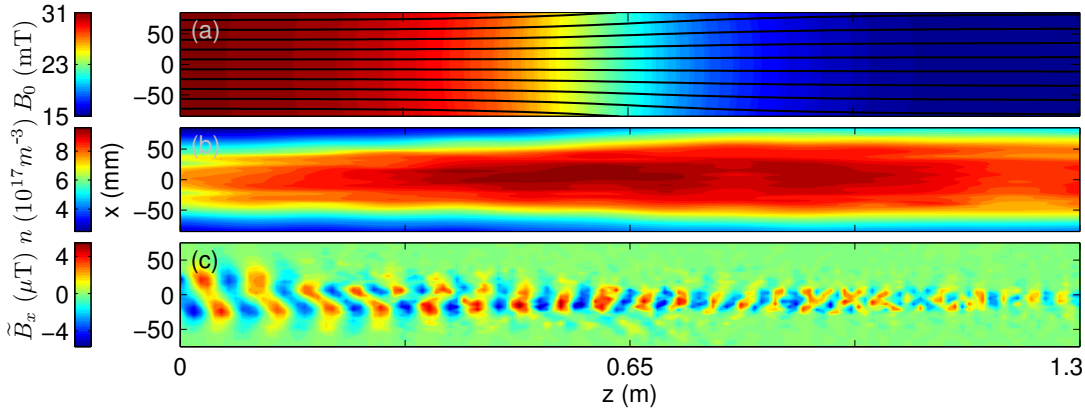

Experimental Parameters		Plasma Center	
$\gamma = 0.1\text{-}0.054$	$B_0 = (31\text{-}15)$ mT	$\delta k_r = 0.5\text{-}0.814$	$\lambda_{\|\|} = (7.7\text{-}4.3)\text{cm} \pm (1.3\text{-}3.6)\%$
$\beta = (1-3.4)\cdot 10^{-3}$	$n = (9.1\text{-}7.5)\cdot 10^{17} m^{-3}$	$\delta k_i = 0.002$	$\tau_{\|\|} = 3.3m \pm 20\%$
$\nu = (1-2.7)\cdot 10^{-3}$	$T = (3\text{-}2.5)$eV	Prediction Dispersion Relation	
$x = 0.23\text{-}0.48$	$f = 200MHz$	$\delta k_r = 0.55\text{-}0.96$	$\lambda_{\|\|} = (6.38\text{-}4)$cm
Resolution (b) : $\Delta x = 6mm$ $\Delta z = 100mm$		$\delta k_i = (5-25)\cdot 10^{-4}$	$\tau_{\|\|} = (12.14\text{-}2.44)$m
Resolution (c) : $\Delta x = 4mm$ $\Delta z = 10mm$			

Figure 6.16: (a) Ambient magnetic field exhibiting an axial gradient, (b) plasma density profile and (c) wave field in this ambient field.

well as wave and damping lengths are indicated in the figure. Thus, the wave length in the plasma center decreases as predicted by the dispersion relation. A result expected from the investigations presented above. A clear separation of the damping length into two domains is not possible. Therefore, a damping length describing the damping along the entire z-axis is indicated, which coincides with the damping length predicted for the low field side of the magnetic field gradient. Moreover, the density profile and the wave field are measured in two azimuthal

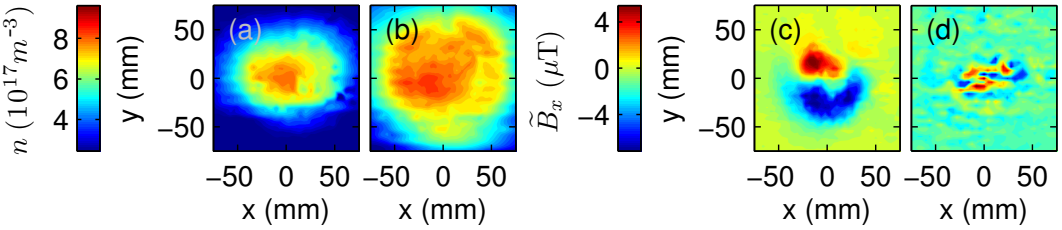

Figure 6.17: Plasma density in an azimuthal plane at (a) $z = 0.065$ m (b) $z = 1.193$ m measured with a resolution of $\Delta x = \Delta y = 6$ mm. Fluctuating magnetic field at (c) $z = 0.065$ m (d) $z = 1.193$ m measured with a resolution of $\Delta x = \Delta y = 4$ mm.

planes. Figure 6.17 shows the density in the plane close to the exciter (a) and further away from the exciter (b). At both distances the plasma density is not circular. Instead an elliptic shape is found close to the exciter and a perturbed ellipsis far from the antenna. The region of plasma density homogeneity close

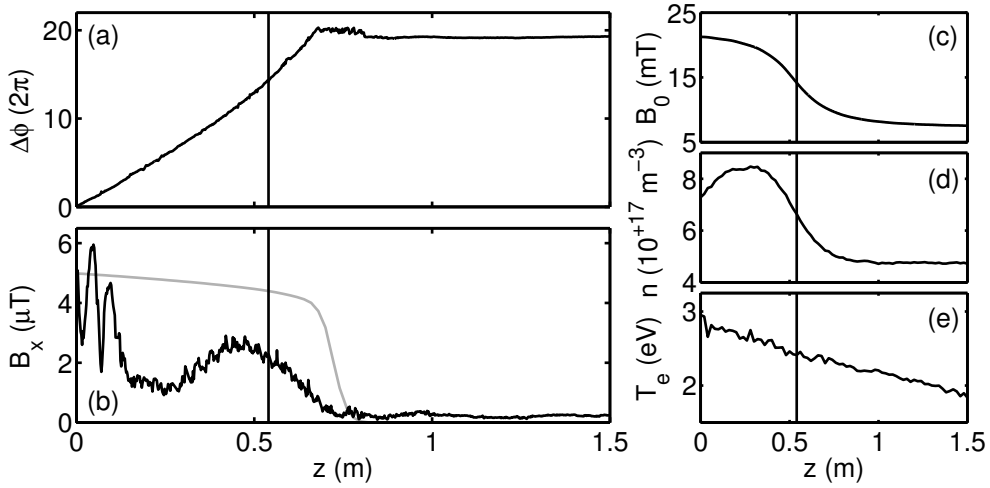

Figure 6.18: Whistler wave propagation in a magnetic field gradient with weak damping in the high field ($B_0 = 23.7$ mT) region and strong damping in the low field ($B_0 = 7.9$ mT) region. The wave field is measured with a spatial resolution of $\Delta z = 2$ mm. A vertical line marks the position in the center of the ambient field gradient.

to the antenna is smaller than in inductive discharges in homogeneous ambient magnetic fields. In turn it is larger far away from the antenna. The wave field close to the exciter is depicted in figure 6.17 (c) while the one far from the exciter is depicted in figure 6.17 (d). Close to the exciter the wave field in the azimuthal plane is given by two regions with opposite polarity as found in the case of inductive discharges in homogeneous ambient magnetic fields. The wave field far away from the antenna has an even more complex structure and a much smaller diameter. Thus, the mode structure close to the antenna differs from the one far from the antenna in diameter and mode number.

6.4.1 Cyclotron Damping in a Magnetic Field Gradient

Figure 6.18 (c) depicts the ambient magnetic field along the symmetry axis of the plasma chosen for the investigation on cyclotron damping. This gradient causes an axial dependency of the plasma density and temperature as depicted in figure 6.18 (d) and (e). Wave propagation in such a magnetic field gradient is discussed in chapter 6.4 for the case of weak damping. Geometric damping as a possible source of strong wave damping was ruled out. In the experiment depicted in figure 6.18 parameters are chosen at which cyclotron damping is negligible in the high field region but strong in the low field region. The electron plasma-β undergoes a change from $\beta = 2 \cdot 10^{-3}$ in the high field region to a value of $\beta = 6 \cdot 10^{-3}$ in the low field region. Moreover, the cyclotron resonance frequency lowers about a factor of three from $f = 662$ MHz to $f = 221$ MHz. Since the wave is excited at $f = 200$ MHz it is very close to the resonance frequency after the gradient is

passed. The axial dependency of the waves phase is depicted in figure 6.18 (a) the phase evolution is given by two characteristic regions. In the axial region for $z < 0.67$ m the phase velocity is relatively small, but becomes large with increasing distance. This indicates a vanishing of the whistler mode wave, instead a cavity mode appears. According to the findings in chapter 6.1 the whistler mode wave is damped away for distances larger than $z = 0.67$ m. This is supported by the amplitude evolution along the symmetry axis depicted in figure 6.18 (b). The wave amplitude shows oscillations in the region of weak damping and vanishes after it propagated through the ambient field gradient. A prediction for the damping of a plane whistler mode wave propagating through this configuration is depicted as a gray line. Since an arbitrary initial value for the prediction is chosen the absolute value of the prediction can not be compared with the experiment. However, the distance at which the prediction exhibits a negligible amplitude can be compared with the one found in the experiment. In this aspect the results agree with an accuracy of 10 %.

7 Summary and Conclusion

Within the scope of this thesis loop antenna excited waves in the whistler wave range of frequencies in a magnetized cylindrical plasma are investigated. Since the plasma has a diameter of 10 cm and the loop antenna a diameter of 4.5 cm the plasma inhomogeneity has an effect on wave propagation. In the experiments an $m = 2$ azimuthal mode with a single amplitude maximum in the radial direction is observed close to the wave exciter. The propagation of the excited mode is investigated for plasma parameters under which the parallel wave length is in the order of the plasma diameter or smaller. A comparison between three different plasma density profiles reveals a crucial influence of plasma density inhomogeneities on the propagation of the excited mode. In hollow profiles ducting of the wave in the peaks around the central axis of the plasma profile is possible, while profiles peaked in the plasma center posses a strong radial variation in the parallel phase velocity. A comparatively simple propagation pattern is found in flat profiles for which the parallel phase velocity within the plasma radius is approximately constant and wave energy is ducted to the plasma center. The mode is identified by a comparison of 2D measurements of the fluctuating magnetic field $\widetilde{B}_x$ in azimuthal and radial axial planes and 3D full-wave simulations. Based on the agreement of the simulations with the experiments close to the wave exciter predictions on the excited modes properties are carried out. In the simulations the fluctuating space charge is identified as the source for the electric field and the inductive contribution is found to be negligible in agreement with alternative approaches [40]. Furthermore, an important contribution of the displacement current to the fluctuating magnetic field is found, which is in the same magnitude of order as the contribution from the electron current. In accordance with the simulations the parallel wave length in the experiments is found to agree with predictions of the plane wave dispersion relation, though a mode differing substantially from a plane wave is excited. In contrast to the parallel wave length in the plasma center, the amplitude run along the center does not agree with the prediction of dispersion theory. An exponential decay is predicted by dispersion theory, while oscillations are observed. Those are due to the mode structure. Since the leakage from the plasma and the focusing towards the plasma center due to wave ducting balance each other the damping length of the oscillations envelope is a good approximation for the damping of the wave due to an energy loss to the plasma. Therefore, it is possible to explore the damping of the mode by 1D measurements along the symmetry axis of the plasma. The parameter dependency of the waves spatial damping increment is found to agree with predictions from kinetic dispersion theory for cyclotron damping, where parameters are chosen for which damping due

to collisions is negligible.
Cyclotron damping is an effect due to a Doppler shift of the waves frequency in the frame co-moving with the electrons in the plasma. The Doppler shift depends only on the parallel phase velocity. Since the parallel phase velocity of the excited mode coincides with the one predicted by the plane wave dispersion relation, also the spatial damping increment agrees. Prior investigations on this topic are carried out based exclusively on 1D measurements of the fluctuating magnetic field perpendicular to the ambient magnetic field $\widetilde{B}_x$, assuming propagation of plane waves [53, 54, 55]. The interpretation of this experiment type is criticized since its first appearance, because propagation of plane waves in such an arrangement is impossible [56, 34, 57, 58]. The results presented within this thesis show that indeed a $m = 2$ azimuthal mode instead of a plane wave is excited, though in the parameter range pointed out 1D measurements and predictions from plane wave dispersion theory suffice to give a good estimation on the spatial damping increment of the excited mode. However, in the general case three dimensional measurements of the wave field in all of the three spatial directions are necessary in order to achieve an exact result on the propagation and the damping of whistler waves [36]. Measurements in one and two dimension can only be used in certain limits or to a certain approximation.
Besides the characterization of the mode excited by the loop antenna, full-wave simulations are found to be a useful tool for the prediction of the excited mode. Although the mode observed in the experiment and predicted by the simulation is known from alternative predictions by dispersion theory [31, 33, 87] some important features are not predicted by dispersion theory. The properties of the loop antenna lead to a broad spectrum of parallel and perpendicular wave numbers, a feature not present in the predictions of dispersion theory. Furthermore, dispersion theory predicts an infinite number of possible modes in a cylindrical plasma, which mode is excited in particular is not predicted. The simulation includes both, the broad spectrum and the excitation of a particular mode. Therefore, such simulations are an essential tool for predictions on experiments. Even the design of experiments can be supported by them.

8 Outlook

The investigations carried out during the preparation of this thesis can be understood as a recommendation for three dimensional measurements of the wave field in all of the three spatial directions [105, 106, 107]. In addition, also the density should be measured in three dimensions and in the case of helicon sources time dependent measurements are necessary [108] in order to clarify whether the plasma density possesses spatial or time dependent inhomogeneities [109]. Those inhomogeneities are supposed to be due to the helicon plasma source, which generates the plasma at least partially by launching an $m = 1$ helicon mode [110]. An inhomogeneity following the $m = 1$ helicon mode could cause the difference between experiments and simulations as observed in the measurements of the fluctuating magnetic field discussed in chapter 6.3. From such measurements a more complete picture of wave propagation would arise which avoids miss interpretations and allows for investigations on whistler wave damping cyclotron damping which are not limited to special cases [36, 111]. Predictions on wave propagation are recommended in the frame work of models including the plasma inhomogeneity and the source of the excited wave. Furthermore, kinetic effects like cyclotron damping and heating of the plasma by collisional damping should be included in the predictions. This could be achieved by a further development of the simulations used within this thesis.

List of Symbols

α	angle between phase and group velocity	chapter 2.2.2
β	electron plasma beta	chapter 2.1
γ	plasma parameter	chapter 2.1
γ_{max}	characterizes the transversal polarizations	chapter 2.2
δ	collisionless skin depth	chapter 2.1
Δ	grid cell size in full-wave simulations	chapter 4.2
$\Delta\phi$	phase difference	chapter 3.1
$\Delta\phi_{B_x,B_y}$	average phase shift between B_x and B_y	chapter 6.1.1
ϵ_s	sign of the particle species s electric charge	chapter 2.2
ϵ_0	vacuum permittivity	chapter 2.1
ζ_{ms}	argument of the plasma dispersion function	chapter 2.3
θ	polar angle and propagation direction	chapter 2.1
θ_{cut}	angle cut-off at which the cut-off occurs	chapter 2.1
θ_{res}	resonance cone angle	chapter 2.1
ι	propagation angle normalized to θ_{res}	chapter 2.1
κ	density decrease between sheath edge and probe	chapter 5.2.1
λ	wave length	chapter 2.2.1
λ_{pl}	wave length in a plasma	chapter 5.2.2
λ_0	vacuum wave length	chapter 5.2.2
μ_0	vacuum permeability	chapter 2.1
ν	ν_{eff} normalized to ω_{ce}	chapter 2.1
ν_{eff}	effective collision frequency	chapter 2.1
ν_{ei}	electron-ion collision frequency	chapter 2.1
ν_{en}	electron-neutral collision frequency	chapter 2.1
$\rho_e = v_{th}/\omega_{ce}$	gyro radius of the electron	chapter 5
ρ_{sc}	space charge density	chapter 2.1
$\widetilde{\rho}_{sc}$	fluctuating space charge density	chapter 4.2.3
σ	full width at half mean in Gaussian profile	chapter 4.2
$\underline{\sigma}$	conductivity tensor	chapter 2.1
Σ_x	sum over the x-component	chapter 6.3
τ	damping length	chapter 2.2.1

Table 1: Greek symbols α - τ.

ϕ	phase	chapter 3.1
ϕ_{fl}	floating potential	chapter 5.2.1
ϕ_{in}	instantaneous phase	chapter 3.2
ϕ_{pl}	plasma potential	chapter 5.2.1
ϕ_r	phase of reference signal	chapter 3.1
ϕ_w	phase of measured signal	chapter 3.1
φ	azimuthal angle	chapter 4.2.3
$\varphi_{E_{xy},H_{xy}}$	angle between E_{xy} and H_{xy}	chapter 4.2.3
χ	frequency normalized to ω_{ce}	chapter 2.1
ψ	wave vector normalized to ω_{ce}	chapter 2.1
ω	angular frequency	chapter 2.1
$\omega_{ce} = eB_0/m_e$	electron cyclotron frequency	chapter 2.1
$\omega_{ci} = eB_0/m_i$	ion cyclotron frequency	chapter 5
ω_{crit}	critical frequency	chapter 2.2.1
ω_L	L-wave cut-off frequency	chapter 2.2
$\omega_{pe} = (ne2/(\epsilon_0 m_e))^{1/2}$	electron plasma frequency	chapter 2.1
ω_R	R-wave cut-off frequency	chapter 2.2
ω_{res}	resonance frequency	chapter 2.2

Table 2: Greek symbols ϕ - ω.

A	area	chapter 5.2.1
A_{in}	instantaneous amplitude	chapter 3.2
$\mathbf{B}$	magnetic induction field	chapter 2.1
$\dot{\mathbf{B}}$	time derivative of the magnetic field	chapter 5.3
$\widetilde{\mathbf{B}}$	fluctuating magnetic field	chapter 2.1
$\mathbf{B}_0$	ambient magnetic field	chapter 2.1
c	speed of light in vacuum	chapter 2.1
$c_s = (T_e/m_i)^{1/2}$	ion sound speed	chapter 5.2.2
$\mathbf{D}$	electric displacement	chapter 2.1
D	dielectric tensor element Stix notation	chapter 2.1
D_r	relative difference	chapter 2.2.2
e	charge of the electron	chapter 5.2.1
$\mathbf{e}_z$	unit vector in z-direction	chapter 4.2
$\mathbf{e}_\mathbf{k}$	unit vector in $\mathbf{k}$-direction	chapter 2.2.2
$\mathbf{e}_\theta$	unit vector in θ-direction	chapter 2.2.2
$\mathbf{E}$	electric field	chapter 2.1
$\mathbf{E}_{es}$	electro static field	chapter 3.3
$\mathbf{E}_{ind}$	inductive electric field	chapter 3.3
$\widetilde{\mathbf{E}}$	fluctuating electric field	chapter 4.2.3

Table 3: Roman symbols A - E.

f	frequency	chapter 5
f_e	electron velocity distribution function	chapter 5.2.1
$f_{e,z}$	f_e parallel to B_0	chapter 5.2.1
$f_r(t)$	reference time series	chapter 3.1
f_s	velocity distribution of particle species s	chapter 2.3
$f_w(t)$	measured time series	chapter 3.1
$f(x)$	real valued signal	chapter 3.2
$f_a(x)$	analytical signal	chapter 3.2
$f_{0,s}$	distribution of the background plasma	chapter 2.3
$f_1(t)$	arbitrary time series	chapter 3.1
$f_2(t)$	arbitrary time series	chapter 3.1
$\mathcal{F}$	Fourier transform operator	chapter 3.1
$g(x)$	Hilbert transformed signal	chapter 3.2
$\mathbf{H}$	magnetic field	chapter 4.2
$\widetilde{\mathbf{H}}$	fluctuating magnetic field	chapter 4.2.3
$\widetilde{H}_{x,J,in}$	$\widetilde{H}_x$ due to J	chapter 4.2.5
$\widetilde{H}_{x,J_{dis},in}$	$\widetilde{H}_x$ due to J_{dis}	chapter 4.2.5
$\widetilde{H}_{x,J_{xy},in}$	$\widetilde{H}_x$ due to J_{xy}	chapter 4.2.5
$\widetilde{H}_{x,J_z,in}$	$\widetilde{H}_x$ due to J_z	chapter 4.2.5
$\mathcal{H}$	Hilbert transform operator	chapter 3.2
i	$\sqrt{i}$	chapter 2.1
I	current	chapter 5.2.1
$I_{i,sat}$	ion saturation current	chapter 5.2.1
$\mathbf{J}$	electron current density	chapter 2.1
$\mathbf{J}_{dis}$	displacement current density	chapter 4.2.5
$\widetilde{\mathbf{J}}$	fluctuating electron current density	chapter 4.2.3
$\mathbf{k}$	wave vector	chapter 2.1
k	absolute value of the wave vector	chapter 2.1
k_B	Boltzmann constant	chapter 2.1
k_i	imaginary part of the wave vector	chapter 2.2.1
k_r	real part of the wave vector	chapter 2.2.1
$\underline{K}$	dielectric tensor	chapter 2.1
K_1, K_2, K_3	elements of the dielectric tensor	chapter 2.1
l	length	chapter 5.2.2
l_p	probe length	chapter 5.2.1
L	Stix parameter	chapter 2.1
m	integer number	chapter 2.3
m_e	electron mass	chapter 2.2
m_i	ion mass	chapter 2.2
m_s	particle species mass	chapter 2.3

Table 4: Roman symbols F - M.

n	electron particle density	chapter 2.1
n_{cut}	cut-off density	chapter 5.2.2
ndl	line integrated density	chapter 5.2.2
n_s	species s particle density	chapter 2.1
$\mathbf{N}$	index of refraction vector	chapter 2.1
N	index of refraction absolute value	chapter 2.1
$\mathbf{N}_L$	index of refraction for L-waves	chapter 2.2
$\mathbf{N}_R$	index of refraction for R-waves	chapter 2.2
p_{Ar}	argon neutral gas pressure	chapter 5
p_{mag}	magnetic pressure	chapter 2.1
p_{plasma}	kinetic plasma pressure	chapter 2.1
P	dielectric tensor element Stix notation	chapter 2.1
P_m	point in space	chapter 4.1
$\mathcal{P}$	polarization operator	chapter 2.1
$\mathcal{P}_\times$	cross-power spectral density operator	chapter 3.1
q_s	electric charge	chapter 2.1
r	radius	chapter 4.2.1
r_p	probe radius	chapter 5.2.1
r_{src}	radius of the loop exciter	chapter 4.2
$\mathbf{R}$	ray direction	chapter 4.1
R	Stix parameter	chapter 2.1
R_S	shunt resistor	chapter 5.2.1
s	index denoting a particle species	chapter 2.1
S	dielectric tensor element Stix notation	chapter 2.1
SNR	signal to noise ratio	chapter 6.1
t	time	chapter 2.1
T	period of an oscillation	chapter 4.2
T_e	electron temperature	chapter 2.1
$U = 0.5\,(\epsilon_0\mathbf{E}^2 + \mathbf{B}^2/\mu_0)$	energy density	chapter 4.2.1
v_{Ae}	electron Alfvén velocity	chapter 2.2
v_{cr}	cyclotron resonance velocity	chapter 2.3
v_{gr}	group velocity	chapter 2.2.2
v_{ph}	phase velocity	chapter 2.1
$\mathbf{v}_s$	particle species velocity	chapter 2.1
v_{th}	thermal velocity of electrons	chapter 2.3
$v_{th,s}$	thermal velocity of species s	chapter 2.3
V	voltage	chapter 5.2.1
$VSWR$	voltage standing wave ratio	chapter 5.3.2
Z_{ns}	dispersion function	chapter 2.3
(x, y, z)	Cartesian coordinates $\mathbf{B}_0 \| \mathbf{e}_z$	chapter 2.1

Table 5: Roman symbols N - Z.

List of Figures

List of Tables

Bibliography

[1] W. H. Preece. Earth currents. *Lett., Nat. London*, 49:554, 1894.

[2] H. Barkhausen. Zwei mit Hilfe der neuen Verstärker entdeckte Erscheinungen. *Phys. Zeitschr.*, 20(71):401–403, 1919.

[3] E. V. Appleton and M. Barnett. Local reflection of wireless waves from the upper atmosphere. *Nature*, 115:333–334, 1925.

[4] E. V. Appleton. Diurnal variation of ultra-short-wave transmission. *Proc. Cambridge Philos. Soc.*, 23:155–161, 1926.

[5] D. Hartree. The propagation of electromagnetic waves in a refracting medium in a magnetic field. *Proc. Cambridge Philos. Soc.*, 27:143–162, 1931.

[6] E.V. Appleton. Wireless studies of the ionosphere. *Proc. Inst. Electr. Eng. : Wirel. Sect.*, 7(21):257 –265, 1932.

[7] H. Barkhausen. Whistling tones from the earth. *Proc. Inst. Radio Eng.*, 18(7):1155–1159, 1930.

[8] T. L. Eckersley. Musical atmospherics. *Suppl. Nat.*, January 19:104–105, 1935.

[9] L. Storey. An investigation of whistling atmospherics. *Philos. Trans. R. Soc. London. Ser. A, Math. and Phys. Sci.*, 246(908):113–141, 1953.

[10] R. A. Helliwell. *Whistlers and Related Ionospheric Phenomena.* Stanford University Press, Stanford, California, USA, 1965.

[11] D. Carpenter. Whistler evidence of a knee in magnetospheric ionization density profile. *J. Geophys. Res.*, 68(6):1675–1682, 1963.

[12] I. B. Bernstein. Waves in a plasma in a magnetic field. *Phys. Rev.*, 109(1):10–21, 1958.

[13] F. Scarf. Landau damping and the attenuation of whistlers. *Phys. Fluids*, 5(1):6–13, 1962.

[14] R. Thorne. Whistler absorption and electron heating near the plasmapause. *J. Geophys. Res.*, 101(A3):4917–4928, 1996.

[15] H. Liemohn and F. Scarf. Whistler determination of electron energy + density distributions in magnetosphere. *J. Geophys. Res.*, 69(5):883–904, 1964.

[16] R. A. Helliwell. Controlled vlf wave injection experiments in the magnetosphere. *Space Sci. Rev.*, 15:781–802, 1974.

[17] M. J. Rycroft. Enhanced energetic electron intensities at 100 km altitude and a whistler propagating through the plasmasphere. *Planet. Space Sci.*, 21(2):239–251, 1973.

[18] D. A. Gurnett, W. S. Kurth, J. T. Steinberg, P. M. Banks, R. I. Bush, and W. J. Raitt. Whistler-mode radiation from the spacelab 2 electron beam. *Geophys. Res. Lett.*, 13(3):225–228, 1986.

[19] D. Carpenter and R. Anderson. An isee/whistler model of equatorial electron-density in the magnetosphere. *J. Geophys. Res.*, 97(A2):1097–1108, 1992.

[20] D. Gurnett, W. Kurth, G. Hospodarsky, A. Persoon, T. Averkamp, and B. Cecconi. Radio and plasma wave observations at saturn from cassini's approach and first orbit. *Science*, 307(5713):1255–1259, 2005.

[21] R. L. Stenzel. Whistler waves in space and laboratory plasmas. *J. Geophys. Res.*, 104(A7):14379–14395, 1999.

[22] R. W. Boswell. Very efficient plasma generation by whistler waves near the lower hybrid frequency. *Plasma Phys. Control. Fusion*, 26(10):1147–1162, 1984.

[23] R. W. Boswell and F. F. Chen. Helicons: The early years. *IEEE T. Plasma. Sci.*, 25(6):1229–1244, 1997.

[24] B. Chakraborty, G. C. Das, A. K. Sur, and S. N. Paul. Nonlinear propagation of whistlers in the ionosphere. *Astrophys. Space Sci.*, 123:259–271, 1986.

[25] P. Palmadesso and G. Schmidt. Collisionless damping of a large amplitude whistler wave. *Phys. Fluids*, 14(7):1411–1418, 1971.

[26] K. Sauer. Wave emission by whistler oscillitons: Application to coherent lion roars. *Geophys. Res. Lett.*, 29(24):2226(4), 2002.

[27] T. Cattaert and F. Verheest. Large amplitude parallel propagating electromagnetic oscillitons. *Phys. Plasmas*, 12(1):12307(7), 2005.

[28] R. L. Stenzel, J. Urrutia, and K. Strohmaier. Whistler modes with wave magnetic fields exceeding the ambient field. *Phys. Rev. Lett.*, 96(9):95004(4), 2006.

[29] R. L. Stenzel, J. Urrutia, and K. Strohmaier. Whistler instability in an electron-magnetohydrodynamic spheromak. *Phys. Rev. Lett.*, 99(26):265005(4), 2007.

[30] R. Gallet, J. Richardson, B. Wieder, G. Ward, and G. Harding. Microwave whistler mode propagation in a dense laboratory plasma. *Phys. Rev. Lett.*, 4(7):347–349, 1960.

[31] B. Wieder. Microwave propagation in an overdense bounded magnetoplasma. *Phys. Fluids*, 7(7):964–972, 1964.

[32] P. Hedvall and L. Sjorgen. Influence of collisions on whistler propagation. *Electron. Lett.*, 1(3):54–55, 1965.

[33] D. Baker and T. Hall. Direct measurement of propagation of whistler wave packets. *Plasma Phys.*, 16(10):901–907, 1974.

[34] R. L. Stenzel. Whistler wave propagation in a large magnetoplasma. *Phys. Fluids*, 19(6):857–864, 1976.

[35] R. L. Stenzel. Antenna radiation-patterns in whistler wave regime measured in a large laboratory plasma. *Radio Sci.*, 11(12):1045–1056, 1976.

[36] R. L. Stenzel, J. M. Urrutia, and C. L. Rousculp. Pulsed currents carried by whistlers. Part I: Excitation by magnetic antennas. *Phys. Fluids B*, 5(2):325–338, 1993.

[37] J. Urrutia, R. L. Stenzel, and C. Rousculp. Pulsed currents carried by whistlers. Part II: Excitation by biased electrodes. *Phys. Plasmas*, 1(5):1432–1438, 1994.

[38] J. Urrutia, R. L. Stenzel, and C. Rousculp. Pulsed currents carried by whistlers. Part III: Magnetic-fields and currents excited by an electrode. *Phys. Plasmas*, 2(4):1100–1113, 1995.

[39] R. L. Stenzel, J. Urrutia, and C. Rousculp. Pulsed currents carried by whistlers. Part IV: Electric-fields and radiation excited by an electrode. *Phys. Plasmas*, 2(4):1114–1128, 1995.

[40] C. Rousculp, R. Stenzel, and J. Urrutia. Pulsed currents carried by whistlers. Part V: Detailed new results of magnetic antenna excitation. *Phys. Plasmas*, 2(11):4083–4093, 1995.

[41] H. Sugai. Whistler wave ducting caused by antenna actions. *Phys. Fluids*, 21(4):690–694, 1978.

[42] R. Smith and J. Angerami. Magnetospheric properties deduced from ogo 1 observations of ducted and nonducted whistlers. *J. Geophys. Res.*, 73(1):1–20, 1968.

[43] R. L. Smith. Propagation characteristics of whistlers trapped in field-aligned columns of enhanced ionization. *J. Geophys. Res.*, 66:3699–3707, 1961.

[44] J. J. Angerami. Whistler duct properties deduced from vlf observations made with ogo-3 satellite near magnetic equator. *J. Geophys. Res.*, 75(31):6115–6135, 1970.

[45] I.G. Kondrat'ev, A.V. Kudrin, and T.M. Zaboronkova. *Electrodynamics of density ducts in magnetized plasmas*. Gordon & Breach, 1999.

[46] H. Sugai. Whistler wave trapping in a narrow density trough. *J. Phys. Soc. Jpn.*, 46(5):1647–1652, 1979.

[47] H. Sugai. Whistler wave-trapping in a density crest. *Phys. Fluids*, 23(10):2134–2139, 1980.

[48] A. Kostrov, A. Kudrin, L. Kurina, G. Luchinin, A. Shaykin, and T. Zaboronkova. Whistlers in thermally generated ducts with enhanced plasma density: Excitation and propagation. *Phys. Scr. T*, 62(1):51–65, 2000.

[49] D. Pasmanik and V. Trakhtengerts. Dispersion properties of ducted whistlers, generated by lightning discharge. *Ann. Geophysicae*, 23(4):1433–1439, 2005.

[50] C. Lechte. Investigation of the scattering efficiency in doppler reflectometry by two-dimensional full-wave simulations. *IEEE Trans. Plasma Sci.*, 37(6):1099–1103, 2009.

[51] A. Streltsov, M. Lampe, W. Manheimer, G. Ganguli, and G. Joyce. Whistler propagation in inhomogeneous plasma. *J. Geophys. Res.*, 111(A3):A03216(10), 2006.

[52] A. Streltsov. Spectral properties of high-density ducts. *J. Geophys. Res.*, 112(A12):A12218(10), 2007.

[53] G. Lisitano and S. Bernabei. Propagation of electron cyclotron waves along a magnetic beach. *Phys. Rev. Lett.*, 26(13):747–751, 1971.

[54] C. Christopoulus, R. W. Boswell, and P. J. Christiansen. Measurements of spatial cyclotron damping in a uniform magnetic field. *Phys. Lett. A*, 47(3):239–240, 1974.

[55] K. Ohkubo and S. Tanaka. Spatial cyclotron damping of whistler waves in plasmas .2. *J. Phys. Soc. Jpn.*, 41(1):254–256, 1976.

[56] B. D. McVey and J. E. Scharer. Measurement of collisionless electron-cyclotron damping along a weak magnetic beach. *Phys. Rev. Lett.*, 31(1):14–17, 1973.

[57] B. D. McVey and J. E. Scharer. Comments on whistler wave propagation in a large magnetoplasma. *Phys. Fluids*, 20(11):1960–1961, 1977.

[58] R. L. Stenzel. Reply to comments on whistler wave propagation in a large magnetoplasma. *Phys. Fluids*, 20(11):1961–1962, 1977.

[59] D. G. Swanson. *Plasma Waves*. Academic Press, San Diego, CA, USA, 1989.

[60] T. H. Stix. *Waves in Plasmas*. AIP, New York, USA, 1992.

[61] P. L. Bhatnagar, E. P. Gross, and M. Krook. A model for collision processes in gases. I. small amplitude processes in charged and neutral one-component systems. *Phys. Rev.*, 94(3):511–525, 1954.

[62] E. P. Gross and M. Krook. Model for collision processes in gases - small-amplitude oscillations of charged 2-component systems. *Phys. Rev.*, 102(3):593–604, 1956.

[63] H. G. Booker. The application of the magneto-ionic theory to the ionosphere. *Proc. R. Sci. London Ser. A: Math. Phys. Sci.*, 150(870):267–286, 1935.

[64] H. Poeverlein. Strahlwege von radiowellen in der ionosphaere. *Zeits. Angew. Phys.*, 1(11):517–525, 1949.

[65] B. D. Fried and S. D. Conte. *The Plasma Dispersion Function*. Academic Press, 1961.

[66] C.L. Olson. *Ph.D. Dissertation*. ProQuest, University of California, Los Angeles, USA, 1970.

[67] S. P. Gary. *Theory of Space Plasma Microinstabilities*. Cambridge University Press, Los Alamos National Laboratory, USA, 1993.

[68] C. L. Olson. Spatial electron cyclotron damping. *Phys. Fluids*, 15(1):160–165, 1972.

[69] T. Ypma. Historical development of the newton-raphson method. *SIAM Rev.*, 37(4):531–551, 1995.

[70] J. A. C. Weideman. Computations of the complex error function. *SIAM J. Numer. Anal.*, 31(5):1497–1518, 1994.

[71] G. P. M. Poppe and C. M. J. Wijers. Algorithm 680: evaluation of the complex error function. *ACM Trans. Math. Softw.*, 16(1):47, 1990.

[72] W. Gautschi. Efficient computation of the complex error function. *SIAM J. Numer. Anal.*, 7(1):187–198, 1970.

[73] K. Sauer. Implementation of code for kinetic dispersion relation. *Privat Communication*.

[74] R. F. Lutomirski. Physical model of cyclotron damping. *Phys. Fluids*, 13(1):149–153, 1970.

[75] L. Marple. Computing the discrete-time analytic signal via fft. *IEEE T. Signal. Proces.*, 47(9):2600–2603, 1999.

[76] G. B. Arfken and H. J. Weber. *Mathematical Methods for Physicists International Edition, 6th edition*. Academic Press, San Diego, USA, 2005.

[77] I. Yabroff. Computation of whistler ray paths. *J. Res. Natl. Bureau Standards*, 65D(5):485–505, 1961.

[78] H. Sugai and S. Takeda. Linear amplitude oscillation of a whistler wave excited by high-power microwaves. *Phys. Fluids*, 23(1):194–199, 1980.

[79] R. L. Smith, R. A. Helliwell, and I. W. Yabroff. A theory of trapping of whistlers in field-aligned columns of enhanced ionization. *J. Geophys. Res.*, 65(3):815–823, 1960.

[80] C. Lechte. Computation of the simulations is performed by Dr.C. Lechte. *IPF Stuttgart*, 2010.

[81] K. Yee. Numerical solution of initial boundary value problems involving maxwells equations in isotropic media. *IEEE Trans. Antennas Propag.*, 14(3):302–307, 1966.

[82] S. Gedney. An anisotropic perfectly matched layer-absorbing medium for the truncation of FDTD lattices. *IEEE T. Antenn. Propag.*, 44(12):1630–1639, 1996.

[83] A. Taflove and S. C. Hagnes. *Computational Electrodynamics*. Artech House, Inc., Norwood, Massachusetts, USA, 2005.

[84] C. M. Franck, O. Grulke, and T. Klinger. Magnetic fluctuation probe design and capacitive pickup rejection. *Rev. Sci. Instrum.*, 73(11):3768–3771, 2002.

[85] H. Sugai, M. Sato, K. Ido, and S. Takeda. Dispersion and attenuation of whistler waves in a finite plasma. *J. Phys. Soc. Jpn.*, 44(6):1953–1959, 1978.

[86] T. Wang and T. Bell. Vlf/elf radiation patterns of arbitrarily oriented electric and magnetic dipoles in a cold lossless multicomponent magnetoplasma. *J. Geophys. Res.*, 77(7):1174–1189, 1972.

[87] B. Harvey. The absorption mechanisms of whistler waves in cool, dense, cylindrically bounded plasmas. *Phys. Fluids B*, 5(11):3864–3875, 1993.

[88] C. M. Franck, O. Grulke, and T. Klinger. Transition from unbounded to bounded plasma whistler wave dispersion. *Phys. Plasmas*, 9(8):3254–3258, 2002.

[89] C. M. Franck, O. Grulke, and T. Klinger. Mode transitions in helicon discharges. *Phys. Plasmas*, 10(1):323–325, 2003.

[90] P. J. Mohr and B. N. Taylor. Codata recommended values of the fundamental physical constants: 2002. *Rev. Mod. Phys.*, 77(1):1–107, 2005.

[91] M. A. Lieberman and A. J. Lichtenberg. *Principles of Plasma Discharges and Materials Processing*. John Wiley & SONS, INC., New York, 1994.

[92] H. M. Mott-Smith and I. Langmuir. The theory of collectors in gaseous discharges. *Phys. Rev.*, 28(4):727–763, 1926.

[93] M. Druyvesteyn. Low-voltage arc. *Zeits. Phys.*, 64:781–798, 1930.

[94] T. Geist, E. Wursching, and H. J. Hartfuss. Multichannel millimeter wave interferometer for W7-AS. *Rev. Sci. Instrum.*, 68(2):1162–1167, 1997.

[95] V. I. Demidov, S. V. Ratynskaia, and K. Rypdal. Electric probes for plasmas: The link between theory and instrument. *Rev. Sci. Instrum.*, 73(10):3409–3439, 2002.

[96] I. D. Sudit and R. C. Woods. Theory of electron retardation by langmuir probes in anisotropic plasmas. *Phys. Rev. E*, 50(3):2222–2238, 1994.

[97] I. D. Sudit. Rf compensated probes for high-density discharges. *Plasma Sources Sci. Technol.*, 3(2):162–168, 1994.

[98] I. H. Hutchinson. *Principles of Plasma Diagnostics*. Cambridge Univ.Press, Cambridge, 1987.

[99] O. Waldmann, B. Koch, and G. Fussmann. Langmuir probe measurements in plasma shadows. *Am. Inst. Phys. Conf. Proc.*, 812:443–446, 2006.

[100] A. Piel. *Plasma Physics*. Springer-Verlag, Berlin Heidelberg, GER, 2010.

[101] K. U. Riemann. The bohm criterion and sheath formation. *J. Phys. D*, 24(4):493–518, 1991.

[102] D. Smith. Diffusion cooling in neon, argon, and krypton afterglow plasmas. *Zeits. Phys.*, 253(3):191–199, 1972.

[103] T. Wang. Vlf input impedance of a loop antenna in a warm collisionless multicomponent magnetoplasma. *J. Geophys. Res.*, 79(7):1073–1082, 1974.

[104] D. Keil. A study of a parallel mode launch into a magnetic beach. *IEEE Trans. Plasma Sci.*, 21(3):329–336, 1993.

[105] H. Pfister, W. Gekelman, J. Bamber, D. Leneman, and Z. Lucky. A fully three dimensional movable, 10m long, remotely controllable probe drive for a plasma discharge device. *Rev. Sci. Instrum.*, 62:2884–2890, 1991.

[106] D. Leneman and W. Gekelman. A novel angular motion vacuum feedthrough. *Rev. Sci. Instrum.*, 72:3473–3474, 2001.

[107] T. Intrator, X. Sun, L. Dorf, I. Furno, and G. Lapenta. A three dimensional probe positioner. *Rev. Sci. Instrum.*, 79:10F129(2), 2008.

[108] R. L. Stenzel. Microwave resonator probe for localized density measurements in weakly magnetized plasmas. *Rev. Sci. Instrum.*, 47:603–607, 1976.

[109] C. M. Franck, O. Grulke, A. Stark, T. Klinger, E. E. Scime, and G. Bonhomme. Measurements of spatial structures of different discharge modes in a helicon source. *Plasma Sources Sci. Technol.*, 14(2):226–235, 2005.

[110] M. P. Reilly and G. H. Miley. Three-dimensional measurements of the helicon wavelength. *Plasma Sources Sci. Technol.*, 19:45006(8), 2010.

[111] D. D. Blackwell, D. N. Walker, and W. E. Amatucci. Whistler wave propagation in the antenna near and far fields in the naval research laboratory space physics simulation chamber. *Phys. Plasmas*, 17:012901(7), 2010.

List of Publications

Conference Contributions

Oral Presentations

1. J. P. Pfannmöller, O. Grulke, K. Sauer and T. Klinger, *Whistler wave measurements in VINETA*, Greifswald–Szczecin mini Workshop "Current topics in plasma waves", Szczecin, Poland (2008)

Poster Presentations

1. J. P. Pfannmöller, O. Grulke, K. Sauer and T. Klinger, *Experimentelle Untersuchungen nicht-linearer Phänomene von Whistlerwellen*, Frühjahrstagung der Deutschen Physikalischen Gesellschaft, P 7.28, Düsseldorf, Germany (2007)
2. J. P. Pfannmöller, O. Grulke, K. Sauer and T. Klinger, *Experimentelle Untersuchungen über nicht-lineare Whistlerwellen-Propagation*, Frühjahrstagung der Deutschen Physikalischen Gesellschaft, P IV.9, Darmstadt, Germany (2008)
3. J. P. Pfannmöller, O. Grulke, K. Sauer and T. Klinger, *Experimentelle Untersuchungen zur Zyklotrondämpfung von Whistlerwellen*, Frühjahrstagung der Deutschen Physikalischen Gesellschaft, P 19.2, Greifswald, Germany (2009)
4. J. P. Pfannmöller, O. Grulke, K. Sauer and T. Klinger, *Experimental Investigations about Cyclotron Damping of Whistler Waves*, 10th International Workshop on the Interrelationship between Plasma Experiments in Laboratory and Space, PG2, Djurönäset, Sweden (2009)

International Max-Planck-Research School on Bounded Plasmas Oral Presentations

1. J. P. Pfannmöller, O. Grulke, *Non–Linear Interaction of Plasma Waves*, Newcomer Report, Greifswald, Germany (2007)
2. J. P. Pfannmöller, O. Grulke, *Non–Linear Whistler Wave Propagation*, Progress Report, Greifswald, Germany (2008)
3. J. P. Pfannmöller, O. Grulke, *Whistler Wave Measurements in VINETA*, Final Report, Greifswald, Germany (2009)

Acknowledgements

Finally, I want to thank all the people who helped me to accomplish this thesis and my education during the past years. A huge number of contributors from different professional and cultural fields crossed my way. Since it is impossible to thank all those people on the limited space available in this thesis, I hope no one is embarrassed.
In particular I would like to thank Prof.Dr.Klinger and Prof.Dr.Grulke for the possibility to accomplish a PhD thesis in the VINETA group. The assistance and discussions during this time is kindly acknowledged. Especially the encouragement to contribute at conferences and in the Max-Planck-Research-School on bounded plasmas has proven useful for the development of the project. In the final stage of the thesis preparation Prof.Dr.Grulke iteratively cross-read various versions of the thesis, which lead to important contributions to the thesis final version.
Prof.Dr.Sauer collaborated in the project and is acknowledged for his help on questions concerning dispersion theory of whistler waves, for the implementation of the code for the calculation of the kinetic dispersion relation and the discussions about whistler waves which always led to new ideas on next steps for this project.
My colleagues in the VINETA group are acknowledge for their help in laboratory issues and the discussions in the group meeting.
Prof.Dr.Hartfuss, Dr.Birus and Dr.Schneider are acknowledged for their invaluable help on questions concerning high frequency electronics. A field in which a kind of mentoring is needed for a start up or total confusion is preprogrammed.
Another essential contribution for the thesis was given by the plasma physics group around Prof.Dr.Stroth, who recognized that simulations of the wave field are necessary in order to give an accurate prediction on the propagation pattern. The simulations are performed by Dr.Lechte, who also implemented the code.
Several other people from the Max-Planck-Institute for plasma physics helped me in questions concerning my thesis, which I like to thank very much. Precise scientific results always needs a precise technical basis to which a lot of employees in the Max-Planck-Institute in Greifswald contribute. Therefore, a big thank you is given to the electronic and mechanics workshop for their support.
During my leisure time in Greifswald I experienced some of the beautiful sides of the region in the north-east of Germany. I remember a lot of sailing in the ASV (Hiddensee) and wind surfing events, which are unforgettable to me. Also the student culture offered a lot of events in the local student clubs (Geokeller, IKUWO) and pubs (Mitt'n'Drin, Domburg) to remember.
In the end I want to thank my family for their moral and financial support during my PhD studies in particular my aunt and uncle, Irmgard and Franz Henkel,

my parents Walter and Sieglinde Pfannmöller and my brother Timo Pfannmöller. Although, I am working in an area which is not common to them they always respected what I am doing, which I am very grateful for.

Eidesstattliche Erklärung

Hiermit erkläre ich, dass diese Arbeit bisher von mir weder an der Mathematisch-Naturwissenschaftlichen Fakultät der Ernst-Moritz-Arndt-Universität Greifswald noch einer anderen wissenschaftlichen Einrichtung zum Zwecke der Promotion eingereicht wurde. Ferner erkläre ich, dass ich diese Arbeit selbständig verfasst und keine anderen als die darin angegebenen Hilfsmittel benutzt habe.

Greifswald, im März 2011

Jörg Pfannmöller